

1-1-2008

## Characterization of the mechanism of bi-layer oxide growth on austenitic stainless steels 316L and D9 in oxygen-controlled Lead-Bismuth Eutectic (Lbe)

Daniel Koury  
*University of Nevada, Las Vegas*

Follow this and additional works at: <https://digitalscholarship.unlv.edu/rtds>

---

### Repository Citation

Koury, Daniel, "Characterization of the mechanism of bi-layer oxide growth on austenitic stainless steels 316L and D9 in oxygen-controlled Lead-Bismuth Eutectic (Lbe)" (2008). *UNLV Retrospective Theses & Dissertations*. 2846.

<http://dx.doi.org/10.25669/hyco-zd18>

This Dissertation is protected by copyright and/or related rights. It has been brought to you by Digital Scholarship@UNLV with permission from the rights-holder(s). You are free to use this Dissertation in any way that is permitted by the copyright and related rights legislation that applies to your use. For other uses you need to obtain permission from the rights-holder(s) directly, unless additional rights are indicated by a Creative Commons license in the record and/or on the work itself.

This Dissertation has been accepted for inclusion in UNLV Retrospective Theses & Dissertations by an authorized administrator of Digital Scholarship@UNLV. For more information, please contact [digitalscholarship@unlv.edu](mailto:digitalscholarship@unlv.edu).

CHARACTERIZATION OF THE MECHANISM OF BI-LAYER OXIDE  
GROWTH ON AUSTENITIC STAINLESS STEELS 316L AND D9 IN  
OXYGEN-CONTROLLED LEAD-BISMUTH EUTECTIC (LBE)

by

Daniel Koury

Bachelor of Science  
Florida Southern College  
1998

Master of Science  
University of Nevada, Las Vegas  
2002

A dissertation submitted in partial fulfillment  
of the requirements for the

Doctor of Philosophy Degree in Physics  
Department of Physics and Astronomy  
College of Sciences

Graduate College  
University of Nevada, Las Vegas  
December 2008

UMI Number: 3352178

## INFORMATION TO USERS

The quality of this reproduction is dependent upon the quality of the copy submitted. Broken or indistinct print, colored or poor quality illustrations and photographs, print bleed-through, substandard margins, and improper alignment can adversely affect reproduction.

In the unlikely event that the author did not send a complete manuscript and there are missing pages, these will be noted. Also, if unauthorized copyright material had to be removed, a note will indicate the deletion.

**UMI**<sup>®</sup>

---

UMI Microform 3352178

Copyright 2009 by ProQuest LLC.

All rights reserved. This microform edition is protected against unauthorized copying under Title 17, United States Code.

ProQuest LLC  
789 E. Eisenhower Parkway  
PO Box 1346  
Ann Arbor, MI 48106-1346



## Dissertation Approval

The Graduate College  
University of Nevada, Las Vegas

August 18, 2008

The Dissertation prepared by

Daniel Joseph Koury

### Entitled

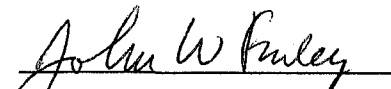
CHARACTERIZATION OF THE MECHANISM OF BI-LAYER OXIDE GROWTH ON

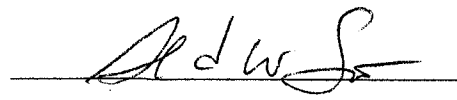
AUSTENITIC STAINLESS STEELS 316L AND D9 IN OXYGEN-CONTROLLED

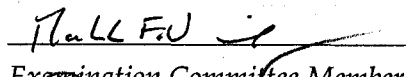
LEAD-BISMUTH EUTECTIC (LBE)

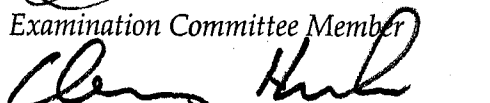
is approved in partial fulfillment of the requirements for the degree of

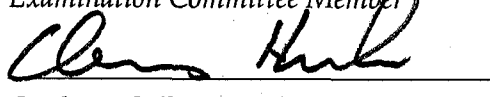
Doctor of Philosophy in Physics

  
Examination Committee Chair

  
Dean of the Graduate College

  
Examination Committee Member

  
Examination Committee Member

  
Graduate College Faculty Representative

  
Examination Committee Member

## ABSTRACT

### **Characterization of the Mechanism of Bi-Layer Oxide Growth on Austenitic Stainless Steels 316L and D9 in Oxygen-controlled Lead-Bismuth Eutectic (LBE)**

by

Daniel J. Koury

Dr. John Farley, Examination Committee Chair

Professor of Physics

University of Nevada, Las Vegas

Lead Bismuth Eutectic (LBE) has been proposed for use in programs for accelerator-based and reactor-based transmutation of nuclear waste. LBE is a leading candidate material as a spallation target (in accelerator-based transmutation) and an option for the sub-critical blanket coolant. The corrosion by LBE of annealed and cold-rolled 316L stainless steels, and the modified austenitic stainless steel alloy D9, has been studied using Scanning Electron Microscopy (SEM), Electron Probe Micro Analysis (EPMA), and X-ray Photoelectron Spectroscopy (XPS). Exposed and unexposed samples have been compared and the differences studied. Small amounts of surface contamination are present on the samples and have been removed by ion-beam sputtering. The unexposed samples reveal typical stainless steel characteristics: a chromium oxide passivation surface layer and metallic iron and nickel. The exposed samples show protective iron oxide and chromium oxide growths on the surface. Oxygen takes many forms on the exposed samples, including oxides of iron and chromium, carbonates, and organic acids from subsequent handling after exposure to LBE. Dif-

ferent types of surface preparation have lead to considerably different modes of corrosion. The cold-rolled samples were resistant to thick oxide growth, having only a thin ( $< 1 \mu\text{m}$ ), dense chromium-rich oxide. The annealed 316L and D9 samples developed thick, bi-layered oxides, the inner layer consisting of chromium-rich oxides (likely spinel) and the outer layer consisting mostly of iron oxides. The cold-rolled samples were able to maintain a thin chromium oxide layer because of the surface work performed on it, as ample diffusion pathways provided an adequate supply of chromium atoms. The annealed samples grew thick oxides because iron was the primary diffusant, as there are fewer fast-diffusion pathways and therefore an amount of chromium insufficient to maintain a chromium based oxide. Even the thick oxide, however, can prolong the life of a steel in LBE, provided proper oxygen control. The mechanisms responsible for the differences in the oxidation behaviors are discussed.

## TABLE OF CONTENTS

ABSTRACT .....	iii
LIST OF FIGURES .....	viii
ACKNOWLEDGMENTS .....	ix
CHAPTER 1 INTRODUCTION .....	1
CHAPTER 2 STAINLESS STEELS .....	4
Introduction .....	4
Ferritic Steel .....	4
Martensitic Steel .....	5
Austenitic Steel .....	6
Surface Work .....	7
Surface Work Performed On Samples .....	8
CHAPTER 3 SAMPLE PREPARATION .....	9
Introduction .....	9
Cutting .....	10
Grinding and Polishing .....	10
Cleaning .....	12
CHAPTER 4 ANALYTICAL TECHNIQUES .....	13
Introduction .....	13
Scanning Electron Microscopy/Energy Dispersive Spectroscopy .....	14
Electron Probe MicroAnalysis/Wavelength Dispersive Spectroscopy .....	20
X-ray Photoelectron Spectroscopy .....	21
CHAPTER 5 CORROSION THEORY .....	28
Introduction .....	28
Oxide Thermodynamics .....	28
Reduction/Oxidation Reactions .....	31

Dry Oxidation .....	32
Aqueous Corrosion .....	32
Dissolution/Oxidation Corrosion by LBE .....	34
Kinetics .....	37
Oxide Layer Growth - Wagner's Law .....	39
CHAPTER 6 OTHER STUDIES .....	48
CHAPTER 7 SEM/EPMA RESULTS .....	53
Introduction .....	53
Surface - Data and Results .....	53
Cross-Sectional Data and Results .....	56
SEM/EDX .....	56
WDS Linescans .....	63
Oxide Growth Rate .....	68
Available Space Model .....	71
CHAPTER 8 X-RAY PHOTOELECTRON SPECTROSCOPY RESULTS ..	74
Introduction .....	74
Abundances as a Function of Depth .....	74
316L Annealed, 3000 h .....	78
316L Cold-rolled, 3000 h .....	78
CHAPTER 9 COLLABORATION .....	83
CHAPTER 10 CONCLUSION .....	86
METALLURGICAL DEFINITIONS .....	94
REFERENCES .....	96
VITA .....	103



## LIST OF FIGURES

Figure 1	Phase diagram of lead and bismuth mixtures .....	2
Figure 2	Surface Contamination .....	12
Figure 3	SEM Illustration .....	14
Figure 4	XPS Illustration .....	15
Figure 5	Electron/Optical Microscopes .....	16
Figure 6	Monte Carlo simulation of electron interaction volume in Fe .....	18
Figure 7	EDX energy resolution without electronic noise .....	19
Figure 8	EDX & WDS overlap spectrum on oxide of D9 .....	21
Figure 9	EDX & WDS overlap spectrum on bulk of D9 .....	22
Figure 10	Universal Curve .....	24
Figure 11	Ion Beam Etching and X-ray Analysis .....	25
Figure 12	Ellingham Diagram .....	44
Figure 13	Metal solubilities in LBE .....	45
Figure 14	Oxide growth kinetics .....	46
Figure 15	Oxide growth kinetics with initial oxide .....	47
Figure 16	SEM Image, EDX Spectra - Unexposed & Exposed, annealed 316L .	54
Figure 17	SEM Image, EDX Spectra - Unexposed & Exposed, annealed 316L .	56
Figure 18	SEM Image, EDX Spectra Covered & Uncovered Areas on exposed, annealed 316L .....	57
Figure 19	SEM Image, EDX Spectra Covered & Uncovered Areas on exposed D9	58
Figure 20	SEM Backscattered electron image and EDX elemental map of ex- posed D9, 1000 h .....	59
Figure 21	EDX hi-res elemental map of exposed D9, 1000hr .....	60
Figure 22	Optical microscope image of exposed D9, 3000hr .....	61
Figure 23	SEM image & EDX Map of exposed, annealed 316L, 3000hr .....	62
Figure 24	Backscattered electron image & EDX elemental map of exposed, cold- rolled 316L, 3000hr .....	63
Figure 25	EPMA backscattered electron image and WDS linescan exposed D9, 1000hr .....	64
Figure 26	Previous WDS linescan of exposed D9, 1000hr .....	66

Figure 27 EPMA backscattered electron image and WDS linescan exposed D9, 3000hr .....	67
Figure 28 Oxide thickness measurements on exposed D9, 1000hr .....	69
Figure 29 Cr 2p <sub>3/2</sub> oxide and metallic standard, Fit to real data.....	77
Figure 30 XPS SDP Percentages of Fe and Cr oxides on exposed, annealed 316L	79
Figure 31 XPS SDP Fe and Cr Intensity profiles on exposed, annealed 316L ..	80
Figure 32 XPS SDP Percentages of Fe and Cr oxides on exposed, cold-rolled 316L .....	81
Figure 33 XPS SDP Fe and Cr Intensity profiles on exposed, cold-rolled 316L .	82
Figure 34 AFM and MFM images of D9 oxide layers .....	84
Figure 35 Hardness and E-modulus on D9 oxide layers .....	85

## ACKNOWLEDGMENTS

I would like to acknowledge the following people for their help and support: John Farley, Allen Johnson, Ning Li, Stuart Maloy, Peter Hosemann, Jenny Welch, Brian Hosterman, Thao Ho, Amo Sanchez, Robert Fairhurst, Clay Crow, Malcolm Nicol, Jim Selser, Clemens Heske, John Kilburg, Matt Eichenfield, Jason McClure, Bill O'Donnell, Len Zane, Sandip Thanki, Bob Chaney and Paul Dryden of Service Physics, and the good folks at the Crown & Anchor.

This work is funded through the University of Nevada, Las Vegas Transmutation Research Program administered through the Harry Reid Center for Environmental Studies and is gratefully acknowledged.

## CHAPTER 1

### INTRODUCTION

In proposed plans for accelerator-based transmutation of nuclear waste, Lead-Bismuth Eutectic (LBE) has been proposed for use in the transmuter, where it can serve two purposes: both as a spallation target (generating source neutrons from the incident proton beam) and as a blanket coolant (removing heat from fission of actinides and transmutation of fission products in nuclear waste). In reactor-based transmutation, LBE can be used as a coolant only.

LBE is a mixture of lead and bismuth in just the right proportions that it constitutes a eutectic. A eutectic is a mixture that has a melting point lower than that of the constituents. Also, all components in the mixture will crystalize at the same temperature if the mixture is at its eutectic point. [1] For LBE the mixture is 45 % lead and 55 % bismuth, and it has a melting point of 123.5 °C. Figure 1 is the phase diagram of lead and bismuth mixtures. The eutectic point is at the “V” point near the diagram center. [2]

The LBE circulates within stainless steel piping and containers. LBE has good thermal properties and makes a good coolant material. However, it severely corrodes the stainless steel pipes in which it is contained via direct dissolution. An absolutely critical question is whether stainless steel walls can be engineered to contain LBE for sufficient lifetime. It is known that the presence of small amounts of oxygen in such a system is beneficial in forming a passivation layer that inhibits corrosion. Lead and its oxides have been studied previously. [3] The general observation in preliminary studies is that, regardless of the nature of oxide growth, the lifetimes of the steels are

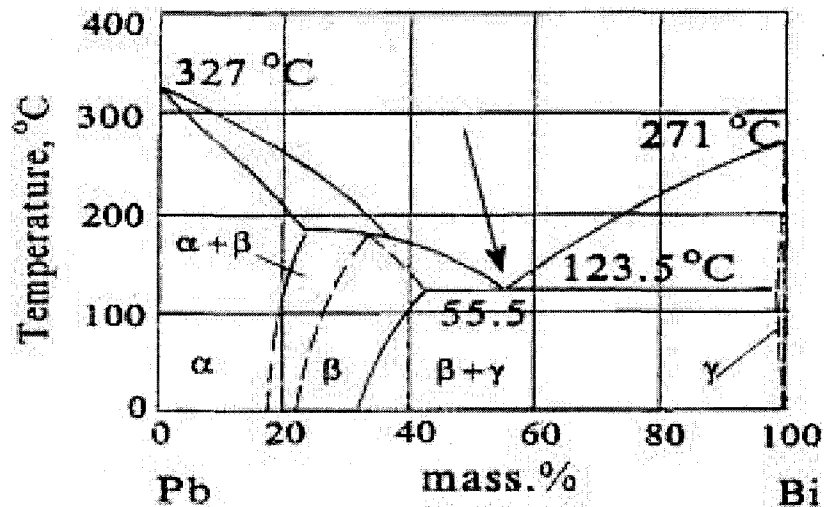


Figure 1 Phase diagram of lead and bismuth mixtures. The eutectic point is noted by the arrow. [2]

increased in most instances by at least an order of magnitude (hundreds of hours to thousands of hours). The ongoing scope of LBE/stainless steel research is to increase lifetimes so that replacement of steel vessels would not be required for a decade or two.

Russian scientists [4] have many decades of experience with LBE coolant in their Alpha-class submarine reactors, having a significant development program and numerous test facilities. They have also performed laboratory studies of the reactions of LBE with US steels. Los Alamos scientists have reviewed these studies [4], in which several US steels [annealed 316L (tube), cold-rolled 316L (rod), T-410 (rod) HT-9 (tube), and D-9 (tube)] and one Russian steel, EP823 (rod), were corrosion-tested. Los Alamos scientists have built and are operating a medium-scale LBE materials test loop, DELTA (DEvelopment of Lead-Bismuth Target Applications). A small-scale test facility is being constructed at UNLV to conduct corrosion experiments in which LBE (or any other liquid metal coolant) is contained in quartz crucibles, such that the only exposed steel surfaces are those of the samples.

A variety of steel samples, some exposed to LBE for varying lengths of time

and temperature and some not exposed to LBE, have been examined in as-received condition. The results reported in this dissertation consist of data taken on the austenitic phase samples mentioned above: annealed and cold-rolled 316L, and D9 stainless steel samples. The exposed samples were exposed to 2 m/sec flowing LBE for 1000, 2000, and 3000 h at 460 °C (cold section) and 550 °C (hot section). The data and analysis reported here focuses on the 550 °C exposures. The total number of examined samples reported here is twelve – D9, 316L annealed, 316L cold-rolled, times three exposure times (9), plus one unexposed sample of each (3).

The purpose of this research is to characterize and understand the chemical corrosion mechanism(s) from the initial phase (how a sample begins to corrode) to the steady state in the LBE environment, including self-healing mechanisms.

## CHAPTER 2

### STAINLESS STEELS

#### Introduction

This chapter presents basic synopsis of the science of metallurgy as it pertains to stainless steels. See Appendix I for a glossary of metallurgical terms relevant to this discussion and research project.

There are over 10,000 different types of steel, dictated by the purposes for which they will serve. They all fall into either of two categories, carbon steels (defined above) or alloy steels.<sup>1</sup>

Stainless steels fall under the alloy classification and are the most common steels. The main components are iron, chromium, and nickel.[5][6] Stainless steels are classified as ferritic, martensitic, or austenitic, based on alloying components (and the amounts of each) and their lattice structures. There are two other classifications: duplex (ferritic-austenitic mixed phase) and precipitation-hardenable, the latter being based on the type of heat treatment used, instead of microstructure. The primary requirement for a steel to be classified as stainless, is that it have a chromium content greater than or  $\approx 11.5\%$  by weight.

#### Ferritic Steel

Ferritic ( $\alpha$  phase) steels are so-named because they have a body-centered cubic crystal structure, like that of pure iron at 300 K, and as such, they are ferromagnetic. Ferritic steels contain 11-30% chromium, and small amounts of austenite-forming

---

<sup>1</sup>Some texts designate three classifications - 0-2% carbon steels, 2-11% low-alloy steels, above 11% high-alloy steels.

elements C, N, Ni. They generally don't have high strength and they are vulnerable to sensitization. As such, chromium carbides form in grain boundaries, reducing the chromium content at grain edges and impairing corrosion resistance. Carburization can consume a lot of chromium: one common form of chromium carbide consumes four to six chromium atoms per carbon atom ( $\text{Cr}_{23}\text{C}_6$  and  $\text{Cr}_6\text{C}$ ). [7] This restricts fabricability and functional size.

Advantages of using ferritic stainless steels include: low production cost, good resistance to stress-corrosion cracking (SCC) induced by chlorides, and good resistance to atmospheric oxidation corrosion. Lower chromium (11%) alloys have good weldability and are widely used in automotive exhaust systems. Intermediate chromium (16-18%) alloys are used for automotive trim and cooking utensils. Higher chromium (19-30 %) alloys, sometimes denoted superferritics, are used in applications requiring high oxidation corrosion resistance. Carburization is minimized by the addition of titanium or niobium, which have higher affinities for forming carbides. [6][8]

### Martensitic Steel

Martensitic steels are frozen in a transitional phase between the austenitic and ferritic phases. This phase takes advantage of cubic crystal distortion to produce very strong alloys. This is achieved by first heating a ferritic steel until it transitions to the austenitic phase (discussed below). Carbon is much more soluble in  $\gamma$ -iron (austenite) than it is in  $\alpha$ -iron. As a consequence of reaching the austenitic temperature, carbon diffuses into interstitial solid solution. The steel is then rapidly quenched to prevent carbides from precipitating out of the grains and the  $\alpha$ -iron phase that would normally reform is greatly deformed. The crystal structure that forms is body-centered-tetragonal and it is magnetic.

Martensitic stainless steels are very hard and brittle. Their hardness depends primarily on the carbon content of the alloy, in direct proportion. They are typi-



cally tempered to improve their ductility, at the expense of some hardness. Typical martensitics have the lowest chromium content of the stainless steels, and relatively high carbon content, therefore making them the least corrosion resistant class of stainless steels. [6][8]

### Austenitic Steel

Austenitic stainless steels are the most numerous in terms of alloys and usages. The austenite phase occurs when a bcc ferritic steel is heated up to such a temperature that the crystal phase transitions to fcc (900 °C to 1400 °C). By alloying with various austenitizers, the fcc phase is preserved upon cooling. Nickel (> 7 wt. %) is the traditional and most popular of these, although a manganese-nitrogen (5 - 20 wt. % Mn) combination is also fairly common.

Austenitics have a wide range of properties, but in general they have exceptional ductility and toughness at a wide range of temperatures. They can also be considerably hardened by cold working. Their corrosion resistance also widely varies, depending on the application, but generally is very good in environments having atmospheric conditions. Molybdenum is added to some alloys (316 and 317) to heighten corrosion resistance in chloride environments. [6][8]

The austenitic alloys in this report have a chromium content of 14.00-18.00 % by weight. They also contain nickel (10.00-14.00 % by weight), whereas martensitic and ferritic steels do not. The added nickel helps to stabilize the austenitic phase and also makes them especially corrosion resistant. [9][10] They are most useful for constructing instruments because of their toughness, ductility, and resistance to corrosion. Austenitic steels comprise the 200 and 300 series of stainless steels, including 316 and 316L. Of the 300 series, 316 is most resistive to corrosion attacks. [5][6] It has been reported that austenitic steels have higher oxidation resistance in LBE due to their relatively high chromium content. [11]

## Surface Work

One key interest in this research is the surface preparation differentiation between the two 316L steels and the D9 steel. All three underwent different surface treatments. Even in the case of exact composition, as with the 316L steels, markedly different corrosion patterns emerge. In a study by *Sencer et al.*, an annealed 316L sample was shot-peened (a form of cold working) and corrosion tested in flowing LBE. Drastic differences in the nature of the corrosion between the treated and untreated samples were observed (discussed in Chapter 6 - Other Studies). [12]

An annealed metal will have large, well-defined grains and, therefore, fewer grain boundary surfaces. A fully annealed steel consists of ferrite with dissolved carbides. A cold worked metal will have deformed grains and take on a martensitic structure. In the process of *cold-rolling* the steel is passed through rollers that provide the plastic deformation force in a very controlled and homogenous way. When external forces induce internal stresses the metal is hardened. This happens due to dislocations in the metal that occur when forced slip processes interfere with each other. Cold-working can also reduce grain size by splitting grains. This is an internal mechanism of stress relief. This is known as *Hall-Petch* (or *Petch-Hall*) hardening, which is demonstrated by a relationship between grain size and the yield point of a material:

$$\sigma_y = \sigma_0 + \frac{k_y}{\sqrt{d}}, \quad (2.1)$$

where  $\sigma_0$  is a starting stress for dislocation movement constant for the material of interest,  $k_y$  is a fitting parameter that is specific to the material,  $d$  is the average grain diameter, and  $\sigma_y$  is the yield stress. [13] As a result of grain splitting more grain boundary surface area is created. It is suggested that by generating surface compressive stress, induced by cold working, cracking is greatly inhibited and chromium diffusion is enhanced. [12][14][15][16] It has been established in the literature that surface texture from finer grains [17] as well as the presence of more grain boundaries

and other diffusion shortcuts provide conditions conducive to a chromium-rich oxide layer. [18]

### Surface Work Performed On Samples

In this study the history of the stainless steel samples is not entirely known. Namely, information on how the samples were prepared (especially surface treatment) is vague. What is known is that there are two types of surface preparation involved with the 316L samples: cold-rolling and annealing. The surfaces of both are quite different: the annealed surface is rough (possibly from a pickling process) and the cold-rolled is somewhat smooth, having lateral striations that could likely be from the rollers in the cold working process.

The D9 sample was annealed and polished, presumably mechanically and aided by a chemical etchant, as it has a shiny appearance to the naked eye. Polishing tends to increase corrosion resistance, as volatile surface contaminants (e.g., sulfur, chlorine) get removed. [8]

## CHAPTER 3

### SAMPLE PREPARATION

#### Introduction

The 316L and D9 samples studied and reported on here were among a batch of steel samples corrosion-tested by scientists at the Institute of Physics and Power Engineering (IPPE) in Obninsk, Russia, under contract to Los Alamos National Laboratory (LANL). The samples were inserted in IPPE's CU-1M non-isothermal LBE loop for time intervals of 1000, 2000, and 3000 hours at temperatures of 460 °C and 550 °C. The 1000h and 3000 h samples were inserted initially, and after 1000 hours the 1000 h samples were removed and the 2000 h samples were inserted for the remaining 2000 hours. This method of inserting the samples gives reason for some caution, as the 2000 h samples may not have experienced the same initial conditions as the 1000 and 3000 h samples. Indeed, the 2000 h samples did exhibit somewhat different behavior compared to the 1000 and 3000 h samples (SEM results in Chapter 7 show some discrepancies). The oxygen level in the LBE was maintained at 30-50 ppb.

The samples were received in "as-is" condition. The 316L annealed samples were tubes 8 mm in diameter (6 mm ID), and the cold-rolled samples were rods 8 mm diameter. The D9 samples were tubes 6 mm in diameter (5 mm ID). All samples were roughly 10 cm in length upon receipt.

It needs to be noted also that the difference between 316 and 316L is carbon content. The "L" in 316L stands for "low carbon". In 316 the carbon content is 0.08 % (by weight) while in 316L it is 0.02 - 0.04 %. See Table 1 for the full compositions of the stainless steels in this research.

Stainless steel alloy D9 is a swell resistant, 15Cr-15Ni- 2.2Mo-Ti austenitic grade steel, similar to 316L, having a slightly higher nickel to chromium ratio (1 to 1) and 0.30 % wt. titanium. The added titanium amounts to a multiple of the carbon content and serves to form TiC precipitates. The precipitates introduce voids and dislocations to the austenite matrix. The voids provide sinks for point defects induced by radiation, which often occur in applications involving high energy particle fluxes. [19][20][21][22][23][24][25]

Material	Fe	Cr	Ni	Si	Mo	Mn	C	other
316L	66.12	17.3	12.1	0.35	2.31	1.8	0.02	
D9 [19]	65.96	13.5	15.5	0.75	2.0	2.0	0.04	0.25 Ti
D9 [20]	68.4	13.6	13.6	0.85	1.11	2.1	0.04	0.31 Ti

Table 1 Steel compositions in weight percent.

### Cutting

Preparing a sample for SEM examination involved several steps. For face-on examination of the outer surface, the only step is to cut the sample to a reasonable size. Anywhere from a few millimeters to a few centimeters per side is sufficient to fit on the SEM stage. The cutting tool was a Buehler Isomet<sup>TM</sup>4000 Linear Precision Saw. Using an Isocut Wafering Blade at 3000 RPM, samples are cut with a feed rate of 5 mm/min.

### Grinding and Polishing

For cross-section examination, several more steps after sectioning are needed. After cutting, the sample is placed edge on in a 1.25 inch diameter cup, with the freshly cut face downward. Then a slow-curing resin epoxy is poured into the cup. The epoxy used was Epothin Low Viscosity Epoxy from Buehler. Average cure time for

this epoxy is about 18 hours. In general, the slower the curing process, the less shrinkage and the better edge retention. Also, since conductivity is imperative, a conductive filler, composed of powdered nickel and graphite, is added to the resin in the mixing phase. Once the sample is completely cured, it can be removed from the molding cup and is ready for grinding/polishing. [26]

The grinding and polishing phase has several steps within itself. The grinding/polishing wheel utilized in this work is the the Beta Grinder/Polisher with the Vector power head from Buehler. The first 5 stages are grinding stages and are performed with silicon carbide sandpaper discs of 240, 320, 400, 600, 800 grits, respectively. Each grinding step (grit) is done for duration of 30 seconds at a force of 5 lb per sample. In short, the theory behind this process is that each grinding phase removes the damage from the grit before it, while doing less damage each time. After the 800 grit grinding step, polishing commences. For our samples, we had two polishing stages: 3 micron MetaDi Diamond Suspension on Textmet (napless chemo-textile polishing pad), and 0.05 micron MasterPrep Alumina Polishing Suspension on Chemomet (polishing cloth). All the products in the polishing stage are also from Buehler. The two polishing stages are done for 2 minutes each, although we have found that running the last phase for as many as ten minutes helps to reveal grain structure on the highly polished plane. [26]

It is important to note that, in between every grinding/polishing phase, the samples are removed from their holders and cleaned. Ideally the cleaning process involves a thorough rinse with distilled water, cleaning with ethanol and a cotton ball, and several minutes in an ultrasonic bath to removed ingrained particles. The rigorous cleaning tasks are vital so as to not contaminate a less damaging grit/polish with particles of larger size. The epoxy is soft compared to silicon carbide, diamond, and alumina so those type of particles can easily embed themselves into the epoxy. [26]

## Cleaning

Once cut, steel samples were cleaned with methanol and, in some cases, placed in an ultrasonic bath for five minutes. The purpose of cleaning was to remove any contamination from cutting products as well as incidental handling.

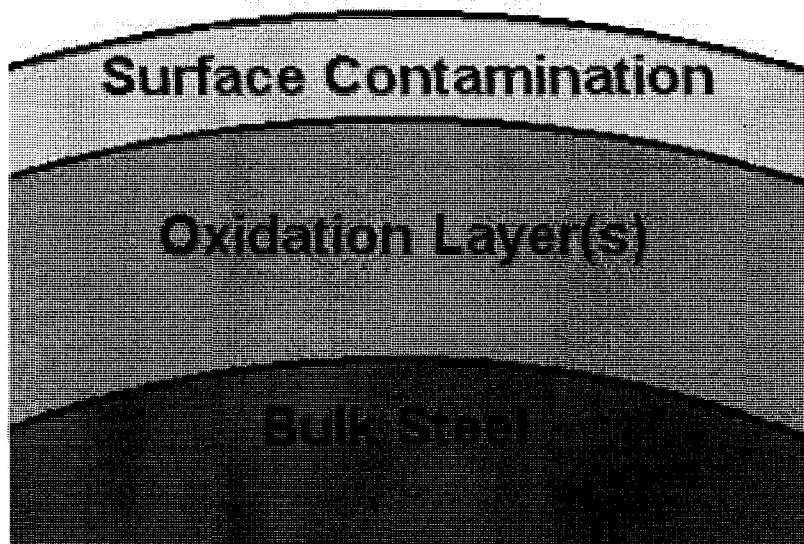


Figure 2 Cross-section view of surface contamination on a sample (not to scale).

The methanol and ultrasonic bath proved to be adequate cleaning for SEM analysis but not for XPS analysis. This is because, as previously mentioned, XPS analysis is highly surface sensitive. Therefore, surface contamination is more prominent. Dealing with surface contamination issues with XPS is discussed in Chapter 8.

## CHAPTER 4

### ANALYTICAL TECHNIQUES

#### Introduction

In our studies, we employed scanning electron microscopy (SEM), in which a high voltage focused electron beam strikes a solid sample and either backscatter or cause secondary electron emission, which are detected to construct an image. The incident electrons also cause fluorescence in the x-ray spectral region (see Figure 3). The X-rays are characteristic of the kind of atom and can be analyzed by energy dispersive x-ray (EDX) spectroscopy. This instrument is capable of measuring elements from boron ( $Z = 5$ ) through uranium ( $Z = 92$ ), mapping the elemental composition as a function of position. EDX has the advantage that it is quick and easy to use.

In addition to SEM, Electron Probe Microanalysis (EPMA) was utilized. An electron beam of the same nature as that in SEM and x-rays produced are analyzed. The key difference between EDX and EPMA is the x-ray detection method. In EPMA the technique of Wavelength Dispersive Spectroscopy (WDS) is applied. WDS has the great advantage over EDX in that it has superior spectral resolution and lower detection limits. This will be discussed later.

We have also performed x-ray photoelectron spectroscopy (XPS). XPS utilizes mono-energetic x-rays to irradiate a surface and eject electrons which are detected and analyzed (see Figure 4). XPS is a much more surface sensitive technique, looking at only the first several layers of atoms. Both techniques are described below.



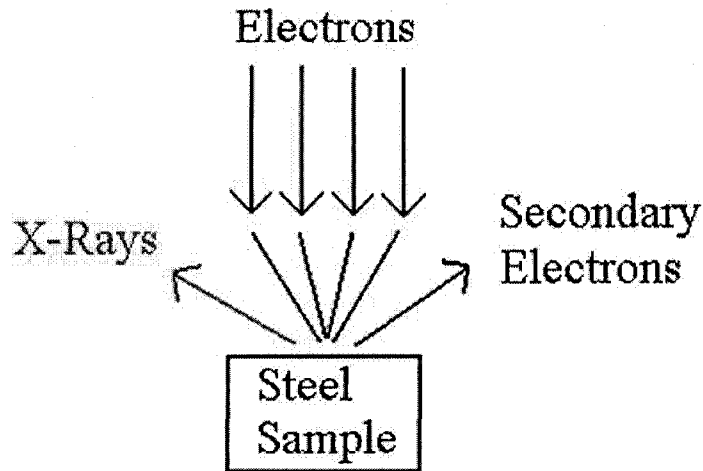


Figure 3 SEM Illustration.

### Scanning Electron Microscopy/Energy Dispersive Spectroscopy

Scanning Electron Microscopy uses 10-20 keV electrons to probe an object and resolve an image by detecting scattered electrons. The function of SEM is very similar to that of an optical microscope, in which photons are focused on an object by means of a series of lenses such that a magnified image of the object is observed through an eyepiece (Figure 5).

The resolution of an optical microscope, or compound light microscope, is limited by the wavelength of the photons used. The Rayleigh criterion for just-resolvable images defines limit of lateral resolution to a reasonable accuracy:

$$x_{min} = f \cdot \frac{1.22\lambda}{D} \quad (4.1)$$

where  $f$  is the focal length of the objective,  $\lambda$  is the wavelength of light used, and  $D$  is the diameter of the lens. For most objective lenses, the ratio  $\frac{D}{f}$  is about 1.2, making  $x_{min} \approx \lambda$ . That means that the resolution of a microscope is approximately equal to the wavelength of light used. For white light, one can achieve resolutions on the order of hundreds of nanometers. In the case of the SEM, the formula is the same

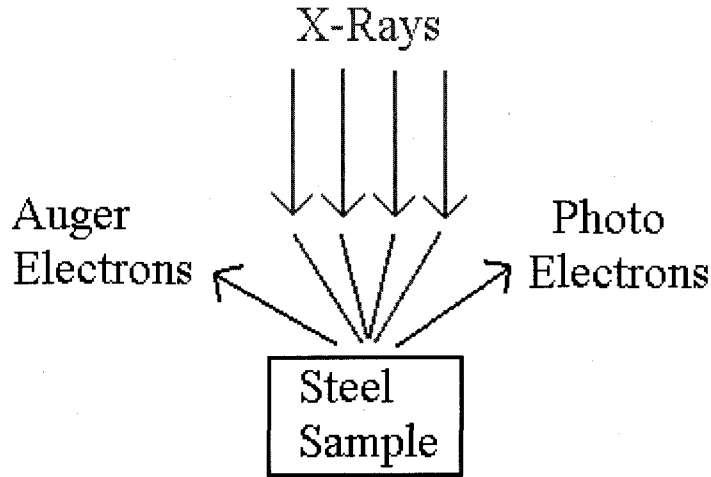


Figure 4 XPS Illustration.

except that the wavelength of the electrons is much smaller and varies depending on the energy of the accelerated electrons. Using the de Broglie relationship: [28]

$$\lambda = \frac{h}{\sqrt{2mE}} \quad (4.2)$$

where  $h$  is Planck's constant,  $m$  is the particle mass (electron mass), and  $E$  is the kinetic energy of the electrons, the de Broglie wavelength of the electrons can be found. For this research the SEM anode was set to 15 kV, accelerating the electrons to an energy of about 15 keV and therefore, having de Broglie wavelengths of  $10^{-11}$  m. This wavelength will, in theory, allow resolution of objects on that same order, with proper magnification. However, real SEM resolution is not that good because of lens aberrations, space charge, mechanical vibrations, electrical noise, finite conductivity, etc. Nonetheless, such high resolution was not necessary in our research since the smallest objects we needed to resolve were conglomerates on the order of several hundred nanometers in size. The electrons are focused by means of current loop magnets onto a surface and either get elastically backscattered, or they collide inelastically with electrons bound to the solid, causing a bulk electron to be ejected as a secondary electron. Either kind of electrons can be detected and used for imaging. Imaging

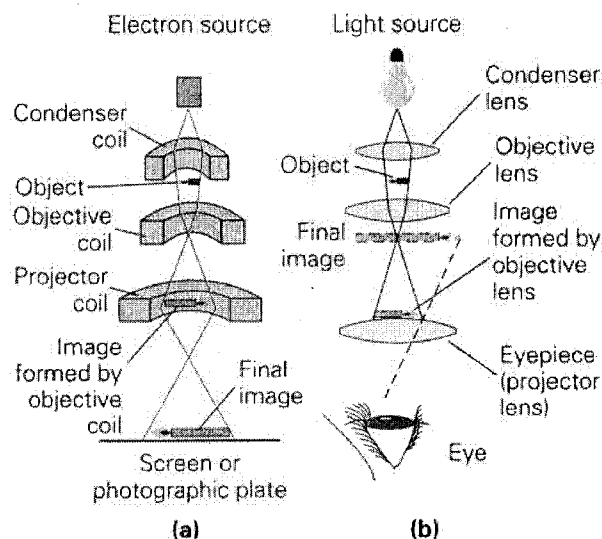


Figure 5 A comparison of the components of an electron microscope (a) and a compound light microscope (b). [27]

works similarly to a television: the images are projected on to a fluorescent screen and different fluorescence intensities dictate whether a particular electron came from a high location (bright spot) or a low location. The sample has to be conducting to avoid local charge buildup and distorted imaging. All of the samples examined were steel, and conductivity proved to be substantial. In the case of poor conductivity, samples have to be either gold or carbon coated as part of their preparation before examination.

As a result of the electrons bombarding a surface, x-rays are emitted with energies characteristic of the elements present in the sample. In a process labeled EDX (Energy Dispersive X-ray), x-ray photons emitted from the sample are detected by a Lithium-drifted Silicon, or Si(Li) detector. Lithium-drifted silicon is made to imitate pure semiconducting silicon, as naturally occurring silicon tends to have impurities that can cause adverse affects. In a process derived by *Pell* [29] (as cited in [30]), the surface of a p-type silicon is exposed to lithium, which diffuses into the silicon matrix and forms a small p-n junction. [31] At the junction boundary is a thin “intrinsic”

semiconductor region, on the order of a few microns in thickness. When a reverse bias electric field is applied to the junction, however, the intrinsic region is expanded up to the millimeter scale. By removing the p-type components it becomes a suitable detector material. It is notable that lithium is quite mobile at room temperature, due to the presence of the applied electric field. Therefore Si(Li) detectors are operated at a 77 K, the temperature of liquid nitrogen, to reduce the number of thermally generated carriers. [30]

When a x-ray photon hits a Si(Li) detector it causes the emission of a photoelectron, which in turn will create electron-hole pairs. Since the detector has an electric field across it, the holes and pairs are swept apart to either end and are registered as an electric pulse. The number of hole-pairs, and therefore the size of the current pulse, is proportional to the energy of the incident x-ray photons. Accordingly, a x-ray spectrum of the elemental composition of the material being examined can be constructed. Peaks emerge from these plots that can be identified with tables or with software. Part of the EDX detector is a multi-channel analyzer (MCA), which is used to collect pulses from different spectral energy windows. As such, a whole spectrum can be acquired at the same time, thereby significantly reducing the collection time typical of traditional scanning type spectrometers.

The x-rays being analyzed come from the area being imaged, so elemental composition can be determined as a function of location on the sample. EDX does not provide information about the chemical state of each element.

The depth that incident electrons penetrate depends on atomic number, the energy of the incident electrons, and the density of the object. Many explanations of electron penetration depth are described in the literature, including a simple equation developed by *Kanaya* and *Okayama*: [32]

$$R_{KO}(\mu\text{m}) = \frac{0.0276 A}{Z^{0.89} \rho} E_0^{1.67}, \quad (4.3)$$

where  $A$  is the atomic weight in g/mol,  $Z$  is the atomic number,  $\rho$  is the density in g/cm<sup>3</sup>,  $E_0$  is the beam energy in keV, and  $R_{KO}$  is the Kanaya-Okayama range. For the 15 keV beam energy used in this study, at normal incidence to a piece of iron ( $Z = 26$ ,  $A = 55.847$  g/mol,  $\rho = 7.87$  g/cm<sup>3</sup>), one calculates  $R_{KO} = 0.992 \mu\text{m} \approx 1 \mu\text{m}$ . The scale of such a depth also manifests itself in all 3 dimensions, namely, the electrons also tend to scatter about a “bulb” shape of roughly the same diameter as the penetration depth. Figure 6 shows a Monte Carlo simulation of electron trajectories in iron from an incident beam of electrons. As a benefit of such a large volume,

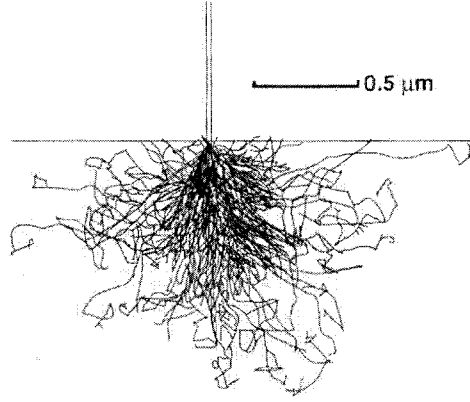


Figure 6 Monte Carlo simulation of the electron trajectories/interaction volume in iron from a 20 keV electron beam ( $R_{KO} \approx 1.6 \mu\text{m}$ ). [30]

EDX sees through the surface (first few atomic layers) which often contains unwanted contaminants. Even with no demanding sample preparation, EDX will provide information preferentially about the bulk rather than the surface. However, x-ray energy resolution is limited (see below).

Energy resolution in EDX is given by

$$\Delta E \propto \sqrt{(C^2 E + N^2)} \quad (4.4)$$

where  $\Delta E$  is the full width, half maximum (FWHM) of the peak (eV),  $E$  is the x-ray photon energy (eV),  $N$  is the broadening contribution from electronic noise which

arises in the the amplification process.  $C$  is the uncertainty in the formation of charge carriers in the Si(Li) detector, given by

$$C = 2.35\sqrt{(F\epsilon)} \quad (4.5)$$

where  $F$  is known as the Fano factor (approximately 0.1 for silicon) and  $\epsilon$  is the amount of photon energy absorbed by each silicon ion ( $\epsilon = 3.8$  eV for silicon), [30][33] and therefore has a value of  $C^2 \approx 2.1$  eV. It can be seen from equation 4.4 that the FWHM for a given peak is very broad, due mostly to the energy-dependence. Even if the contribution from noise were completely eliminated,  $\Delta E$  is still significantly broad. Figure 7 shows a plot of  $\Delta E$  vs. x-ray energy, in the absence of electronic noise.

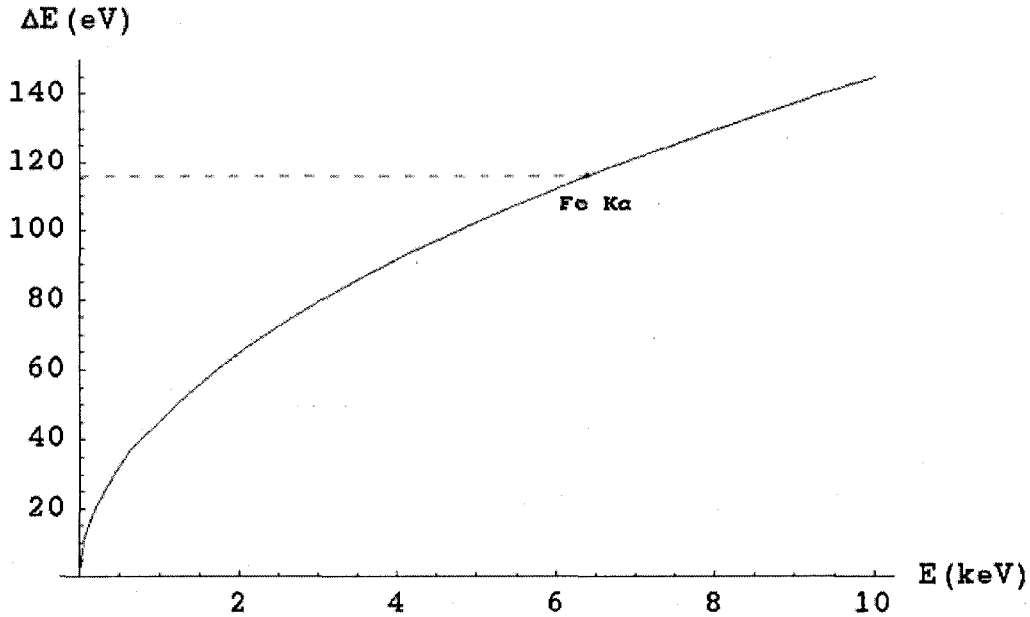


Figure 7 EDX FWHM energy resolution in the absence of electronic noise. For reference,  $\Delta E_{Fe K\alpha} \approx 116$  eV.

Two major problems with poor resolution in EDX is peak overlap between elements, or overlap between different peaks of the same element, and detection difficulties of trace elements and/or weak signals of minor peaks. These issues are greatly

diminished in WDS (see below).

One more feature combines imaging with elemental analysis. Elemental mapping allows users to create images for designated elements for a given area of interest. The utility of this technique is obvious: determination where elements are concentrated in an area and their relative concentrations (qualitative). Elemental mapping can be done with EDX or WDS. To create maps, energy windows for elements of interest are defined in the SEM/EPMA software, and then x-ray fluorescence counts for those given energies are plotted as a function of location, as the electron beam scans over the sample. The spatial resolution of EDX or WDS maps are limited to the dimensions of the interaction volume, discussed above. Such a limited resolution is remarkable considering that the incident electrons have a beam width on the order of nanometers. In Transmission Electron Microscopy (TEM) samples are prepared extremely thin, on the order of 100 nm. Having such a small volume prevents numerous electron/atom scattering events, thereby allowing much better EDX resolution.

#### Electron Probe MicroAnalysis/Wavelength Dispersive Spectroscopy

Electron Probe MicroAnalysis (EPMA) is basically the same as the SEM/EDX techniques mentioned above, with the major difference being the method of characteristic x-ray detection. In WDS various crystals are used to disperse x-rays via Bragg diffraction. Full spectra are constructed sequentially by several crystals, as opposed to EDX where an entire spectrum is acquired at once. Different crystals are needed as each can only disperse over a certain range of x-ray wavelengths, and resolution depends on the given crystal. Nonetheless, even the poorest resolution of any WDS crystal is many times better than EDX (Figures 8 and 9). An order of magnitude better resolution is possible with some crystals. With such better resolution, trace elements can be identified and quantified in many cases. The primary use of WDS is quantitative analysis. A typical WDS system is sensitive to tens of parts per million.

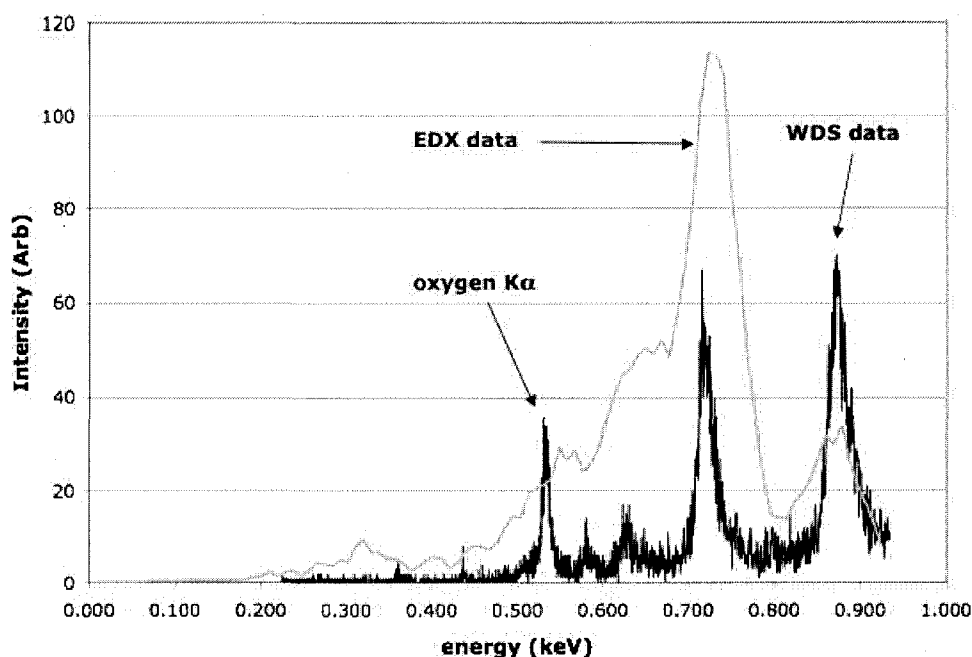


Figure 8 Overlapping EDX and WDS (LDE1 crystal) spectra on an oxide layer of D9. Resolution differences are clearly evident.

In this work WDS was used to perform quantitative linescans. Quantitative linescans are performed by rastering the electron beam along a series of points, with a step size of about  $0.5\ \mu\text{m}$ , whose coordinates are user-defined. Characteristic x-rays are analyzed quantitatively as a function of those coordinates.

Disadvantages of WDS are that measuring x-ray wavelengths is time consuming and characteristic peaks have to be anticipated. Because of the ease of use, EDX is often used in conjunction with WDS to first determine which elements are present in a sample.

### X-ray Photoelectron Spectroscopy

Emission of electrons from the surfaces of materials induced by either a photon or another electron is one of the most successful ways of learning about composition, structure, and bonding at surfaces on an atomic and molecular scale. [28]



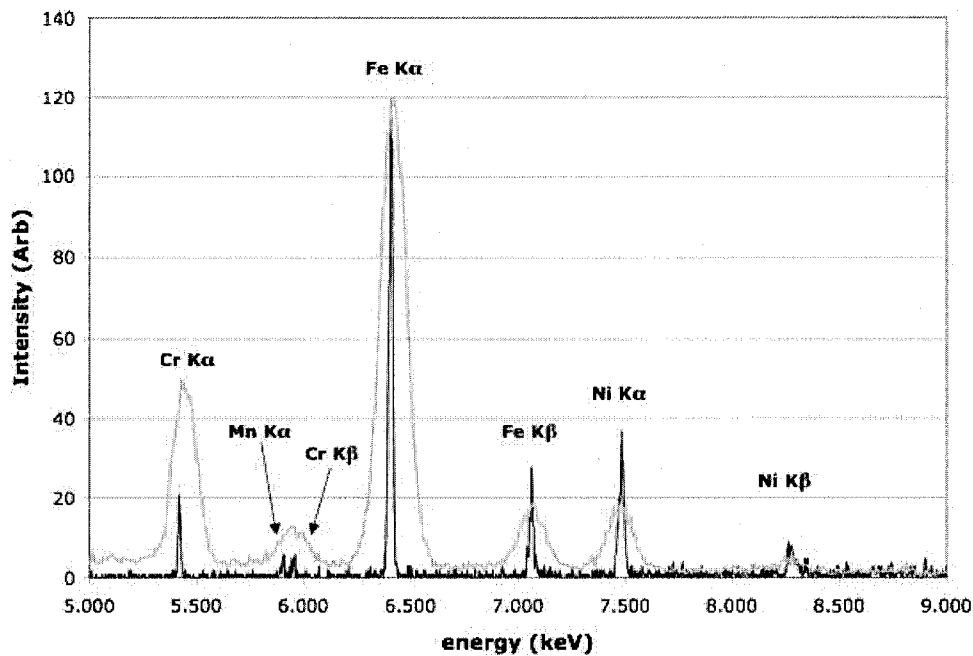


Figure 9 Overlapping EDX (gray) and WDS (black) (LiF crystal) spectra on bulk D9. Superior WDS resolution allows identification of manganese  $K\alpha$  peak in the presence of chromium  $K\beta$ .

The XPS instrument used in this research is a Surface Science Instruments model SSX-100 which has been fitted with a Nonsequitur Technologies Model 1401 ion gun for sputtering.

In x-ray photoelectron spectroscopy (XPS), electrons are photo-emitted from atomic core levels by use of mono-energetic (1.486 keV) x-rays. The x-ray source consists of an aluminum anode, where Al  $K\alpha$  photons are produced by electron beam bombardment of an aluminum target. The x-rays excite atomic core electrons on the sample, causing them to eject into vacuum with kinetic energies of

$$KE = h\nu - E_b - \phi_s \quad (4.6)$$

where  $h\nu$  is the energy of the incident x-ray photons,  $E_b$  is the binding energy of the ejected electron, and  $\phi_s$  is the spectrometer work function. [34] The electrons are

detected and their energies analyzed. A spectrum is plotted of electron counts per energy interval as a function of kinetic energy. Similar to SEM/EDX, these electron kinetic energies are characteristic of the elements present: each element has its own unique spectrum. In a material composed of more than one constituent, the sum of the peaks from each element comprises the overall spectrum.

XPS has a few of its own advantages that makes it a unique and powerful method for analyzing materials. One of those advantages is its surface sensitivity. Even though x-rays can penetrate several microns deep into a material, the electrons that are analyzed come from just the top few atomic layers. This is because the inelastic mean free path of the electrons in a solid is very small, so only atoms near the surface emit electrons that can escape elastically. The inelastically scattered electrons contribute to the background. Therefore, XPS will provide data on just the top few atomic layers at the surface. According to the *universal curve* (Figure 10), electrons with kinetic energies of 1-2 keV will have inelastic mean free paths (IMFP) of a few nanometers.

In XPS, core holes are created that can be filled by two processes: a direct (radiative) or indirect (non-radiative, known as Auger) process. In the radiative process, the vacancy (hole) is filled by an outer shell electron. In the relaxation process, an outer shell electron falls into this hole, releasing its energy in the form of a photon. In the second, non-radiative process, the excess energy from the relaxation of the atom is transferred to another atomic electron, which is ejected. This process is called the Auger Effect. Like photoelectrons, Auger electrons serve as a means of elemental fingerprinting and show up as peaks in XPS scans. The emission of an Auger electron occurs about  $10^{-14}$  s after the photoelectric emission, and the kinetic energy of an Auger electron is independent of the initial state of ionization. [35] In most cases, depending on the binding energy, the Auger transition rate is faster than the radiative

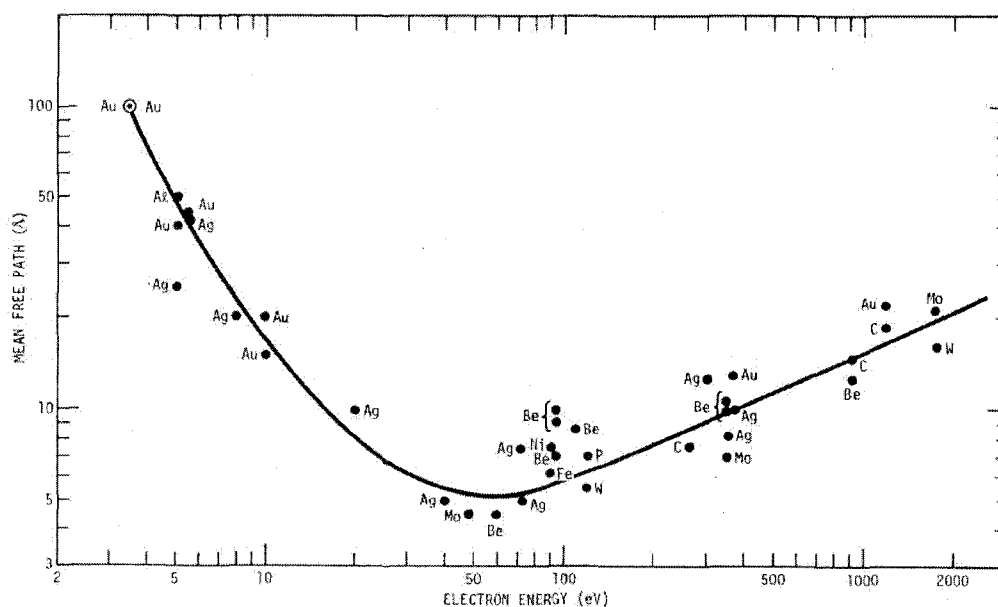


Figure 10 The mean free path of electrons in different solids as a function of kinetic energy. [28]

rate and therefore is more probable. [36] Auger peaks appear in the spectra taken in this work, however, they were not analyzed.

XPS analyzer resolutions are in the range of 0.7 - 1.4 eV. Such resolutions are sufficient to discriminate various peak shapes characteristic of the type of material (conductor/insulator) being irradiated and local charge (chemical state) of the elements in the material. [37] This allows tracking of oxidation states of elements at the surface. Even though XPS probes binding energies in the range of inner core electrons, those energies shift as a result of changes in the chemical environment and the shift can be detected. The shifts in energy are related to charge transfer in outer electron levels and final state effects. An electrically neutral element becomes oxidized by losing electrons, leaving it with a net positive charge. This causes electrons to be more tightly bound due to less charge shielding. In the case of oxidation, where an element has lost electrons, a shift to higher binding energy is observed. The degree

of oxidation is then determined by the amount of peak shift. Oxidation is discussed in Chapter 5.

The XPS apparatus we used also had an ion beam milling (also known as ion sputtering) device attached to it. With the device, a beam of  $\text{Ar}^+$  ions can be formed and focused onto a material ( $\approx 30^\circ$  to the normal) for surface ablation. This allows for performing sputter depth profiling (SDP) (Figure 11).

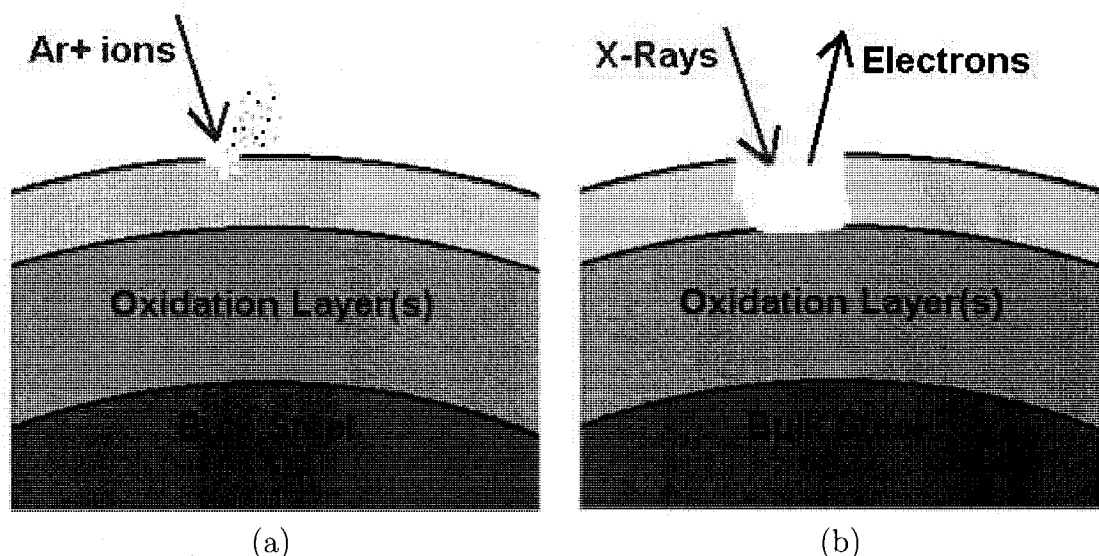


Figure 11 (a) Ion Milling of the surface of a sample. (b) X-ray analysis of an ablated surface.

Though the sputter rate is not trivial to determine, it can be approximated. A good approximate measure to sputter rates can be found by inserting chips of silicon with an oxidized surface of known depth. Sputter rates for various oxides were measured by *Engelhard et al.* and their results are shown in Table 2. [38] By sputtering for short time intervals and taking x-ray data while watching for elemental peaks to change, a rate can be determined once the oxide layer is penetrated. Sputtering for short amounts of time (5 - 10 sec) can be done to clear away surface contaminants, while sputtering for longer times (30 - 300 sec) will etch deeper into the bulk. Milling

Oxide	Thickness (Å)	Ratio to SiO <sub>2</sub>
Fe <sub>2</sub> O <sub>3</sub>	328	0.60
Cr <sub>2</sub> O <sub>3</sub>	685	0.49

Table 2 Ratio of sputter rates of Fe<sub>2</sub>O<sub>3</sub> and Cr<sub>2</sub>O<sub>3</sub> to SiO<sub>2</sub> with an Ar<sup>+</sup> ion beam at an incident angle of 45°. [38]

for increased time intervals can be executed, with XPS survey scans and high resolution elemental scans performed at each interval. This allows for elemental and chemical mapping as a function of depth. By subtracting the background via the method of *Shirley* [39], measuring the area of pertinent peaks in XPS hi-res spectra, and multiplying that value by an appropriate atomic sensitivity factor, approximate atom percentages of elements in a material can be measured. Performing this quantitative technique with ion milling intervals is sputter depth profiling (SDP). The information obtained should be in agreement with WDS linescans mentioned previously (after conversion to weight percent). Similar to SDP, one can track oxidation states of important elements as function of depth. The data contained within a SPD set includes peak energies which can shift with depth: for example, iron typically shifts from higher energy (oxidized) to lower energy (metallic) as the oxide layer of a piece of iron is sputtered through. This information is very useful in determining whether an element present in oxide layers is simply a metallic alloy diffusant suspended in the oxide matrix, or it is an actual constituent of the oxide matrix.

Some undesirable effects occur from sputtering a surface with ions, resulting in changes in the target material. Some of these effects include implantation of incident ions, changes in lattice structure, and, most importantly, chemical changes. [40] Ions intermixing with a target obviously change the composition of a material. [41] Chemical changes can appear in the form of oxidation shifts from creation or destruction of

chemical bonds. [40] Although argon can be used to bombard the sample, oxidation because of elevated oxygen partial pressures can occur. Stimulated oxide growth by this method usually increases sputter times. [42]

The effects mentioned above do not necessarily dominate the XPS/SDP environment. Nevertheless, when interpreting XPS/SDP data, they need to be considered, especially as sputtering time is increased.

## CHAPTER 5

### CORROSION THEORY

#### Introduction

The corrosion mechanism of the LBE/steel system is not completely understood. Experiments have been carried out and theoretical models have been developed to help to understand the thermodynamics and kinetics entailed in such an environment. There are ideas about preserving the steel surfaces and models describing the LBE/steel chemical behavior. Thus far, models agree with experiments to the extent that short-term predictions can be made about the longevity of various steels and needs for future maintenance.

#### Oxide Thermodynamics

The chemical processes that occur in oxidation can be predicted by thermodynamics. Thermodynamics dictates whether or not a particular reaction can occur. The rate at which a system changes is dictated by kinetics, which will be discussed later.

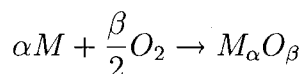
The thermodynamic quantity  $G$ , the Gibbs Free Energy, and its properties are at the core of the theoretical machinery describing chemical reactions. It is  $\Delta G$  that can be measured. Any system that can lower its Gibbs Free Energy via chemical reaction at a given temperature and pressure will do so for a spontaneous reaction. The total Gibbs Free Energies of the reaction products must be lower than that of the reactants, and thus  $\Delta G < 0$ . The application of this principle is universal throughout chemistry, though the focus of this discussion will be on the Gibbs Free energies of a metal or metallic alloy with oxygen.

The change in Gibb's Free Energy can be determined in several ways. One way is from the thermodynamic relationship, derived from the second law of thermodynamics, involving enthalpy ( $H$ ), entropy ( $S$ ), and temperature ( $T$ ) of an isothermal, isochoric system. For temperatures above 298 K, where temperature is constant,

$$\Delta G = \Delta H - T\Delta S. \quad (5.1)$$

The changes in enthalpy and entropy for many reactions are tabulated in a large number of texts.

Another way to determine  $\Delta G$  in a reaction (isothermal, isobaric),



is by considering how it relates to the equilibrium constant,  $K$ , given by

$$K = \frac{a_{MO}}{a_M^\alpha a_{O_2}^{\beta/2}}, \quad (5.2)$$

where  $a_{MO}$ ,  $a_M^\alpha$ , and  $a_{O_2}^{\beta/2}$  are the chemical activities of the metal oxide, the metal, and oxygen, respectively. The relationship between  $\Delta G^\ominus$  (standard Gibbs free energy change) and  $K$  is

$$-\Delta G^\ominus = RT \ln K. \quad (5.3)$$

The negative sign provides a positive value for spontaneous reactions. Substituting equation 5.2 into equation 5.3 gives

$$-\Delta G^\ominus = RT(\ln a_{MO} - \alpha \ln a_M - \frac{\beta}{2} \ln a_{O_2}). \quad (5.4)$$

This relationship can be expressed in terms of the chemical potentials such that

$$-\Delta G^\ominus = \Delta \mu_{MO} - \alpha \Delta \mu_M - \frac{\beta}{2} \Delta \mu_{O_2}, \quad (5.5)$$

as  $\Delta \mu_i = RT \ln a_i$  is defined as the change chemical potential,  $\mu$ , of species  $i$  from its standard state. When a chemical species is pure, meaning there are no other elements



mixed with it, it has a maximum chemical activity equal to one. This is defined to be standard state. Therefore when a metal alloy (meaning the metal is not pure, such as in the case of steel) is in contact with pure oxide, then equation 5.5 becomes

$$-\Delta G^\ominus = -\alpha \Delta \mu_M - \frac{\beta}{2} \Delta \mu_{O_2}. \quad (5.6)$$

Other such simplifications of equation 5.5 can easily be made by assuming maximum activity of any of the species involved. It follows from the nature of spontaneous reactions that  $\Delta \mu \leq 0$ . [43]

To discuss the activity,  $a$ , of a substance,  $i$ , in order to relate it to an observable, for an ideal vapor it can be shown that

$$a_i = \frac{p_i}{p_i^*}, \quad (5.7)$$

where  $p_i$  is the partial vapor pressure of solute  $i$  and  $p_i^*$  is the vapor pressure of pure substance  $i$ . It can be seen here that  $a_i \rightarrow 1$  as  $p_i \rightarrow p_i^*$ . [1] This relationship, when substituted into equation 5.4, provides a relationship between the Gibbs free energy change of a system and pressures,

$$-\Delta G^\ominus = RT(\ln p_{MO} - \alpha \ln p_M - \frac{\beta}{2} \ln p_{O_2}), \quad (5.8)$$

where the pure vapor pressures ( $p_i^*$ ) of each are taken to be 1 atm, which also accounts for the apparent problem of units inside the natural log. The pressures shown in equation 5.8 are dimensionless.

The thermodynamics discussed above is very useful when a pure metal and its pure oxide are in intimate contact. The oxygen pressure developed in such a system is conventionally designated the dissociation pressure ( $p_{O_2}$ ) and, for a given temperature, obeys the equation

$$\begin{aligned} -\Delta G_T^\ominus &= -\frac{\beta}{2} \Delta \mu_{O_2} \\ &= \frac{\beta}{2} RT \ln p_{O_2}. \end{aligned} \quad (5.9)$$

A convenient graphical representation the relationship between free energy and partial oxygen pressure for metals and their corresponding oxides is the *Ellingham Diagram* (Figure 12). Drawing a line from the “O” in the upper left corner to the intersection of the  $\Delta G^\ominus$  curve and desired temperature will determine the equilibrium oxygen partial pressure at which a given metal will oxidize when the line is extrapolated to the “ $P_{O_2}$ ” scale on the right side of the diagram. If  $\Delta G^\ominus$  for a certain metal is above a particular  $P_{O_2}$  line, that means the oxygen partial pressure is too low to form an oxide, and any oxide of that metal already present will be reduced. Conversely, if  $\Delta G^\ominus$  falls below the  $P_{O_2}$  line, the metal will continually oxidize. [44] This is the idea behind the “sacrificial anode” process: if a metal of a smaller  $|\Delta G^\ominus|$  is placed in contact with an oxide of greater  $|\Delta G^\ominus|$ , then the latter will be reduced in favor of the oxide of the previous. The processes of oxidation and reduction are discussed in the next section.

### Reduction/Oxidation Reactions

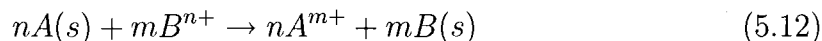
In a typical oxidation corrosion environment, an electrochemical process resembles a galvanic cell, an electrochemical cell which operates a spontaneous reduction-oxidation (redox) reaction, in which reacting species exchange electrons to form products. In a redox reaction, one of the reactants is oxidized, meaning that it gives up electrons, increasing its oxidation number. The other reactant is reduced, meaning that it accepts electrons, decreasing its oxidation number. The species is oxidized by an oxidizing agent, which itself is the reduced species. The oxidized species is the reducing agent. [1]

Consider two representative elements, A and B. The chemical equation representing the sum of reduction and oxidation half-reactions, in which electrons appear explicitly, are written as





where  $m$  and  $n$  are the oxidation numbers. The net equation is just the sum of the two, properly balanced so that electrons cancel and charge is conserved.



In this redox reaction, element A is oxidized and is the reducing agent, while element B is reduced and is the oxidizing agent.

### Dry Oxidation

When a clean stainless steel surface is exposed to air in atmospheric conditions, it immediately begins to form an oxide layer. It forms because of the influence of an electric field, which is described quantum mechanically by the *Cabrera-Mott* theory. The concepts of the theory are: oxygen atoms adsorb to the surface, electrons from the metal pass through the thin oxide film already present, and the oxygen atoms become anions by capturing the electrons. This process creates a strong electric field across the film, on the order of  $10^6$  V/cm, for films roughly 10 nm thick. The electric field is responsible for driving metal cations through the oxide. Film growth is ultimately restricted by the limited range of electrons available by tunneling or thermionic emission. [46] According to the theory for thin oxides, the growth of the oxide has the inverse logarithmic form

$$\frac{1}{X} = C_1 - C_2 \ln t, \quad (5.13)$$

where  $X$  is the thickness of the oxide as a function of  $t$ . [47][48]

### Aqueous Corrosion

One of the most common forms of corrosion is aqueous corrosion. Aqueous corrosion can occur in many forms. For all types of aqueous corrosion, it is well known that the process proceeds by an electrochemical mechanism. An anodic and cathodic

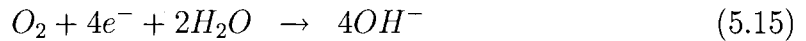
reaction must occur, very similar to that of an electrochemical cell. Oxidation takes place at the anodic site, while reduction takes place at the cathodic site. At the anodic site, material is lost to oxidized ion dissolution and redeposited, after forming a solid oxide, at the cathodic site. These two reactions must take place simultaneously, as the electrons gained in the reduction process are provided by the oxidation process. If the electrons from oxidation cannot be consumed, the anodic reaction does not take place.

One familiar form of this type of corrosion is the oxidation of iron alloys, or rusting. The fact that iron prefers to exist in its oxidized form is a major nuisance in the industrial world. Rust corrosion in the United States alone costs \$276 billion per year. [49]

A piece of iron with water on it exposed to atmosphere serves as a good example of rusting. In the scenario, iron atoms on the surface of the metal in contact with the water serves as the anodic site. The iron is oxidized (ionized) in the following fashion



The surface of the water in contact with atmosphere serves as the cathodic site. Here, both oxygen and hydrogen ions (from acid solutions) are reduced. The oxygen molecules are dissolved in solution to form hydroxide, and hydrogen gas is produced by the reduction of the hydrogen ions. The reduction reactions are



In the case in which the iron is only partially exposed to the solution, such as water droplets on a piece of steel, there is often separation of anodic and cathodic sites, with the latter at the water/atmosphere boundary where there is oxygen available. Rust would form in between the two in this system. The iron ions bond with hydroxide ions

in solution and precipitate out, forming various insoluble mixtures of iron, oxygen, and hydrogen. A few of these are  $\text{Fe}(\text{OH})_2$ ,  $\text{FeO} \cdot \text{OH}$ , and  $\text{Fe}_2\text{O}_3 \cdot \text{H}_2\text{O}$ . [49][50][51]

Since steels are widely used structural materials, much has been learned about rusting. Many techniques have been developed for use either in the manufacturing stages, such as experimenting with different alloys in different quantities, or in the post-manufacturing stage, such as covering steels with paint or other protective material. [51]

### Dissolution/Oxidation Corrosion by LBE

It is known from experience that LBE attacks steel surfaces, corroding them severely and rapidly. The type of corrosion that occurs is dissolution corrosion. This corrosion occurs mostly because the base and major alloying components of steels are soluble in LBE. Those elements include nickel, chromium, and iron, listed in decreasing order of solubility (Figure 13), given by the relationship

$$\log(c_{sat}) = A + \frac{B}{T}, \quad (5.17)$$

where  $c_{sat}$  is the saturation concentration in weight ppm,  $T$  is temperature in Kelvin, and the constants,  $A$  and  $B$ , are given in Table 3. [52][53][54][55] It has been found that adding a small amount of oxygen, on the order of tens of ppb, to the LBE will greatly reduce the steel corrosion. Lead and bismuth are chemically more inert than the major alloying elements of steel, namely, the elements listed above, because they all have higher molar free energies of formation for oxidation. Therefore, it is possible to form chromium and iron-based oxidation layers at the LBE-steel interface that can passivate the steel surface. With proper oxygen control, a self-healing protective oxide film forms. The oxide layer protects the metal substrates by greatly reducing diffusion, as diffusion rates of the alloying elements in oxides are negligibly small. The oxide, however, is reduced by the LBE at the interface, but it reaches a local equilibrium and

the iron concentration is at equilibrium. [52][53] This reduction process is discussed below.

The oxygen level must be carefully maintained by active oxygen control. [53] If not enough oxygen is present in the coolant, the protective oxide films on the steel surfaces are not formed, therefore permitting dissolution corrosion as mentioned above. If too much oxygen is present, exceeding solubility, then solid lead and/or bismuth oxides can form from the overabundance of oxygen. Such oxides contaminate the coolant and can precipitate out in cool regions, possibly clogging the flow of coolant. Another problem that will occur if the oxygen levels are not properly maintained is reduction of the oxide layers until they are thin enough such that diffusion of substrates is considerable. The main idea behind active oxygen control is to control oxygen levels properly, in order to keep the reduction process at an equilibrium between the formation and dissolution of oxides. [53]

The popular description of the actual corrosion mechanism of the LBE/steel system, as proposed by several papers, is described here. Multi-phase oxide scales are formed because of different diffusion rates in alloying components, which occurs as a result of different solubilities of the alloys in LBE. Three different layers form on the steel surfaces: an outer magnetite ( $\text{Fe}_3\text{O}_4$ ) which is on top of the original surface and consists mostly of iron and oxygen, an intermediate spinel  $\text{Fe}^{2+}(\text{Fe}_{1-x}^{3+}\text{Cr}_x^{3+})_2\text{O}_4(+\text{Ni})$ , and an innermost layer which is an oxygen diffusion zone with spinel formation along grain boundaries. [11][52][56][57] Micro-Raman studies performed by *Hosterman* [58] at UNLV have confirmed the presence of the magnetite layer. Further Raman projects are underway to determine the chemical nature of the inner oxide layer(s).

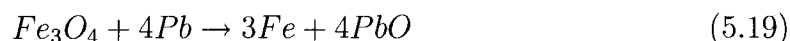
The proposed mechanism for the layering goes as follows: oxygen in the LBE first reacts with iron and chromium to form the Fe-Cr spinel. The spinel is porous and will allow oxygen to diffuse through this layer and further react with steel elements

to form more spinel-like structures. Because of the inward diffusion of oxygen, the Fe-Cr spinel grows inward, forming the innermost layer mentioned above. Similarly, iron diffusion outward is what accounts for the outer magnetite layer, which grows on the surface. Chromium diffusion occurs more slowly which accounts for its presence only in the inner layers. In those regions, the chromium content is roughly 1.5 times higher than its concentration in the bulk. This is due to iron depletion. [56]

Dissolution occurs if too little oxygen is available for an oxide layer with iron. In this regime, the concentration of iron in LBE is equal to its saturation level, meaning the iron concentration is at an equilibrium. [53] The concentration of the iron in LBE is

$$\log(c_{Fe}) = 6.01 + \frac{-4380}{T}, \quad (5.18)$$

where  $T$  is temperature in Kelvin. If sufficient oxygen is present and the oxide is formed, the reaction that takes place at the interface is a reduction reaction with lead as the reducing agent.



The concentration of iron in this situation is now determined by the following:

$$\log(c_{Fe}) = 11.35 - \frac{12844}{T} - \frac{4}{3}\log(c_O), \quad (5.20)$$

where  $c_O$  is the concentration of oxygen. The point where the two functions, equations 5.18 and 5.20, of iron concentration are equal determines the minimum oxygen concentration to form the oxide layer. The ideal oxygen concentration is actually higher than this point such that the iron concentration is significantly lowered and the oxidation corrosion rate is minimized. [53][52] The upper limit of the oxygen concentration is determined by the activity at which lead oxide forms in the coldest region of the system. This is indicated in the Ellingham diagram, Figure 12.

## Kinetics

As previously mentioned, the thermodynamics of the metal/LBE system is what dictates what chemical processes can and do occur. To enrich the picture a discussion of the kinetics of the system is appropriate. Such topics as LBE flow rate and mass transport, oxide growth rate, precipitation deposition will be discussed.

In a model of the mass transport phenomenon developed by *Li et. al.*, [52][54][55][59] the dynamics of the flowing LBE and metallic species dissolution is described by the convection/diffusion equation:

$$\frac{\partial c_i}{\partial t} = D_i \nabla^2 c_i - (\mathbf{v} \cdot \nabla) c_i \quad (5.21)$$

where  $c_i$  is the concentration of the  $i^{th}$  corrosion product in wppm,  $D_i$  is the diffusion coefficient of the  $i^{th}$  product in the liquid, and  $\mathbf{v}$  is the velocity vector of the flowing liquid. The diffusion coefficient for metal atoms in liquid metal solvents is reported in the literature by the Einstein-Sutherland equation

$$D_M = \frac{kT}{4\nu r_M \pi}, \quad (5.22)$$

where  $k$  is the Boltzmann constant,  $T$  is temperature in Kelvin,  $\nu$  is the viscosity of the liquid metal solvent, and  $r_M$  is radius of the diffusing metal atom. [60] Assuming no time dependence (steady state), diffusion only occurring in the axial ( $x$ ) direction, and convection occurring only in the transverse ( $y$ ) direction, the equation simplifies to

$$\gamma y \frac{\partial c_i}{\partial x} = D_i \frac{\partial^2 c_i}{\partial y^2} \quad (5.23)$$

where  $\gamma$  is the shear rate at the steel interface in  $\text{sec}^{-1}$  and  $y$  is the transverse distance from the interface. The product  $\gamma y$  is the viscous-flow velocity of the LBE, which is zero at the wall, where  $y = 0$  (boundary layer), and increases in proportion to  $y$ . In this model, it has been assumed that mass transfer in LBE is dominated by convection



and diffusion, such that chemical reactions can be ignored. By parameterizing  $x$  and  $y$  with

$$\begin{aligned}\xi &\equiv \frac{x}{L}, \\ \eta &\equiv \left(\frac{\gamma}{DL}\right)^{1/3} y,\end{aligned}$$

where  $L$  is the length of the test loop, equation 5.23 now reads

$$\eta \frac{\partial c_i}{\partial \xi} = \frac{\partial^2 c_i}{\partial \eta^2}. \quad (5.24)$$

Writing the solution of the concentration as a Fourier series

$$c_i(\xi, \eta) = \sum_k Y_k(\eta) e^{2\pi i k \xi}$$

and inserting it into the PDE above, one will find that for each value of  $k$ ,  $Y_k(\eta)$  satisfies

$$\frac{d^2 Y_k(\eta)}{d\eta^2} = 2\pi i k \eta Y_k(\eta).$$

$Y_k(\eta)$  is the  $k^{th}$  Fourier Harmonic and has the general solution

$$Y_k(\eta) = a_k A_i(\sqrt{2\pi i k} \eta) + b_k B_i(\sqrt{2\pi i k} \eta),$$

where  $A_i$  and  $B_i$  are Airy functions.

Applying the appropriate boundary conditions (equations 5.18 and 5.20)

$$Y_k(\eta) = c_k \frac{A_i((2\pi i k)^{1/3} \eta)}{A_i(0)} \quad (5.25)$$

where  $c_k$  is the  $k^{th}$  harmonic of the Fourier Transform for the wall concentration of the  $i^{th}$  species

$$c(y=0) = \sum_k c_k e^{2\pi i k \xi} \quad (5.26)$$

From this solution, the corrosion/precipitation flux at the wall can be determined from

$$q = D_i \frac{\partial c_i}{\partial y}.$$

By using the values  $A_i(0) = 0.355$  and  $A'_i(0) = 0.259$ , one will arrive at

$$q = 0.730 \left( \frac{2\pi\gamma D^2}{L} \right)^{1/3} \sum_k c_k k^{1/3} \exp(2\pi i k \xi + i \frac{\pi}{6}). \quad (5.27)$$

The phase shift of  $\frac{\pi}{6}$  in the above expression shows that the highest corrosion/precipitation occur out of phase with the highest/lowest concentrations, and therefore highest/lowest temperatures, by a factor of  $\frac{1}{12}$  the total length of the test loop.

This theoretical model is in good agreement with simulations, which numerically solve the full mass-transport equations using a lattice Boltzmann method [61].

Based on the apparent reliability of this model, it will be very useful in making predictions with other liquid-metal corrosion test facilities. A small test facility is currently in design for use at UNLV.

The data and conclusions reported in this work are in good agreement with this model.

#### Oxide Layer Growth - Wagner's Law

A description of the growth rate of an oxide layer on a substrate was developed by Wagner [62], based on the *Tammann* differential equation. [63] Once steady state is reached, where an initial oxide layer has been established, diffusion of metal ions outward and oxygen inward is the slowest process and dictates the rate of oxide growth. Wagner's Theory assumes local thermodynamic equilibrium, even if there is not a global thermodynamic equilibrium. The theory provides a method to predict a growth rate based on measurable quantities. Prior to Wagner, it was assumed that oxide growth was parabolic in nature, namely

$$X^2 = k_p t, \quad (5.28)$$

where  $X$  is the oxide thickness,  $k_p$  (cm/sec) is known as the parabolic rate constant (of steel oxidation in air at the same temperature and oxygen partial pressure), and

$t$  is time. Differentiating this expression with respect to time and rearranging terms yields

$$\frac{dX}{dt} = \frac{k_p}{2X}, \quad (5.29)$$

which shows that the growth rate decreases as the oxide film gets thicker. The kinetics of oxide growth predicated by Wagner's theory are parabolic.

The parabolic rate constant can be calculated as

$$k_p = \frac{4}{3} \int_{p_{O_2}^I}^{p_{O_2}^{II}} f^{-1} D^* d \ln p_{O_2},$$

where  $D^*$  is the tracer diffusion coefficient of Fe in  $\text{Fe}_3\text{O}_4$ , and  $f$  is known as the correlation factor for diffusion (typically about 0.5 for vacancy diffusion and 0.4-1 for interstitials). The tracer diffusion coefficient obeys the relationship

$$D_{Fe}^* [m^2/sec] = 4 \times 10^{-15} \exp \left[ \frac{1.45(eV)}{kT} \right] p_{O_2}^{2/3} + 8 \times 10^3 \exp \left[ \frac{-6.37(eV)}{kT} \right] p_{O_2}^{-2/3},$$

where  $k$  is the Boltzmann constant. The limits in are the oxygen partial pressures at the inner/outer oxide interface ( $p_{O_2}^I$ ) and oxide/LBE interface ( $p_{O_2}^{II}$ ). [64]

Deviations from parabolic behavior can be accounted for by considering the gradual breakdown of the oxide at the LBE interface. *Tedmon* [55][65] developed a model to describe the kinetics of oxide dissolution. In addition to equation 5.29 above, one can also state

$$\frac{dX}{dt} = -k_s \quad (5.30)$$

where  $k_s$  is proportional to a parameter called the volatilization rate constant,  $k_v$  ( $\text{cm}^2/\text{sec}$ ), given by

$$\frac{\Delta M}{A} \left( \frac{g}{\text{cm}^2} \right) = k_v t,$$

the weight loss due to the chemical breakdown of the oxide at elevated temperatures.

Combining two expressions, equations 5.29 and 5.30, gives

$$\frac{dX}{dt} = \frac{k_d}{X} - k_s, \quad (5.31)$$

where  $k_d \equiv \frac{1}{2}k_p$ . Integrating equation gives

$$t = \frac{-X}{k_s} - \frac{k_d}{k_s^2} \ln |k_d - k_s X| + C,$$

where the integration constant,  $C$ , can be found by applying the boundary condition  $X = 0$  when  $t = 0$ . Doing so gives

$$t = \frac{k_d}{k_s^2} \left[ -\frac{k_s}{k_d} X - \ln \left| 1 - \frac{k_s}{k_d} X \right| \right]. \quad (5.32)$$

By setting equation 5.31 equal to zero, the limiting, asymptotic oxide thickness (assuming no spalling) can be found -

$$X_f = \frac{k_d}{k_s}. \quad (5.33)$$

When either  $X$  or  $k_s$  is small, the natural log term in Equation 5.32 can be Taylor expanded -

$$\ln \left| 1 - \frac{k_s}{k_d} X \right| = -\frac{k_s}{k_d} X - \frac{1}{2} \left( \frac{k_s}{k_d} X \right)^2 - \frac{1}{3} \left( \frac{k_s}{k_d} X \right)^3 - \dots - \frac{1}{n} \left( \frac{k_s}{k_d} X \right)^n$$

and substituted into equation 5.32, yielding

$$t = \frac{1}{2} \frac{X^2}{k_d} + \frac{1}{3} \frac{k_s X^3}{k_d^2} + \dots + \frac{1}{n} \frac{k_s^{n-2} X^n}{k_d^{n-1}}. \quad (5.34)$$

When no dissolution of the oxide occurs ( $k_s = 0$ ),  $t$  is parabolic.

The above description, namely equation 5.32, assumes no preoxidation, and therefore is only adequate under such circumstances. A modification to Tedmon's model to conveniently account for kinetics and mass change was developed by Zhang et. al. [59], and proceeds as follows. By parameterizing equation 5.32 with:

$$\begin{aligned} \xi &\equiv \frac{X}{X_f} & \tau &\equiv \frac{t}{t_c} \\ &= \frac{k_s}{k_d} X & &= \frac{k_s^2}{k_d} t \end{aligned}$$

where  $t_c = k_d/k_s^2$  is *twice* (discussed below) the time required to reach asymptotic thickness following a pure parabolic trend (no scale removal), it takes on the dimensionless form

$$\tau = -\xi - \ln |1 - \xi|. \quad (5.35)$$

By a Taylor expansion of the natural log term and transforming the power series to express  $\xi$  as a function of  $\tau$  [66], this expression can be simplified for early stages of oxide growth, in which case it becomes

$$\xi(\tau \rightarrow 0) \approx (2\tau)^{1/2} - \frac{2}{3}\tau, \quad (5.36)$$

where the first term is the pure parabolic term, consistent with the parabolic term in equation 5.34, and the second is a linear scale-removal term. The “2” in the first term accounts for  $t_c$  being twice the time required for the oxide scale to reach asymptotic thickness, as mentioned above. For a system in the steady state, equation 5.35 becomes

$$\xi(\tau \rightarrow \infty) \approx 1 - e^{-(\tau+1)}. \quad (5.37)$$

Equations 5.35, 5.36, and 5.37 are all summarized in the graph of figure 14. Though both the initial and asymptotic trends match the exact solution very well, neither match the transitional period (about  $0.5 \leq \tau \leq 1.5$ ).

If the substrate metal has an initial oxide cover of thickness  $X_0$ , then the initial condition becomes  $t(X_0) = 0$ , and the exact, dimensionless solution becomes

$$\tau = -(\xi - \xi_o) - \ln \left| \frac{1 - \xi}{1 - \xi_o} \right|. \quad (5.38)$$

The mathematical details entailed in evaluating this expression for the possible scenarios is beyond the scope of this text. Reference [59] outlines those very nicely. To summarize it all, there are basically three scenarios: the initial oxide thickness is less than, equal to, and greater than the asymptotic thickness. In the first case ( $\xi_o < 1$

and  $d\xi/d\tau > 0$ ) the oxide grows asymptotically to  $\xi = 1$ . In the second case ( $\xi_o = 1$  and  $d\xi/d\tau = 0$ ), no changes in the system occur. In the third case ( $\xi_o > 1$  and  $d\xi/d\tau < 0$ ) the oxide layer is reduced via dissolution to the asymptotic thickness. [55] These are summarized in figure 15.

# Ellingham Diagrams

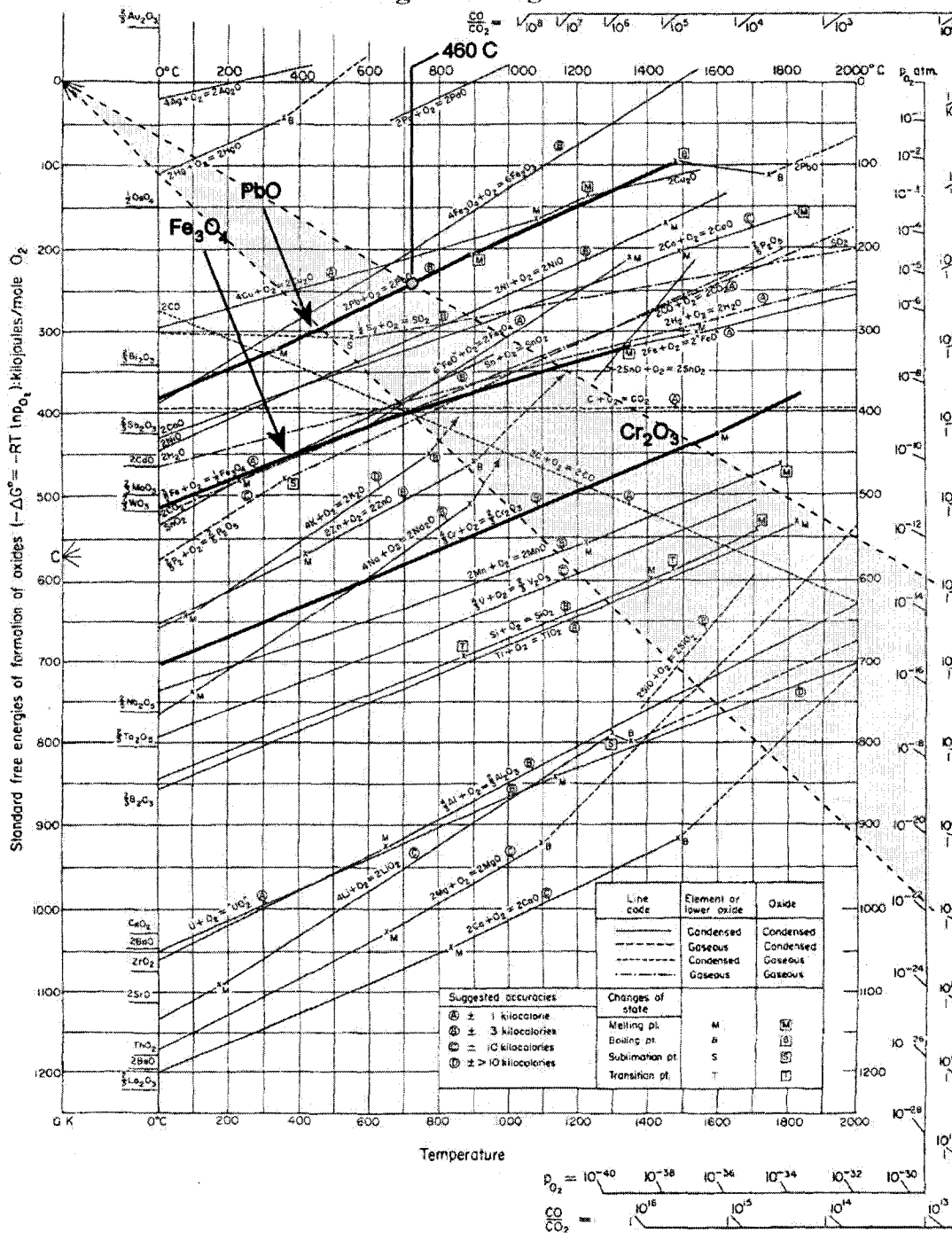


Figure 12 Ellingham Diagram with  $\Delta G^\ominus(T)$  curves labeled for  $Cr_2O_3$ ,  $Fe_3O_4$ , and  $PbO$ . Also indicated is the  $O_2$  partial pressure range in LBE, bound on the upper end by the minimum oxygen needed to oxidized lead at 460 °C and on the lower end the equilibrium  $p_{O_2}$  for the reaction  $3Fe + 2O_2 \rightleftharpoons Fe_3O_4$  at 460 °C. [45]

$c_{sat}$	Fe	Cr	Ni
A	6.01	3.98	5.53
B (K)	-4380	-2280	-843

Table 3 Solubility data for major alloying elements (Equation 5.17).

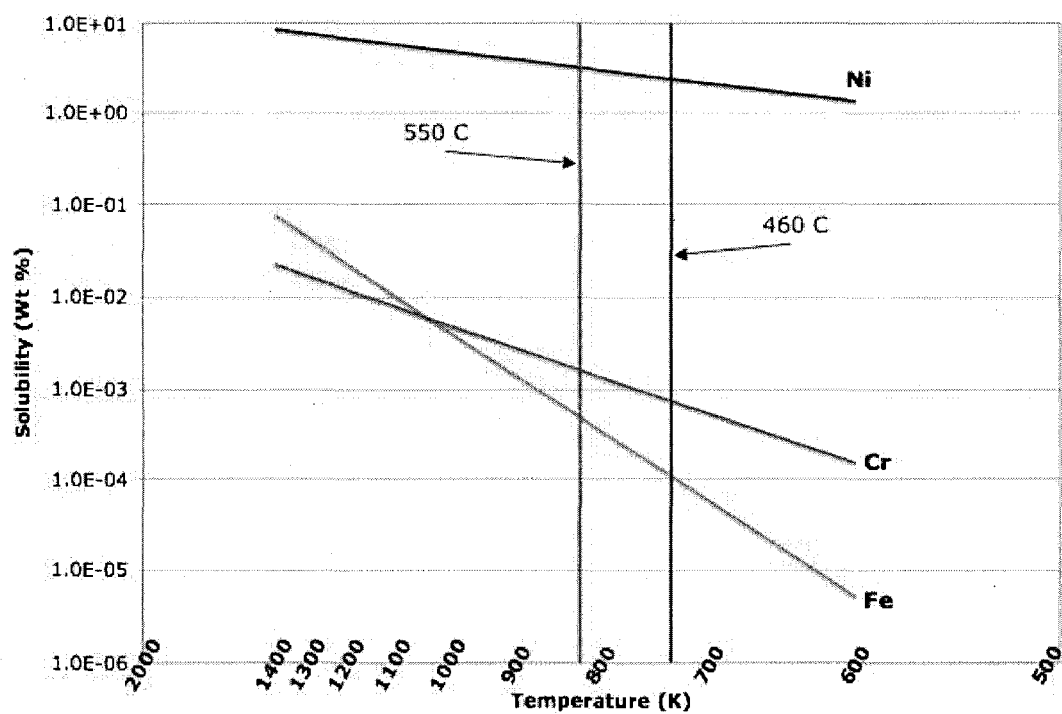


Figure 13 Solubilities of iron, chromium, and nickel in LBE as a function of temperature.



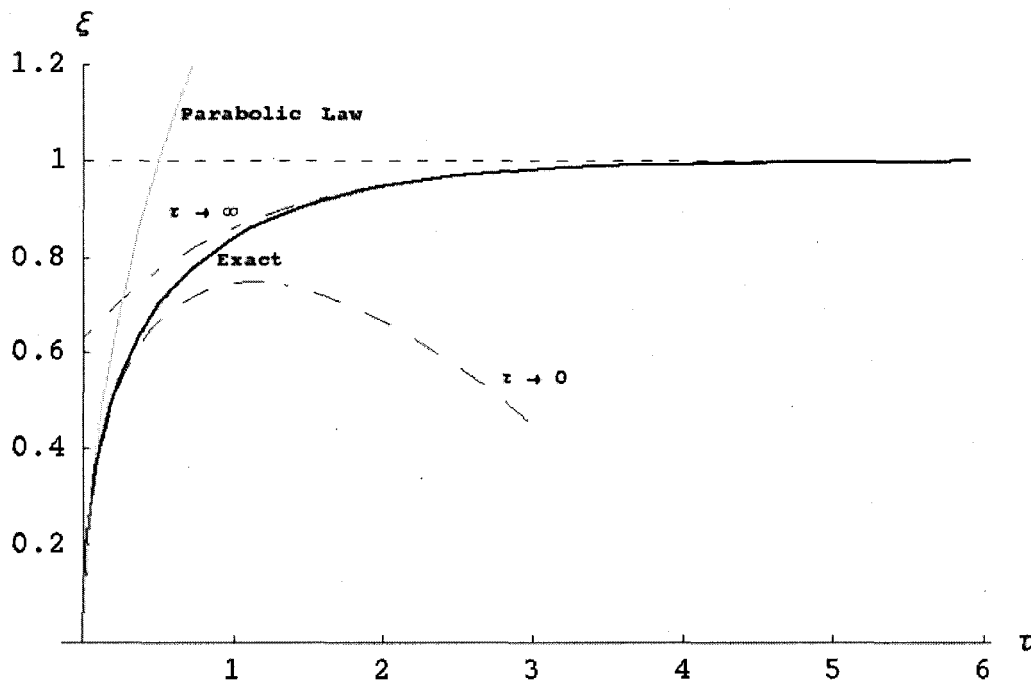


Figure 14 Kinetics of initial ( $\tau \rightarrow 0$ , Eqn. 5.36) and asymptotic ( $\tau \rightarrow \infty$ , Eqn. 5.37) oxide growth compared to the exact solution (dark line, Eqn. 5.35) and a pure parabolic trend (gray line). [59]

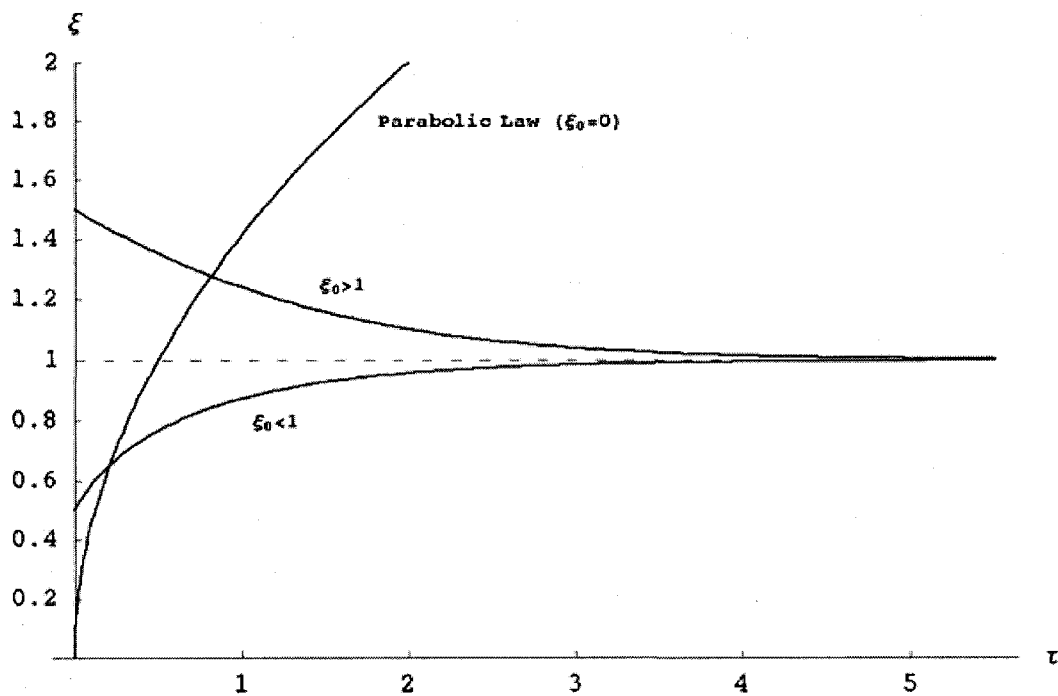


Figure 15 Kinetics of oxide growth with an initial oxide, both when it is thicker than the asymptotic thickness ( $\xi_0 > 1$ ), and thinner than the asymptotic thickness ( $\xi_0 < 1$ ). A pure parabolic trend on a clean substrate ( $\xi_0 = 0$ ) is also plotted for comparison. [55]

## CHAPTER 6

### OTHER STUDIES

In other similar studies, much of what is reported in our work is verified for austenitic stainless steels. Some groups did very similar studies: their steel samples were exposed for durations and temperatures very close to those of our steels. Others used different temperatures and/or different durations. Also, one study is included that presents results on a martensitic steel, as well as a model describing duplex oxide growth that is consistent with the one proposed in this study.

*Glasbrenner et al.* [56] exposed austenitic alloys 1.4948 and 1.4970 (the previous being similar in composition to 316 and the latter being similar to D9) to flowing lead at 400 °C and 550 °C for periods of 1027 h, 2000 h, and 3027 h. The oxygen level in the lead was maintained at  $3\text{--}4 \times 10^{-5}$  percent by weight. Some samples were surface-treated by a pulsed electron beam, a process dubbed “GESA” [67], in which a thin surface area of a sample can be melted and cooled in a short time. The fast cooling process results in very fine grains in the near-surface region (grain size is not reported). They report that the GESA-treated austenitic steels developed multiphase oxide scales, described below. The untreated samples developed a thin, dense oxide layer with a thickness of about 2  $\mu\text{m}$  after being exposed for 3000 h at 550 °C. An inspection of the exposed samples revealed a golden shiny surface which is indicative of a thin oxide layer. The color darkens with exposure time but remained shiny up to the 3000 hour mark. They claim that either type of oxidation is sufficient to prevent dissolution attacks for at least the 3000 hour exposure time; however, in the case of the thicker, multiphase oxide, oxidation corrosion could become a problem at longer

exposure times. The techniques they employed were weighing of test specimens, X-ray spectral microanalysis, metallurgical examination, and EDX analysis on cross-sections of the samples.

*Barbier and Rusanov* [57] performed similar studies on several types of steel, including 1.4970 austenitic steel (similar to D9). However, they used flowing LBE with an oxygen concentration of  $1-2 \times 10^{-6}$  percent by weight. The samples received no surface treatment besides initial machining. They exposed samples to LBE at 300 °C and 470 °C for up to 3116 hours. The austenitic steel showed the greatest resistance to oxidation in LBE. They report no signs of corrosion damage at the maximum exposure time and temperature. They reported no nickel depletion in the austenitic steel even though nickel has a high solubility in lead alloys, as reported by others. [52][53][54][55] X-ray maps and concentration profiles from the oxide/bulk interface show no change in the distribution of the elements, and therefore dissolution did not occur. They measured an oxide layer  $\ll 1 \mu\text{m}$  which apparently provided protection against corrosion. They calculated the oxide layer thickness from weight change measurements, as SEM did not detect it. The techniques they used were SEM/EDX, X-ray diffraction spectroscopy (XRD), and weight analysis.

*Fazio et al.* [11] performed isothermal tests on 316L at 300 °C, 400 °C, and 476 °C for times of 700, 1200, 1500, and 5000 h in stagnant, oxygen-saturated LBE. The nature of any surface work performed was not mentioned. They reported that the austenitic steel 316L exhibited acceptable resistance to oxidation corrosion. At the two colder temperatures with the longest exposure, a thin ( $\ll 1 \mu\text{m}$ ) oxide layer formed. EDS (EDX) analysis showed oxide composition of mostly iron, chromium, and oxygen. Some nickel enrichment was also detected. At 1200 hours at higher temperatures of 464 °C and 476 °C, 316L showed a slightly thicker and nonuniform layer of oxidation growth, ranging from 2 to 4  $\mu\text{m}$ . Nickel enrichment at the oxide/metal

interface was again detected. Using XRD, they reported composition of the corrosion products corresponds to  $\text{Fe}(\text{Fe}_{1-x}\text{Cr}_x)_2\text{O}_4$ .

All three papers mentioned above report the multi-layer oxide formation as mentioned in Chapter 4, under "Dissolution Corrosion by LBE". The layers are: an outer magnetite ( $\text{Fe}_3\text{O}_4$ ), an intermediate spinel  $\text{Fe}^{2+}(\text{Fe}_{1-x}^{3+}\text{Cr}_x^{3+})_2\text{O}_4(+\text{Ni})$ , and an innermost oxygen diffusion layer.

According to *Li* [52][53][54][55] and *Barbier et al.* [57], nickel has the highest solubility and therefore we predict it to be the first alloying element diffused out of the bulk and dissolved into the LBE. At first glance, our data seem to agree with that claim. However, *Glasbrenner et al.* [56] claim that nickel is in the deepest regions of the oxide layer and at the the oxide-bulk interface. From quantitative linescans taken with WDS in this report, nickel is shown to be enhanced above its alloy concentration in the inner oxide (Figures 25 and 27).

LBE corrosion tests were performed by *Li et al.* [12] on 316L samples that had been surface-treated. Initially annealed, the samples had average grain size of 35  $\mu\text{m}$ . Surface-treated samples were shot-peened, which is a form of cold-working, by blasting one surface with aluminum oxide powder at 55 psi for 15 s. The resulting surface had a roughness of approximately 0.9  $\mu\text{m}$  and a damage depth of about 30  $\mu\text{m}$ . The shot-peened samples were subsequently polished. The shot-peened/polished sample showed no sign of corrosion compared to the untreated (annealed) sample. The proposed mechanism for such corrosion/oxidation resistance on the treated sample is rapid chromium diffusion to the surface.

*Martinelli et al.* [68] performed LBE corrosion tests on T91, a martensitic alloy (9Cr1Mo steel with 0.18-0.25 % V and 0.06-0.10 % Nb) at 470 °C both in oxygen-saturated LBE and dry air. The corroded samples were examined with SEM/EDX, glow discharge optical emission spectroscopy (GD-OES), secondary ion mass spec-

trometry (SIMS), and XPS. They also propose a model to describe the nature of duplex oxide growth, based on the “available space model”, a process ascribed to *Brückman* and *Romanski* [69]. The model basically dictates that the growth of the inner oxide is entirely dependent on vacancies left by outward diffusing iron. Consequentially, all oxide growth is limited by iron diffusion in the oxide lattices. The details of the model are rich and the article is highly recommended to gain good insight into the mechanism.

Assuming no mass loss to dissolution, Martinelli et al. presented mass conservation equations which show the thickness of the inner spinel layer,  $h_{sp}$ , as a function of the outer magnetite layer,  $h_{mag}$ , dictated by the available space model:

$$h_{sp} = \frac{C_{Fe,mag}}{C_{Fe,bulk} - C_{Fe,sp}} h_{mag},$$

where  $C_{Fe,mag}$  is the concentration of iron in the magnetite layer,  $C_{Fe,bulk}$  is the concentration of iron in the bulk steel, and  $C_{Fe,sp}$  is the concentration of iron in the spinel layer. All three iron concentrations are determined from atomic percentages obtained by x-ray and microprobe analysis. The thickness of the magnetite layer is calculated from theoretical diffusion models and parabolic growth models, using experimentally determined parameters (e.g. iron diffusion coefficient similar Fe-Cr spinels) from the literature.

Martinelli et al. find a thick ( $\approx 16 \mu\text{m}$ ) outer  $\text{Fe}_3\text{O}_4$  scale of columnar grains that is porous and has lead inclusions after 7800 h exposure to LBE. They observed a thick ( $\approx 14 \mu\text{m}$ ) inner oxide spinel with the formula  $\text{Fe}_{2.34}\text{Cr}_{0.66}\text{O}_4$ , the stoichiometry of which was determined by microprobe analysis and by assuming a  $\text{Fe}_{3-x}\text{Cr}_x\text{O}_4$ -type spinel. They also found lead penetration as deep as the oxide/metal interface. They propose that the spinel oxide grows inward from the original metal interface by oxygen diffusion inward, and the outer oxide grows outside the original metal interface by iron diffusion outward. Oxygen diffusion in the oxide lattices is several orders of

magnitude too low to account for the inner oxide growth. What is likely providing oxygen is lead channels through the oxide layers, as the diffusion of oxygen in lead is much greater. They also note that chromium concentration in inner oxide is the same as in the bulk metal. Therefore chromium it is not highly mobile. The results of the dry air tests are drastically different: oxide formed in LBE grows approximately 100 times faster than that formed in air, even with  $p_{O_2,air} = 4000 \cdot p_{O_2,LBE}$ . Their calculations are in very good agreement with their results, which is notable because they show that mass loss to metal dissolution in LBE is minimal. Their simulations on the growth of a magnetite layer assumed the dynamics of lattice diffusion for iron, as opposed to grain boundaries. Given the good agreement of their model with measurements, iron diffusion through the grain lattices is plausible.

## CHAPTER 7

### SEM/EPMA RESULTS

#### Introduction

Data obtained using the SEM and EPMA apparatuses incorporate several crucial aspects regarding quantification and classification of the corroded steels. In just about any journal article about these types of studies, sample analysis includes some kind of electron microscopy. It is one of the most widely employed techniques in surface science. In most cases SEM is easy to use and, therefore, takes little training on the part of the user. A good understanding of how an electron beam interacts with a material can yield much more information than just nice images and basic identification of abundant elements. This was discussed in Chapter 4.

#### Surface - Data and Results

The surface images and the EDX spectral data of Figure 16 show that the surface of the corroded sample is covered by oxygen-containing compounds, consisting primarily of iron oxides. The EDX spectrum the annealed 316L stainless steel tube before exposure to LBE shows high abundances of chromium and iron, with a smaller amount of nickel and a few other trace elements. The zinc peaks were surprising, but are clearly present, and were found in XPS data. [70] No oxygen peaks were observed in the spectrum of the unexposed, annealed 316L, indicating that the oxide layer is very thin and does not contribute a detectable peak. However, oxygen did appear in the XPS data, as discussed below. The spectrum taken from an identical tube that has been exposed to LBE for 3000 hours at a temperature of 550 °C, the longest and hottest exposure in a number of tests. For the exposed sample, the spectrum shows



high abundances of iron and oxygen, with very little chromium. This suppression of chromium in the exposed sample is confirmed in the XPS data, which are discussed below. This is also indicated by the XPS data, which will be discussed below.

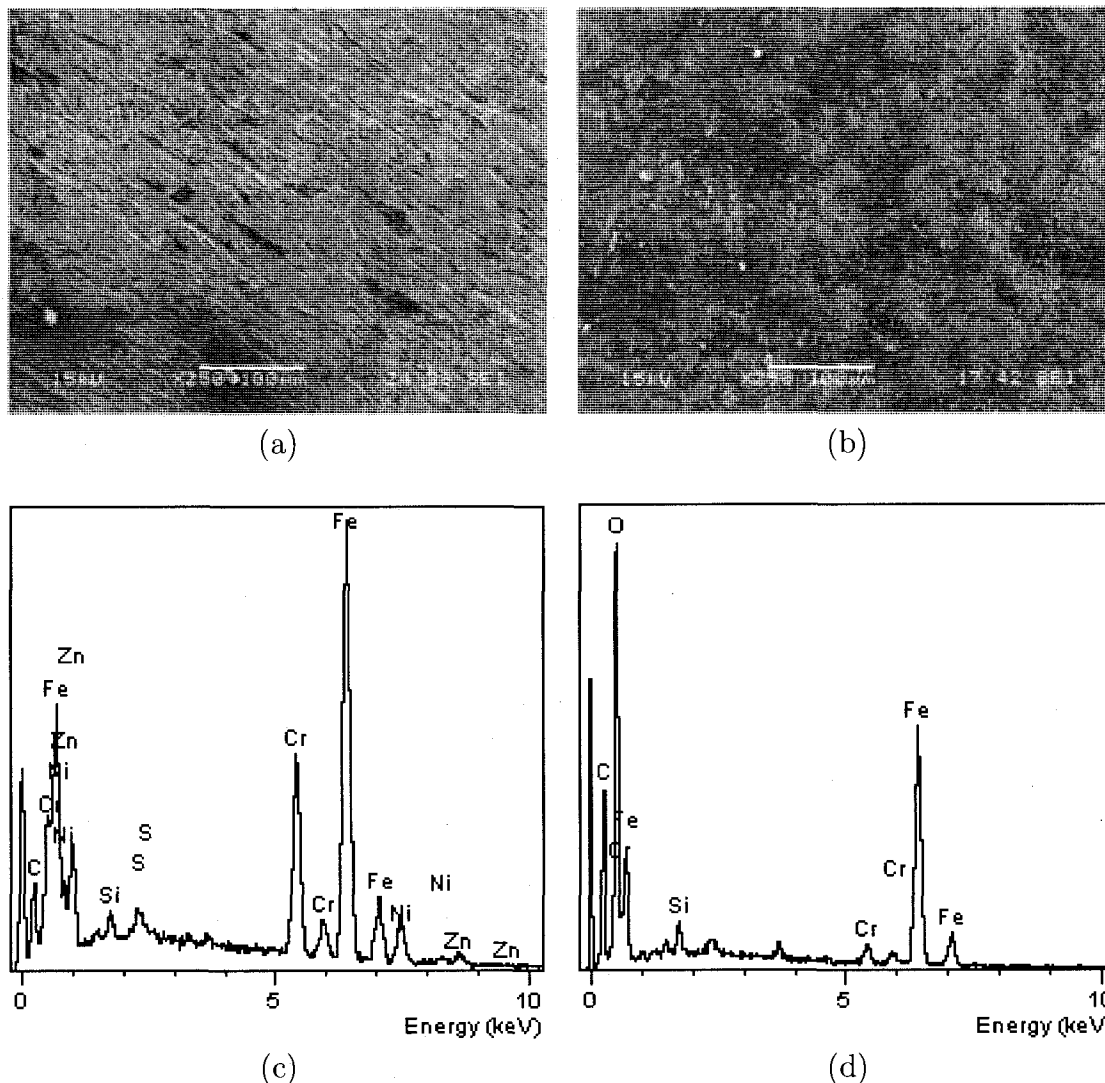


Figure 16 (a) SEM image of the surface of unexposed annealed 316L sample reveals the fresh steel surface without exposure to LBE. (b) Surface of the exposed, annealed 316L steel sample is drastically different when viewed at the same magnification as (a). Each image is about 500  $\mu\text{m}$  across. (c) EDX spectrum of annealed 316L steel sample, not exposed to LBE. (d) EDX spectrum of an annealed 316L steel sample, exposed to LBE for 3000 hours at 550  $^{\circ}\text{C}$ .

An EDX spectrum of the surface of the cold-rolled 316L sample give indications that it is covered by a thin layer of iron and chromium oxides. Further evidence of the nature of this oxide cover being very thin and consisting of iron and chromium oxides is revealed below. The unexposed cold-rolled 316L sample looks quite different than the annealed sample, though their EDX spectra indicate practically identical surface compositions (Figure 17).

Annealed samples exposed for shorter times show a morphology consisting of some areas covered by oxides, and other areas uncovered. EDX spectra of uncovered areas reveal significant differences from those of the covered areas (Figure 18). The level of chromium in the uncovered area is much higher than the level of chromium in the covered area. While chromium is present in the uncovered (but not covered) areas, oxygen is present in the spectra of both areas. For the covered area, the chromium is covered by iron oxides, as it is consistent with the data on the completely covered annealed 316L steel. In short, chromium oxides are present only in the uncovered areas, while iron oxides are present in both covered and uncovered areas. It is also noteworthy that the uncovered areas are very characteristic of the surface of the exposed, cold-rolled sample (Figure 17). XPS studies are used to investigate the chemical states of the surface species and establish what elements are oxidized (Chapter 8).

A similar trend to that of the 2000 hr annealed 316L occurs on D9. D9 also shows partial thick oxide coverage, which increases with exposure time (Figure 19). An EDX spectrum taken on an uncovered area (marked "a") shows mostly just iron and oxygen, with suppressed chromium. Conversely, a covered area (marked "b") still shows strong oxygen. However chromium is roughly as abundant as iron.

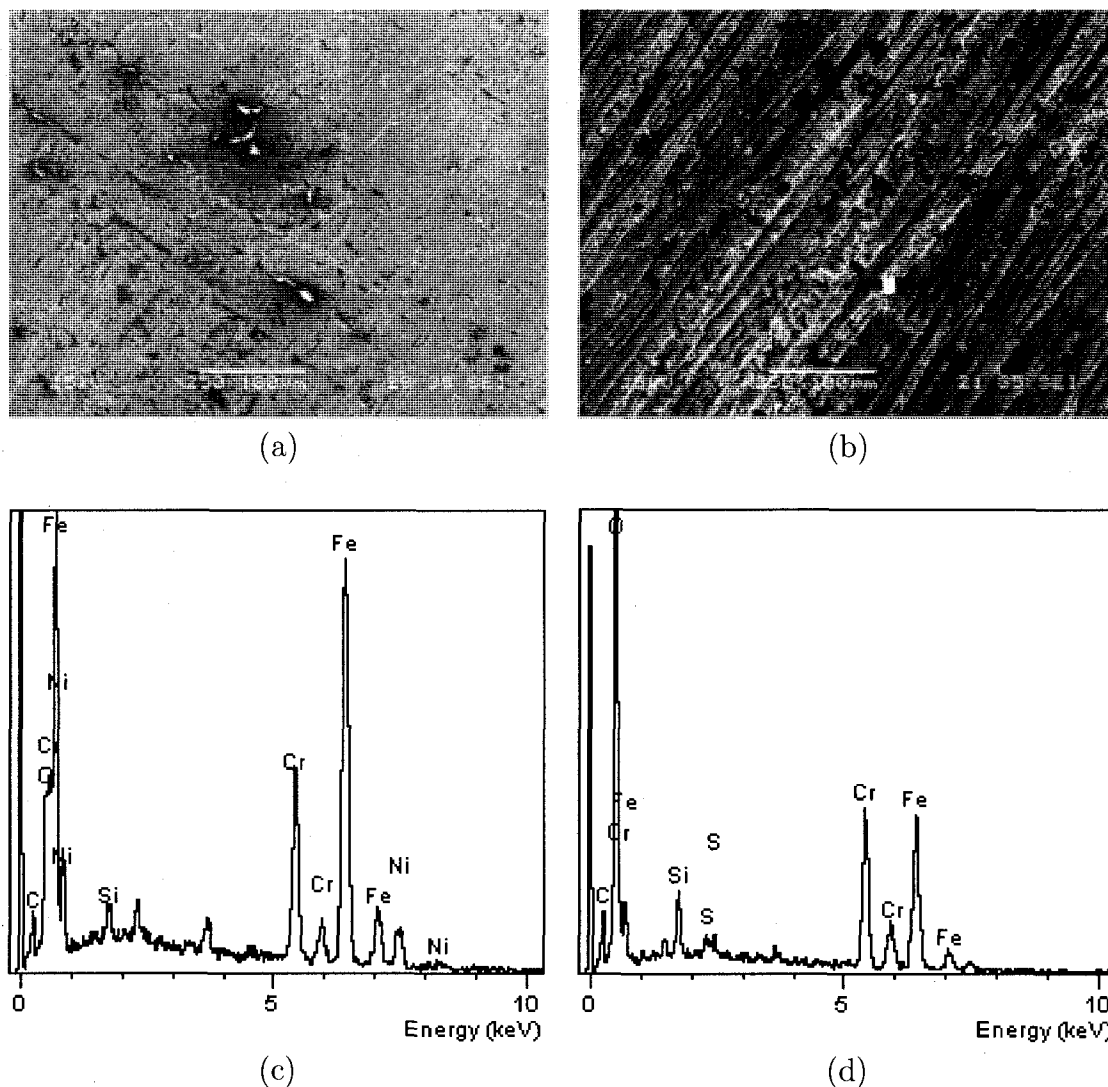


Figure 17 (a) SEM image of the surface of unexposed cold-rolled 316L sample reveals the fresh steel surface without exposure to LBE. (b) Surface of the exposed, cold-rolled 316L steel sample is drastically different when viewed at the same magnification as (a). Each image is about  $500\ \mu\text{m}$  across. (c) EDX spectrum of cold-rolled 316L steel sample, not exposed to LBE. (d) EDX spectrum of a cold-rolled 316L steel sample, exposed to LBE for 3000 hours at  $550\ ^\circ\text{C}$ .

## Cross-Sectional Data and Results

### SEM/EDX

In cross-section, the duplex nature of the oxide layers on the D9 sample is clearly evident in Figure 20. From the elemental maps (Fig 20), it can be seen that the outer

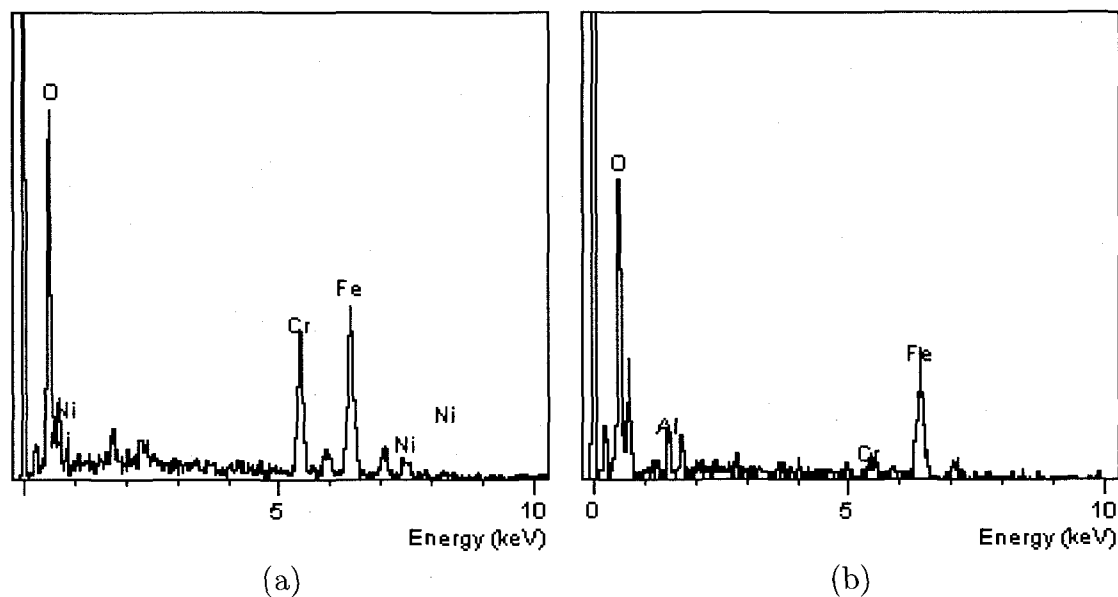
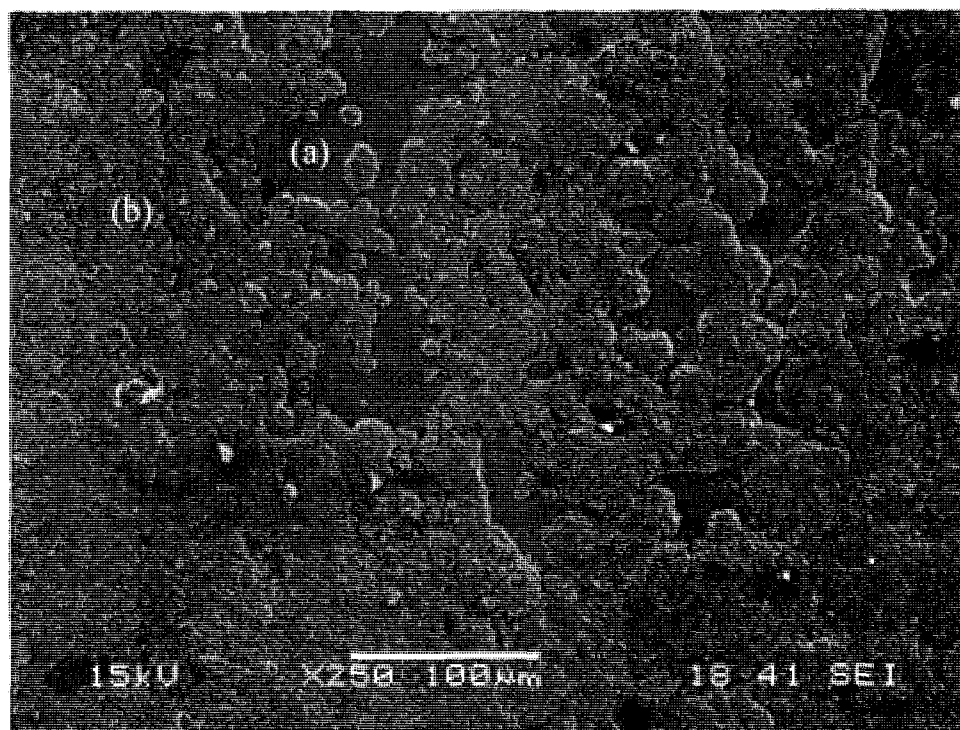


Figure 18 SEM of an annealed 316L steel sample exposed to LBE for 2000 hours at 550 °C shows some uncovered areas where the original surface is still visible (top image). Regions marked “(a)” and “(b)” in the image correspond to the respectively labeled EDX spectra.

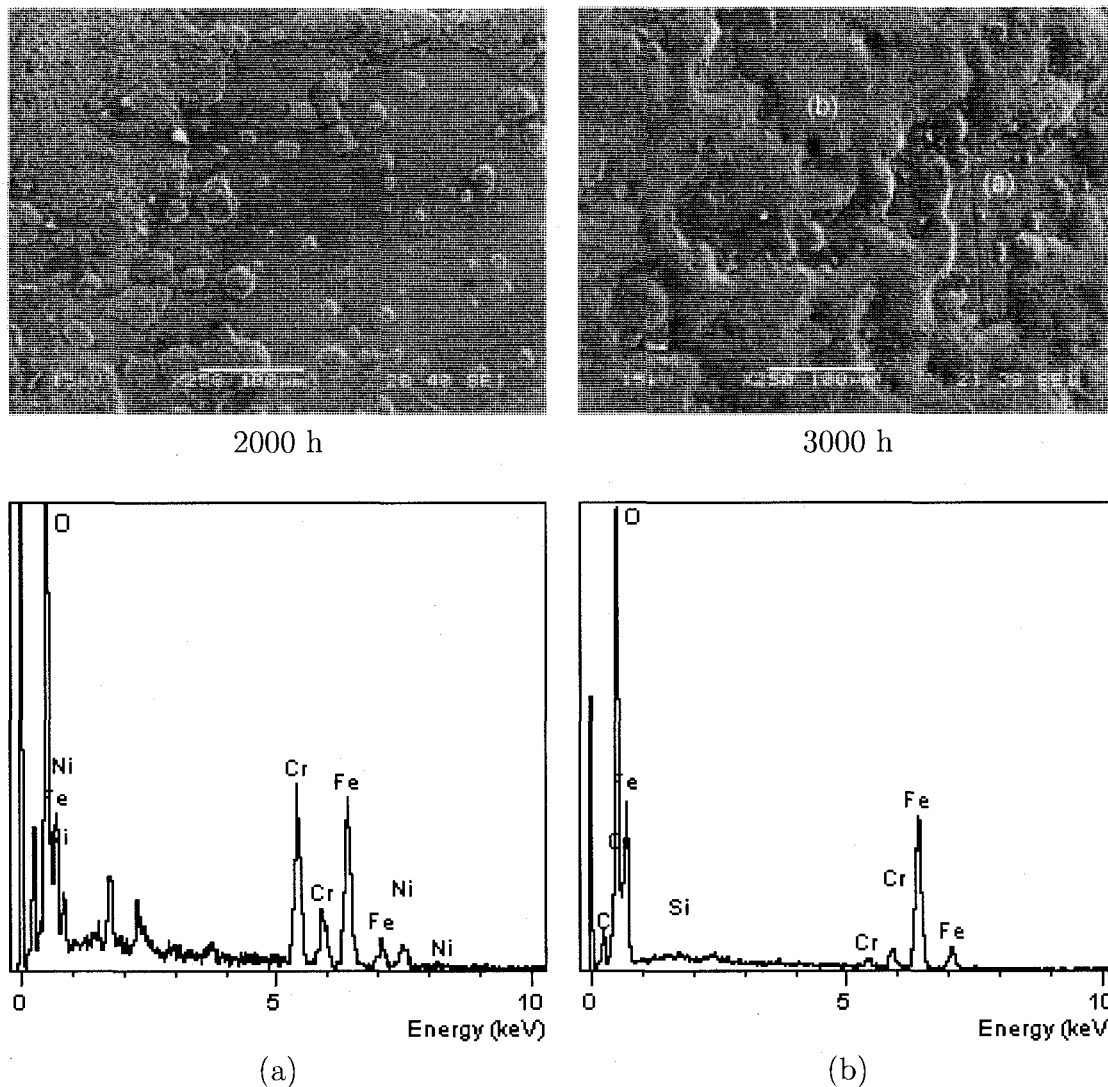


Figure 19 SEM of D9, exposed to LBE for 2000 h and 3000h at 550 °C show some uncovered areas where the original surface is still visible. Regions marked “(a)” and “(b)” in the 3000 h image correspond to the respectively labeled EDX spectra. Each image is about 500  $\mu\text{m}$  across.

oxide consists iron and oxygen, with some lead inclusions (trapped LBE). The inner oxide layer consists of chromium, some iron, and nickel (see Figure 21 for a better nickel map). It should be noted that the growth of the inner oxide follows the grain pathways at short exposure times. At longer exposure times the inner oxide/bulk metal boundary flattens out. Figure 21 shows a highly detailed elemental map of the

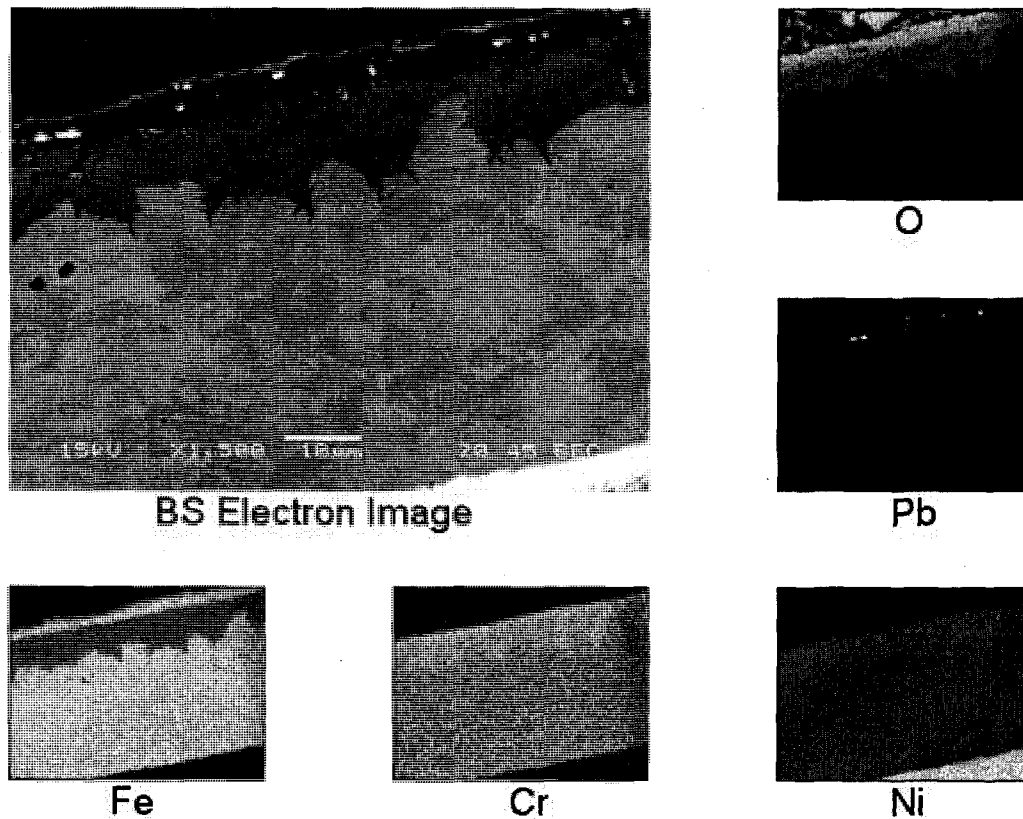


Figure 20 SEM backscattered electron image of the D9 steel sample, exposed to LBE for 1000 hr, and EDX elemental maps of the same region.

inner oxide on the 1000 h exposure D9 sample. Some key features to note include the enhancement of oxygen, silicon, and chromium in the grain boundaries within the oxide. Nickel is noticeably depleted in the oxide grain boundaries, although it generally enhanced in the inner oxide as a whole. Conversely, nickel is slightly enhanced in the bulk grain boundaries, while chromium is slightly depleted there. The interface between the inner oxide and the metal is rough in the 1000 h D9 sample, following the general grain structure (Figure 20). However, at 3000 h the inner oxide/metal interface is very straight, as seen in an optical microscope (Figure 22).

The annealed 316L sample is similar to D9 in that it has a duplex oxide structure. However, the dynamics of the inner oxide are more difficult to deduce. Figure 23

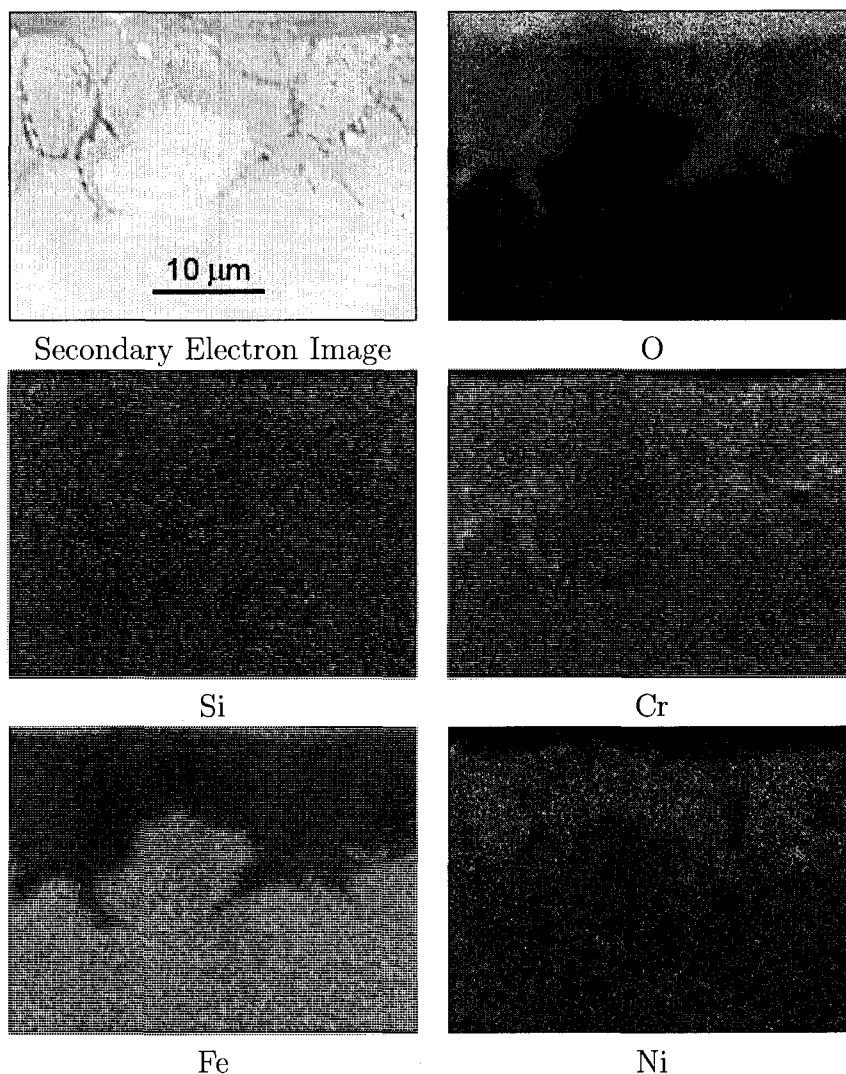


Figure 21 Hi-res EDX elemental map of the inner oxide on a D9 steel sample, exposed to LBE for 1000 hr.

is an image of the oxide layers in cross section, as well as a higher magnification elemental map of a region of the oxide. The map shows an outer iron-based oxide (likely magnetite) and an inner oxide that follow the original grain structure of the steel, and propagates along grain boundaries. The inner oxide consists of mostly oxygen, chromium, and nickel. Oxygen is enhanced in the grain boundaries, though there are some voids in the oxygen map. Chromium closely mimics the oxygen map. Nickel is likely metallic, though it can also exist as a spinel oxide with chromium,



Figure 22 Optical microscope image of D9, exposed to LBE for 3000 hr.

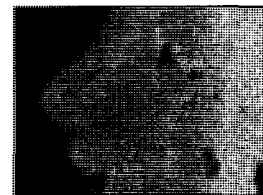
nickel chromite. Iron is present, though depleted in the inner oxide compared to the outer oxide and bulk. Iron is likely oxidized in the inner oxide, although it is evidently metallic (both nickel and iron are enhanced in the oxygen “voids” mentioned above).

The cold-rolled 316L sample has a thin oxide covering most of its surface, with occasional small regions of thick duplex oxide (Figure 24). From the elemental maps one of the rare, small regions of duplex oxide growth can be seen, as well as the typical thin oxide coverage (Figure 24). The duplex oxide is similar to the annealed sample and the D9 sample in that it is iron based in the outer layer and chromium enhanced in the inner layer. Nickel, however, seems depleted in the inner layer. Due to resolution limitations, the composition of the thin oxide will be discussed in the next chapter on XPS and sputter-depth profiling.

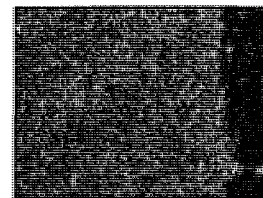




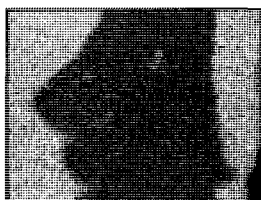
**Secondary Electron Image**



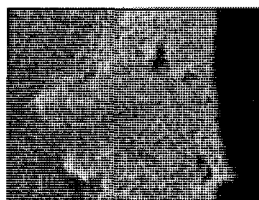
**O**



**Pb**



**Fe**



**Cr**



**Ni**

Figure 23 SEM image and EDX elemental maps of the annealed 316L steel sample, exposed to LBE for 3000 hr. The box is the region mapped. The voids in the oxygen map (dark areas) are rich in iron and nickel. Note - each map is about 30  $\mu\text{m}$  in width.

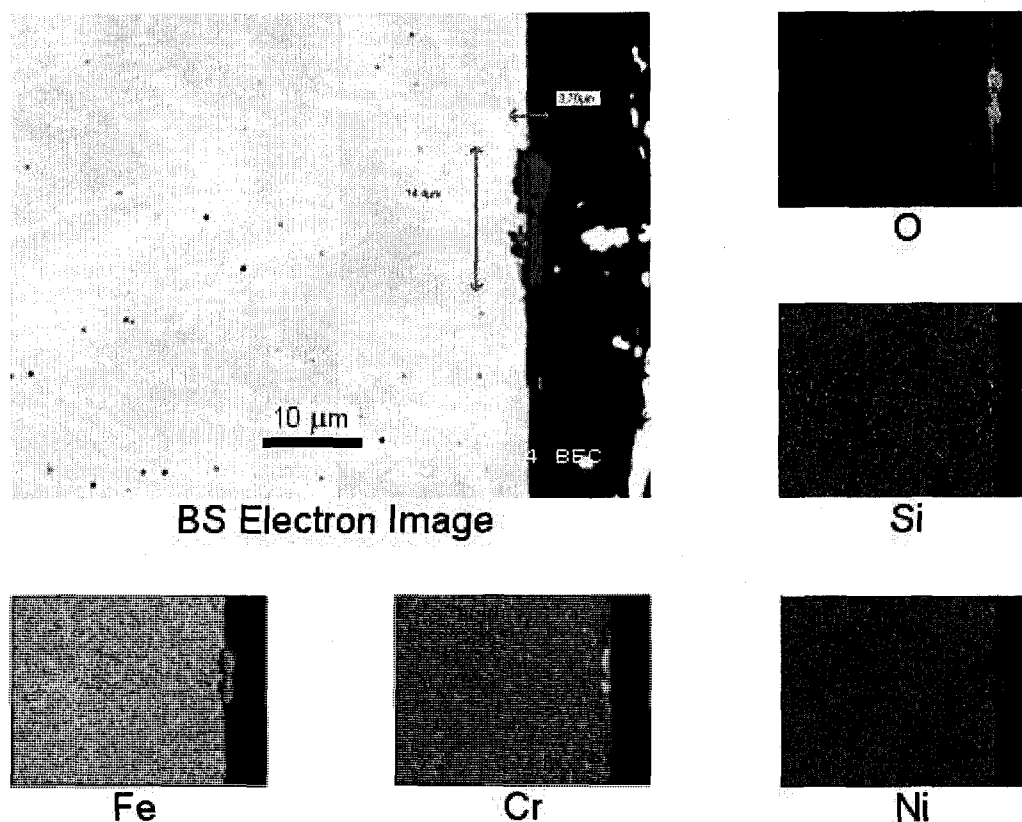


Figure 24 SEM backscattered electron image and EDX elemental maps of the cold-rolled 316L steel sample, exposed to LBE for 3000 hr.

#### WDS Linescans

Quantitative linescans taken on the D9 samples show weight percentages of the elements present as a function of depth, with a spatial resolution of about a micron. Figure 25 is an EPMA backscattered electron image and corresponding linescan on the 1000 hour sample. The linescan starts outside the outer oxide of the sample, in the epoxy, crosses both outer and inner oxide layers, and continues into the bulk. It also crosses an oxidized grain boundary in the bulk. The outer oxide is about 5 microns thick and is composed of iron and oxygen. Iron is about 69% and oxygen is about 29% by weight percent, giving an iron to oxygen weight ratio of about 2.4. The iron/oxygen ratio in magnetite ( $\text{Fe}_3\text{O}_4$ ) is about 2.3 and in hematite ( $\text{Fe}_2\text{O}_3$ ) it

is about 2.6. The ratio on this sample is therefore closer to that of magnetite, which is not absolutely conclusive, but Raman studies [58] verify the identity of the outer oxide as magnetite. Following the linescan inward (Figure 25), chromium quickly

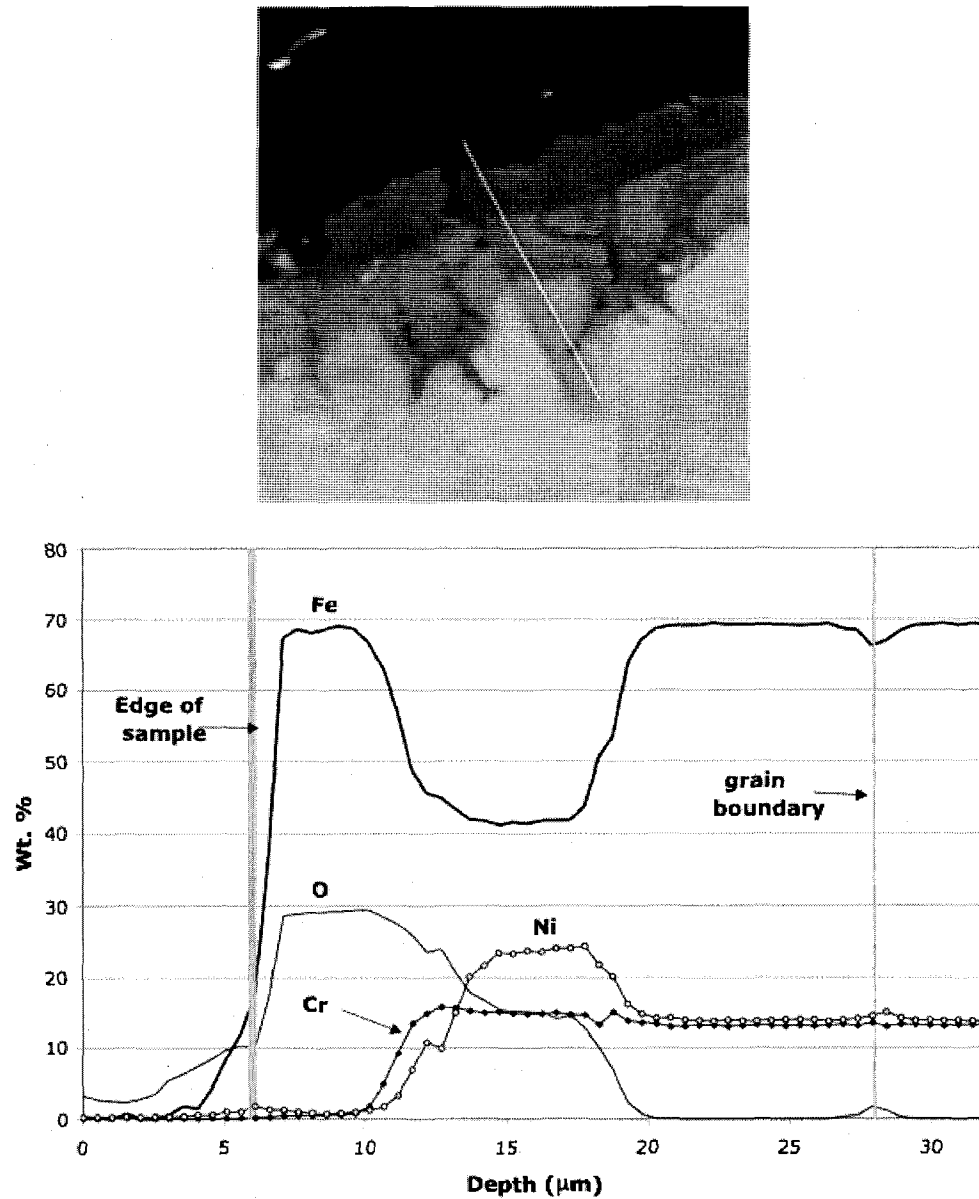


Figure 25 EPMA backscattered electron image (top) showing the location of a linescan (bottom) on the D9 steel sample, exposed to LBE for 1000 hr.

appears at about 5  $\mu\text{m}$  at 15-16 wt. percent. At this same point oxygen is falling and eventually reaches about 15%. About 2  $\mu\text{m}$  after the depth at which chromium appears, nickel quickly shows up and rises to 23-24 wt. percent. In this inner oxide region iron has fallen to 41-42 wt. percent. It is difficult to simply calculate elemental ratios to deduce the type of oxide present, as the exact nature of the oxide is not known. However, it is claimed in many other studies [55][59][64][71] that the inner oxide is some type of iron-chromium spinel and nickel-chromium spinel (especially for nickel-rich, austenitic steels [72]). Even with the insight from the literature, the information is still too vague to determine the exact chemical nature of the spinel oxide. Some portion of the chromite spinel could be inverse, in which cases the Fe/Cr and Ni/Cr ratios flip (1:2 to 2:1). Moreover, though nickel is greatly enhanced (compared to its concentration in the alloy) in the inner oxide, XPS data (see next chapter) reveal that it is mostly metallic in the inner oxide region.

At about 12  $\mu\text{m}$  from the oxide/LBE interface, the inner oxide ends and the elements reach their bulk values (69% iron, 14% chromium, 14% nickel, 0% oxygen). The last feature to notice is the grain boundary that the linescan intersects. Since the grain boundary is only briefly encountered, the shifts in weight percentages are small. Nonetheless, the nature of the oxide in the grain boundary is probably the same as the inner oxide (Figure 25).

Previous WDS linescans were taken on the 1000 h sample that included manganese and silicon. Figure 26 is a linescan of all of the elements with a close-up on the manganese and silicon graphs.

The D9 sample exposed for 3000 h is very similar to the 1000 h sample except that both outer and inner oxides are thicker (7-8  $\mu\text{m}$  outer oxide, 18-20  $\mu\text{m}$  inner oxide). Again it is noteworthy that chromium appears 1-2  $\mu\text{m}$  before nickel does, and nickel is enhanced in the inner oxide with respect to its bulk concentration, to

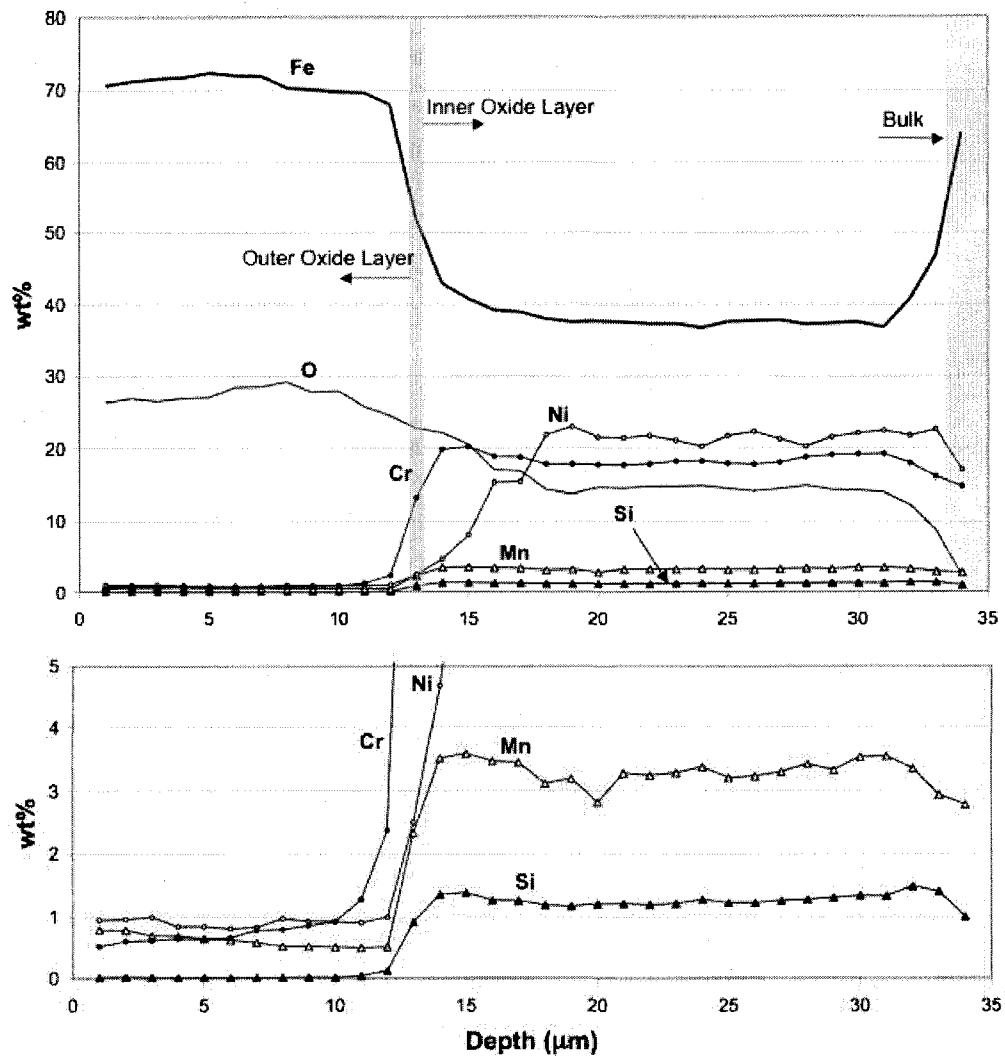


Figure 26 Previous WDS linescan of the D9 steel sample, exposed to LBE for 1000 h. The bottom graph is a close-up of Mn and Si.

about 25 % in the 1000 h sample and 20 % in the 3000 h sample. Also, this linescan traverses a couple of grain boundaries within the inner oxide region, where chromium and oxygen increase by 2–3 %, and nickel decreases by 4–5 % (Figure 27).

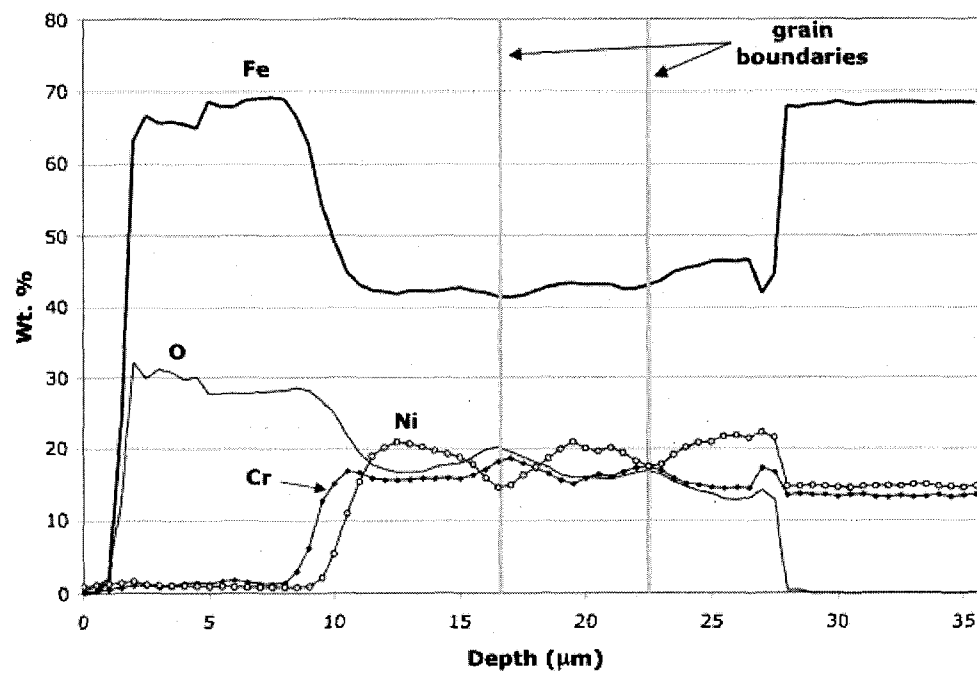


Figure 27 EPMA backscattered electron image (top) showing the location of a linescan (bottom) on the D9 steel sample, exposed to LBE for 3000 hr. The boundary between the outer and inner oxides occurs at about 9  $\mu\text{m}$ .

## Oxide Growth Rate

Measurements of oxide layers as a function of time were taken and fit to the model described in Chapter 5, equation 5.32. The method of oxide thickness measurements is described here. Grayscale images of the cross-sections of oxide layers are modified in a specific way, such that a program written by *John Kilburg* can return pixel values from the edges of the oxide layers in the images. First, the image has to be oriented such that the oxide layer(s) is horizontal. Then by increasing the color depth to include RGB colors, the outside of the outermost layer is traced with red (RGB value 255,0,0). Then the interface between the inner and outer oxide layers is traced in green (0,255,0). Next the metal/inner oxide interface is traced in blue. Lastly, the left and right edges of the traced region need to be indicated so the program knows when to start noting pixels. This is done with a yellow (255,255,0), “starting” line on the left and a teal (0,255,255), “finish” line on the right. The lengths of the yellow and teal lines have to match the first red and blue pixels on the left and the last ones on the right (Figure 28).

When the program has finished, pixel coordinates can be loaded into a spreadsheet. For a given vertical pixel column there are three coordinates – the outer edge of the outer oxide, the interface between the inner and outer oxide, and the interface between the inner oxide and the bulk metal. By subtracting the y-values of the coordinates, the oxide thicknesses can be found in pixel lengths. By multiplying by the appropriate scaling factor ( $X \mu\text{m}/\text{pixel}$ , determined by the scale bar in the image), the thicknesses in microns are determined. This method of determining thicknesses is very useful in that visual biases are minimized and many measurements (data points) are acquired for good statistical analysis, especially when an oxide varies dramatically in thickness.

The method that was used to fit the model to the data was a nonlinear, least-squares fit. The “NonlinearRegress” function in *Mathematica*<sup>TM</sup> was used to calculate

the least-squares, and it allows for weighting of data points. Weighted fits were performed, utilizing 1/variance as the weighting parameter. Results of the oxide thickness measurements fitted to the growth model are summarized in (Table 4).

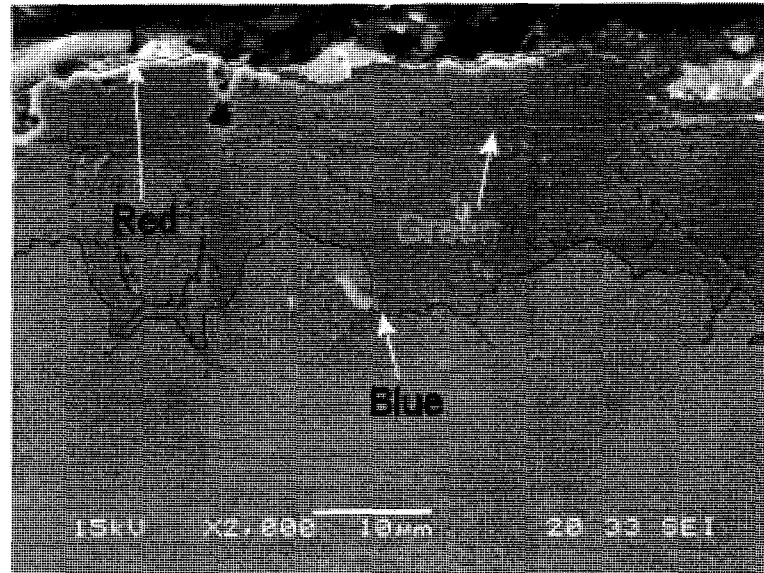


Figure 28 An example of an image that is prepared to be input to software that outputs coordinates of oxide layer boundaries. Image is of the D9 steel sample, exposed to LBE for 1000 h.

Time (hours)	Average $X$ ( $\mu\text{m}$ )	$k_p(\frac{m^2}{s}), k_s(\frac{m}{s})$ (fit)	$k_p, k_s$ (Ref. [55])	$X_f$ (fit)	$X_f$ (Ref. [55])
1000	$16.7 \pm 2.6$	$8.61 \times 10^{-17}$ ,	$6.87 \times 10^{-17}$ ,	469 $\mu\text{m}$	49 $\mu\text{m}$
2000	$26.0 \pm 4.0$				
3000	$29.6 \pm 2.3$	$9.17 \times 10^{-14}$	$7.04 \times 10^{-13}$		

Table 4 Results of average oxide thickness measurements and growth rates on D9, exposed to LBE for 1000 h, 2000 h, and 3000 h.

The values in the table do not agree closely to those reported by Zhang et. al. [55]. The model they used is based on the same principles used in this report (Tedmon model), but applied to weight changes of the samples as a function of exposure time,



rather than oxide thicknesses. Their value of  $k_p$  is fairly consistent with the value reported here, having a percentage difference of 22 %, but the value for  $k_s$  in the reference is nearly an order of magnitude larger. The difference in  $k_s$  is most evident in the final oxide thickness, where the order of magnitude difference is reflected. The implications of this difference is manifested in the lifetimes of the steels. If the values reported here are accurate, then the thickness of the oxide layer at 3000 h is only 6.4 % of the asymptotic oxide thickness. According to Figure 14, the oxide growth model doesn't deviate significantly from a pure parabolic trend until the oxide thickness is about 40 % of the final thickness. Therefore, it is concluded here that performing a fit with just the parabolic term of equation 5.34 is reasonable, and the parabolic growth constants of both fits should agree. A weighted convolution of the pure parabolic function with the data yields  $k_p = 8.16 \times 10^{-17}$ , compared to the Tedmon model value of  $k_p = 8.61 \times 10^{-17}$  (both in  $m^2s^{-1}$ ), a difference of 5.4 %. The major weakness of these results is that the estimated value of the volatilization constant,  $k_s$ , is dubious since the higher order terms of the expansion (eqn. 5.34) are negligible. This elicits carrying out experiments for much greater times to determine the loss rate of material and give credence to the model. However, to reach an oxide thickness that necessitates incorporating higher order terms could easily require exposure times an order of magnitude greater (several years) than those reported here. This is not practical in the sense of carrying out experiments in a timely and cost-effective manner.

Although the final thickness values reported above do seem very large, it's not surprising considering the model used, that is, a one-dimensional model for oxide layer growth. As mentioned above (Figure 19), the growth of corrosion layers on D9 clearly do not display one-dimensional behavior. The average oxide thickness is determined only from areas where duplex oxide is present, and does not represent

the total exposed surface of the sample. If the outward growth of the oxide (the thickness) is still described well by the values measured in this research, then the lateral growth that accounts for coalescence of localized growths can be ignored, which is the assumption to be made if the calculations here are to be regarded as tenable. A model describing a two-dimensional system is an area of ongoing investigation.

### Available Space Model

A modification to the Available Space Model, mentioned in Chapter 6, is needed if it is to be applied to D9. The model presented by *Martinelli et al.* [68] describes a binary alloy of approximately 91 % Fe and 9 % Cr (ignoring minor alloying components). The balance equations, which assume no mass loss (consistent with the negligible material loss concluded in the previous section), describing the conservation of mass (space made available = space filled by oxide) for iron and chromium are:

$$C_{Fe,met}X_{met} = C_{Fe,sp}X_{sp} + C_{Fe,mag}X_{mag}, \quad (7.1)$$

$$C_{Cr,met}X_{met} = C_{Cr,sp}X_{sp}, \quad (7.2)$$

where  $C_{Fe,met}$ ,  $C_{Fe,sp}$ , and  $C_{Fe,mag}$  in equation 7.1 are the weight percentages of iron in the metal, spinel (inner layer), and magnetite (outer layer), respectively, and are determined from WDS quantitative linescan data. The same labels apply to chromium in equation 7.2; however, chromium does not appear in the outer layer. The values  $X_{met}$ ,  $X_{sp}$ , and  $X_{mag}$  are the thicknesses of the iron-depleted zone, spinel layer, and the magnetite layer, respectively.  $X_{sp}$  and  $X_{mag}$  are measured from the SEM images of the oxide layers via the method described in the “Oxide Growth Rate” section above.  $X_{met}$  is inferred from equation 7.2 as follows: it is seen in the WDS linescans (Figures 25, 26, and 27) that the concentration of chromium does not change from the

bulk metal to the spinel oxide layer. As such,  $X_{met} \equiv X_{sp}$ , and equation 7.1 becomes

$$X_{sp} = \frac{C_{Fe,mag}}{C_{Fe,met} - C_{Fe,sp}} X_{mag}. \quad (7.3)$$

Heedlessly substituting the iron weight percentages of D9, obtained via WDS ( $C_{Fe,met} \approx 70\%$ ,  $C_{Fe,sp} \approx 40\%$ ,  $C_{Fe,mag} \approx 70\%$ ) into equation 7.3, gives  $X_{sp} \approx 2.3X_{mag}$ . This ratio ( $X_{sp}/X_{mag}$ ) is a bit high (see Table 5). The reason for this has to do with the nickel content of D9. D9 is approximately a ternary alloy of iron, chromium, and nickel. A balance equation for nickel would be the same as that for chromium (equation 7.2), with the exception that nickel does not retain its bulk metal concentration. As seen in the WDS linescans, nickel is enhanced 5-10 % over its bulk weight percent. This enhancement in the inner oxide means that the “available space” for Fe/Cr oxide growth will be reduced. Including the nickel enhancement,  $\Delta C_{Ni,sp}$ , in the iron balance equation (eqn. 7.1)

$$C_{Fe,met}X_{met} = C_{Fe,sp}X_{sp} + C_{Fe,mag}X_{mag} - \Delta C_{Ni,sp}X_{sp}.$$

Solving for  $X_{sp}$  gives

$$X_{sp} = \frac{C_{Fe,mag}}{C_{Fe,met} - C_{Fe,sp} + \Delta C_{Ni,sp}} X_{mag}. \quad (7.4)$$

Including  $\Delta C_{Ni,sp}$  brings the ratio,  $X_{sp}/X_{mag}$ , down to the 1.8 – 2.0 range, which agrees much better with the data for the 1000 h and 3000 h exposure times. The ratio of the measured oxide layer thicknesses for the 2000 h exposure is 1:1, which the model doesn’t agree with very well. However, there are reasons for concern with the 2000 h samples (discussed in Chapter 3). Table 5 summarizes these calculations.

The key issue to consider when applying this model to predict oxide thickness ratios is the mobilities of the alloying metals. If a metal exhibits mobilization such that there are variations in weight percentages between the various layers (like iron and nickel in D9), then that needs to be factored into the balance equations. Chromium

does not vary across the layers (except that it is not present in the outer layer) and therefore can be left out of the balance equation for iron.

D9 sample	$X_{sp}$ ( $\mu\text{m}$ )	$X_{mag}$ ( $\mu\text{m}$ )	$X_{sp}/X_{mag}$
1000 h	10.6	6.1	1.7
2000 h	13.0	13.0	1
3000 h	20.0	9.7	2.1
A.S. Model in reference [68]			2.3
Modified A.S. Model			1.8 – 2.0

Table 5 Calculations based on the Available Space Model and measured values of oxide thicknesses on D9. The modified Available Space Model agrees well with the measured oxide ratios for the 1000 h and 3000 h samples.

## CHAPTER 8

### X-RAY PHOTOELECTRON SPECTROSCOPY RESULTS

#### Introduction

As a complementary technique to SEM, XPS is a very valuable technique because it augments the information from SEM. With the ability to track oxidation states as a function of depth, much more has been learned about the nature of corrosion on our samples. By comparing high resolution peaks of individual elements to documented peaks of known oxidation states and species, most of the elements present have been identified. XPS studies of annealed and cold-rolled 316L stainless steels also reveal more interesting details on the differences between exposed and unexposed samples. Many results of preliminary surface surveys and short-duration sputtering performed on these samples have been reported. [70]

It is noteworthy to mention XPS spectra calibration. Typically, XPS spectra will shift because of the problem of charging, especially on insulating samples. When a poorly conducting sample acquires a steady state charge, binding energies in the sample can shift by as much as several electron volts from their true value. Therefore, to insure accuracy in binding energies, all of the XPS spectra need to be calibrated using an internal standard, or reference peak, of known binding energy. For the following data, adventitious carbon was used as the reference, assigned a binding energy of 284.6 eV.

#### Abundances as a Function of Depth

While depth profiles showing atomic percentages as a function of depth are useful, they are at best semi-quantitative. Moreover, the quality of the data gets worse at

greater depths because of prolonged sputtering damage. For good quantitative data on the elements as a function of depth, the WDS linescans presented previously are to be referenced. Also, only quantitative linescans of the D9 samples were taken.

Nevertheless, Sputter Depth Profiling (SDP) is useful, especially for the case of a thin ( $< 1 \mu\text{m}$ ) oxide, as on the 316L cold-rolled samples. On such samples, WDS data are spurious because of spacial resolution limits, which were discussed in Chapter 4.

As mentioned earlier, oxidation states can be tracked using XPS. A binding energy difference of just a few electron volts can constitute a difference in oxidation state. In acquiring this data caution must be exercised to guarantee that any charging that takes place is adequately neutralized by the electron flood gun and/or is properly corrected in the spectra. Any unaccounted for charging can cause peak shifts on the order of several electron volts as well, thereby providing spurious shifts from the true binding energy.

Sputter depth profiles were performed on 316L annealed and cold-rolled samples, exposed to LBE for 3000 h at 550 °C. The SDP data acquired provided both relative abundance (semi-quantitative) of iron, chromium, and oxygen, as well as oxidation state information of iron, chromium, and nickel.

Peak fits of chromium and iron  $2p_{3/2}$  profiles were based on a fit to a pure oxide peak from an oxide standard, and a pure metallic peak (nickel profiles did not show a change that would be indicative of an oxidized state, and is therefore assumed to be metallic at all depths.) All of the parameters in the peak-fitting software (% gaussian, % asymmetry, peak center, peak area), DPViewer from Service Physics, were floated to fit both standards separately. Then the fit parameters for each peak were locked, with the exception of peak center, and both were used to fit the peak profiles throughout the SDP. The peak centers tend to shift a little bit, on the order of 0.5 eV, likely because of charging. However, the separation between the oxide and metallic

peak for a given sputter cycle should be constant. Therefore, the oxide/metallic peak separation is constrained by amounts determined from averaging the peak centers for the oxide and metallic peaks (2.4 eV for chromium, 2.5 eV for iron). Figure 29 shows the fits for oxidized and metallic chromium standards, as well as a fit to a mixed-state chromium envelope taken from an oxidized sample. From the information gained from fitting, the SDP peaks can be graphed to show a percent oxide vs percent metal depth profile graph, based on the areas of the standard peaks, according to the relationship

$$A_{total} = \alpha A_{metal} + (\alpha - 1) A_{oxide},$$

where  $A_{total}$ ,  $A_{metal}$  and  $A_{oxide}$  are the total area of a data profile, and the areas of from the peak fits of the standards; and  $\alpha$  is the amplitude of the metallic peak. The total area is normalized to 100 % in the graphs of Figures 30 and 32.

Apparent in metallic peaks is asymmetric line shapes, having a more gradual slope to higher binding energy. It is well known that a core-level photo-emission lines of metals exhibit a phenomenon known as infrared divergence of electron-hole pair excitations, which leads to asymmetric peaks.[73] In metals, core electrons ejected due to inelastic scattering processes can be easily boosted into the conduction band, above the Fermi level, and contribute to the photo-emission peak on the higher binding energy (lower kinetic energy) side. This line shape is commonly modeled by the *Doniach-Sunjić* (DS) profile. Simply put, it is a gaussian-lorentzian (Voigt) convolution function with an exponential tail modifier function. [73][74][75]

One caveat of this analysis is that depth resolution is not very good. Unlike SEM/EDS/WDS data, a clear switch from oxide state to metallic state is not observed. This is due primarily to inhomogeneous sputter rates of the elements and surface roughness. However, bearing poor depth resolution, the results are consistent with the data from SEM/EDS/WDS.

Another caveat is the aforementioned problem of partial oxide reduction of one

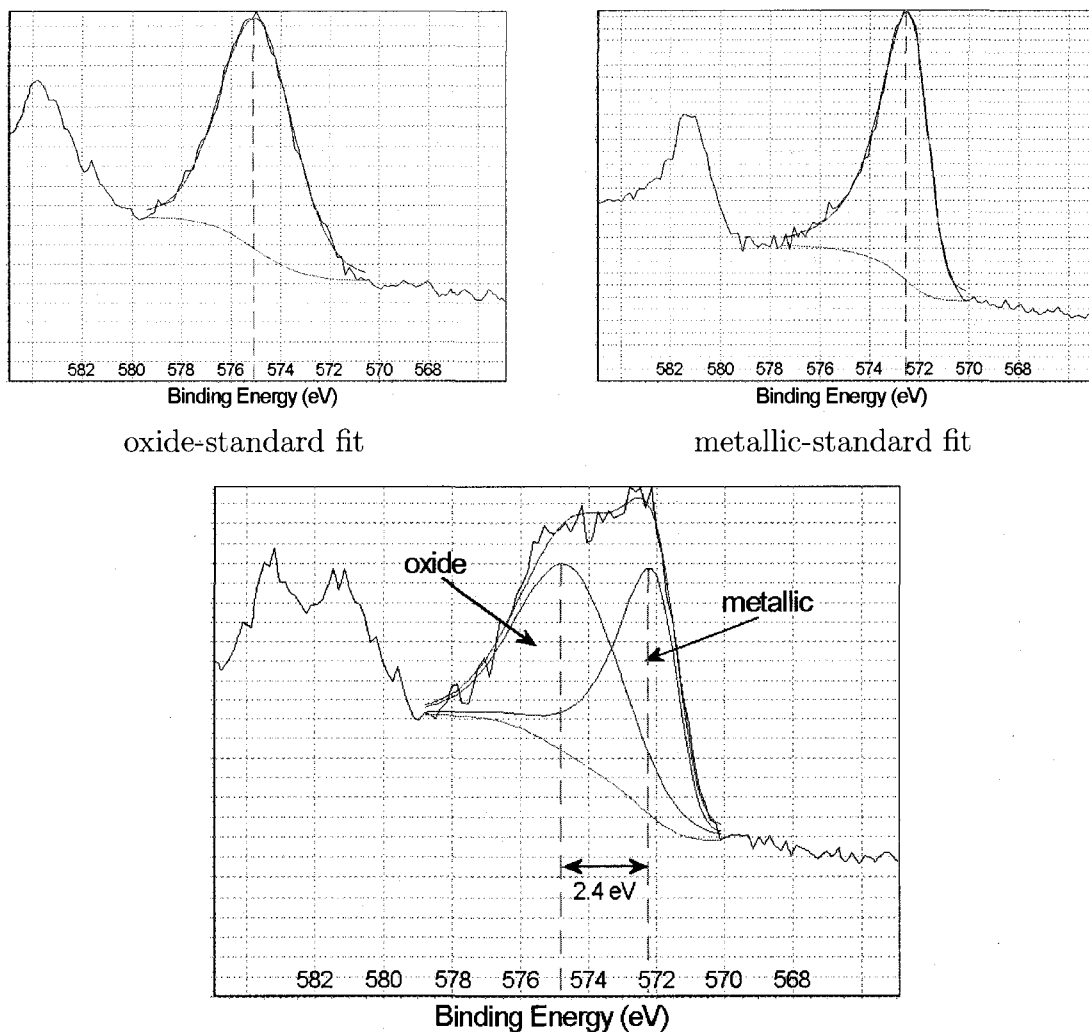


Figure 29 Fits to Cr  $2p_{3/2}$  oxide and metallic standards (top), which are used to fit a Cr  $2p_{3/2}$  peak (bottom) from a corroded sample and annealed 316L. The average separation between the oxide and metallic peak is about 2.4 eV.

metal oxide in intimate contact with the metallic phase of another metal caused by prolonged sputtering. It is known from the SEM/EDS/WDS data that at least three metals are present in the oxide layer regions - iron, chromium, and nickel. Nevertheless, it is regarded as an ignorable effect in this report, insofar as only qualitative information is sought with the XPS/SDP data.



### 316L Annealed, 3000 h

Chromium is virtually oxidized for the first 20  $\mu\text{m}$  at which point metallic chromium starts to appear. For the next 10  $\mu\text{m}$  (to a depth of 30  $\mu\text{m}$ ) the metallic phase strengthens and the oxide weakens until there are equal parts of each. This depth is the observed oxide/metal interface from SEM data. Though chromium is present in the outer layer region, its concentration is very low, as seen in SEM data of Chapter 7. The oxidized and metallic phases of iron appear to be present throughout the oxide layers, however, the oxide phase is predominant in the first 10  $\mu\text{m}$ , consistent with an outer layer of iron oxide. There appear to be roughly equal amounts of metallic and oxidized iron in the inner oxide layer region, with the metallic strengthening and the oxide weakening with depth. At  $> 30 \mu\text{m}$ , only the metallic phase is present. These results are summarized in Figure 30.

Other ways to show how iron and chromium change chemical state with depth include stacking the profiles in order of depth, and graphing each cycle as a color intensity profile with depth. Figure 31 has both such graphs. The trends discussed above are shown: iron is oxidized in the outer oxide layer (8-10  $\mu\text{m}$ ), it consists of both metallic and oxidized states in the inner oxide region (10-30  $\mu\text{m}$ ), and is metallic in the bulk ( $> 30 \mu\text{m}$ ). Chromium is completely oxidized in the inner oxide region, and is metallic in the bulk steel.

### 316L Cold-rolled, 3000 h

Chromium is predominantly oxidized in the first 500 nm of the SDP, at which depth the metallic begins to slowly appear. At a depth of 1  $\mu\text{m}$  and beyond, both oxide and metallic phases are present in equal amounts. Iron is completely oxidized at the surface, but the metallic phase quickly appears and equals the oxide phase at a depth of about 300 nm. Beyond that depth, the metallic phase grows to 70-80 % to all depths shown, and presumably continues in that trend until only metallic iron

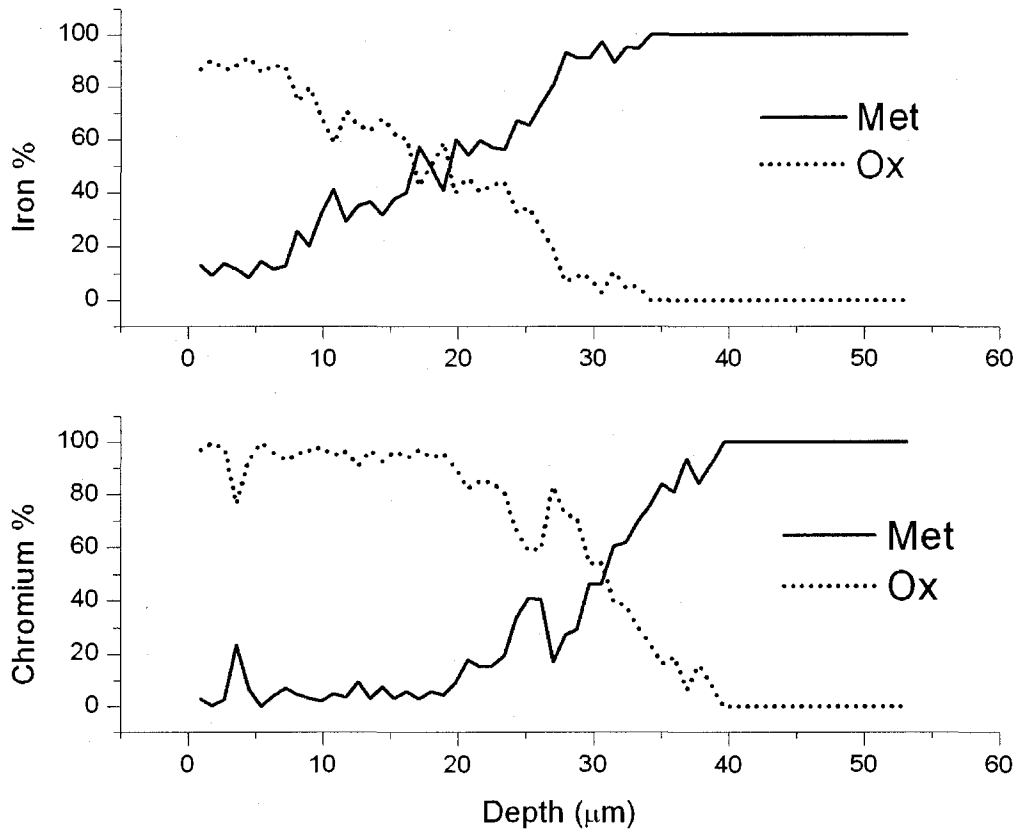


Figure 30 XPS SDP of oxide ("Ox") vs. metallic ("Met") percentages of iron (top) and chromium (bottom) on annealed 316L, exposed to LBE for 3000 h at 550 °C.

is present. These results are summarized in Figure 32.

Figure 33 consists of stacked line graphs and color intensity profiles of iron and chromium as a function of depth. The aforementioned conclusions are confirmed: iron is metallic at the surface and quickly develops a metallic edge. At a depth of 1 μm it is completely metallic. Chromium is oxidized at all depths, although it gradually broadens to lower binding energy, indicative of metallic chromium.

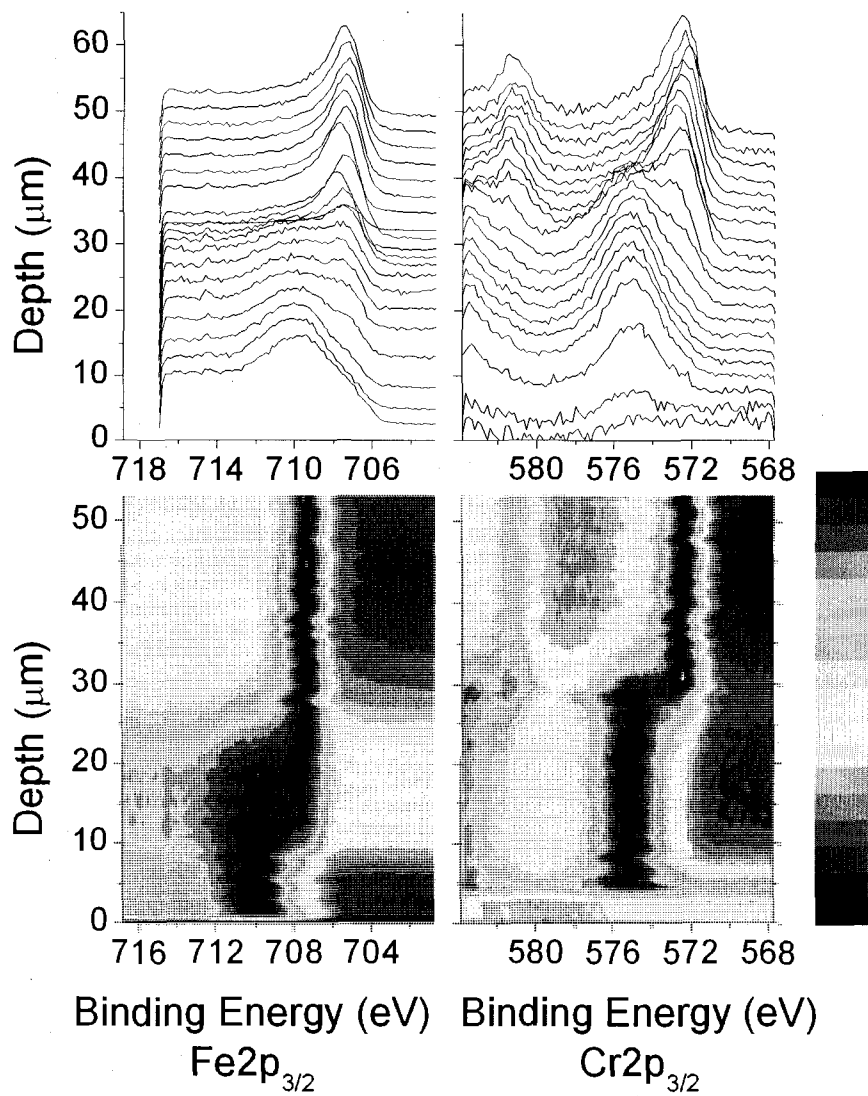


Figure 31 XPS SDP line (top) and color (bottom) intensity profiles of iron and  $2p_{3/2}$  peaks on annealed 316L, exposed to LBE for 3000 h at 550 °C. Blue is the most intense in the color intensity profile.

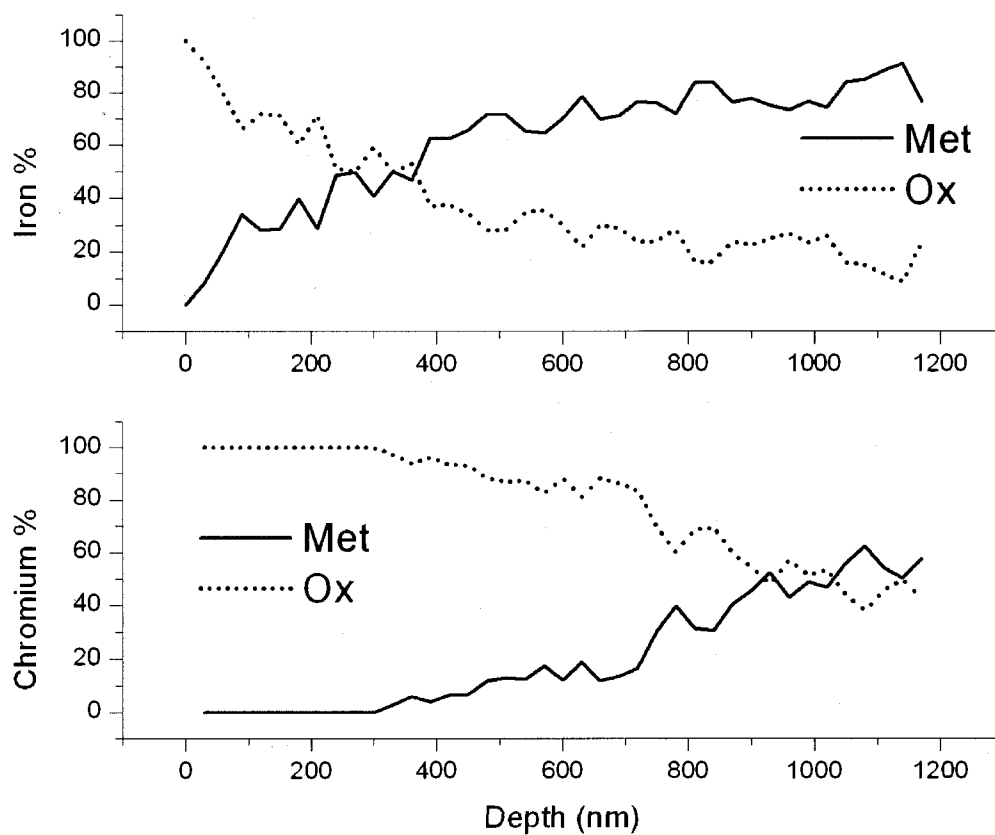


Figure 32 XPS SDP of oxide ("Ox") vs. metallic ("Met") percentages of iron (top) and chromium (bottom) on cold-rolled 316L, exposed to LBE for 3000 h at 550 °C.

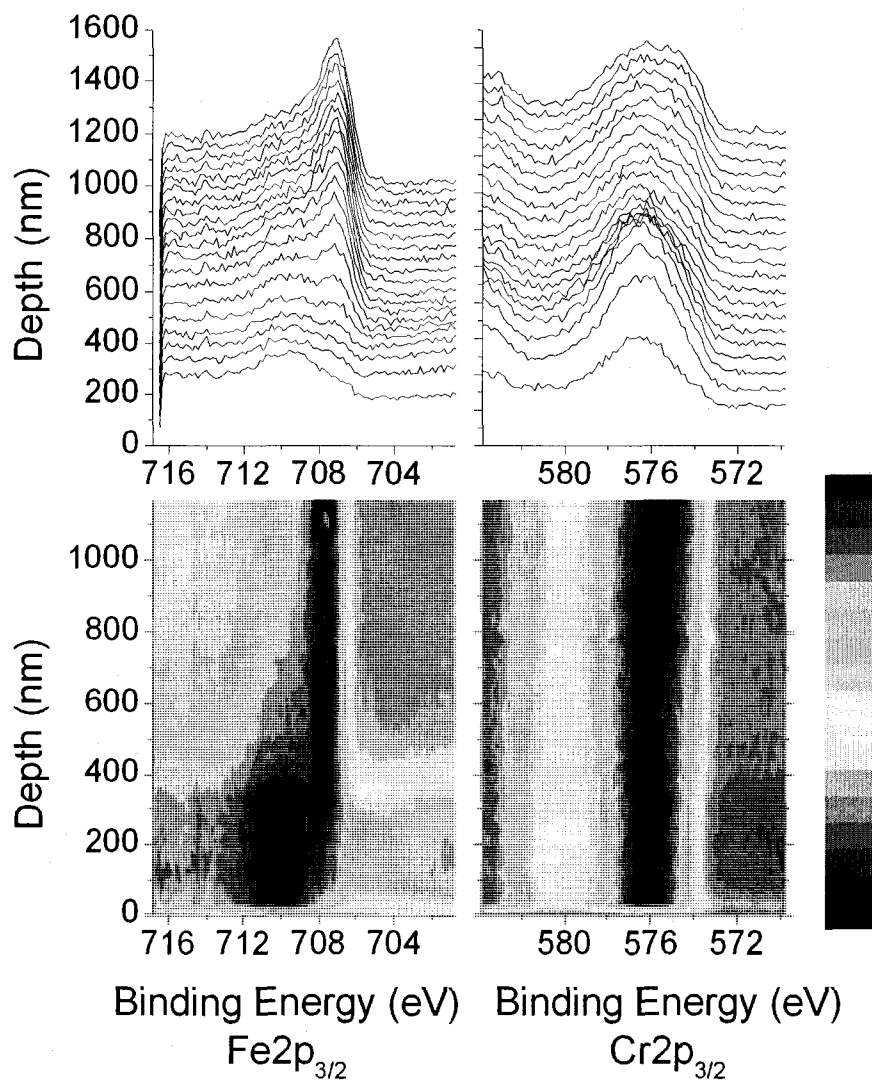


Figure 33 XPS SDP line (top) and color (bottom) intensity profiles of iron and  $2p_{3/2}$  peaks on cold-rolled 316L, exposed to LBE for 3000 h at 550 °C. Blue is the most intense in the color intensity profile.

## CHAPTER 9

### COLLABORATION

In a collaborative effort to further understand the corrosion mechanism(s) on D9, Atomic Force Microscopy (AFM), Magnetic Force Microscopy (MFM), and Nanoindentation to measure hardness were performed by *Peter Hosemann* [76] at Los Alamos National Lab (LANL). From his AFM and MFM images (Figure 34) he finds four different layers within the already-identified duplex layers.

The outer two layers constitutes the outer, iron-oxide layer of the duplex. The outermost is a sub-micron grained layer with no preferential grain orientation, but strong magnetic polarization. The second layer (outside  $\rightarrow$  in) is a larger grained (micron sized) layer in which the grains are elongated normal to the surface, and it possesses the strongest magnetic polarization. These grains, still much smaller than those in the bulk (20-30  $\mu\text{m}$ ), have columnar appearances (note red box in Figure 34a). These features are believed to be evidence of diffusion pathways for outward diffusing iron (see Chapter 10). The third layer is only observed in the MFM images as it has no magnetic polarization and is very thin ( $\leq 1 \mu\text{m}$ ). This is possibly the initial thin oxide on the unexposed steel. Some WDS linescans show a slight chromium enhancement in this same region, which supports this proposition. The last inner layer is the thickest and is whole inner oxide of the duplex structure. It shows the same grain structure as the bulk steel, with the grain boundaries being weak, porous, and abundant with precipitates. The precipitates are probably chromium oxides, as SEM data shows (Figure 21). MFM shows that its magnetic structure is relatively weak.

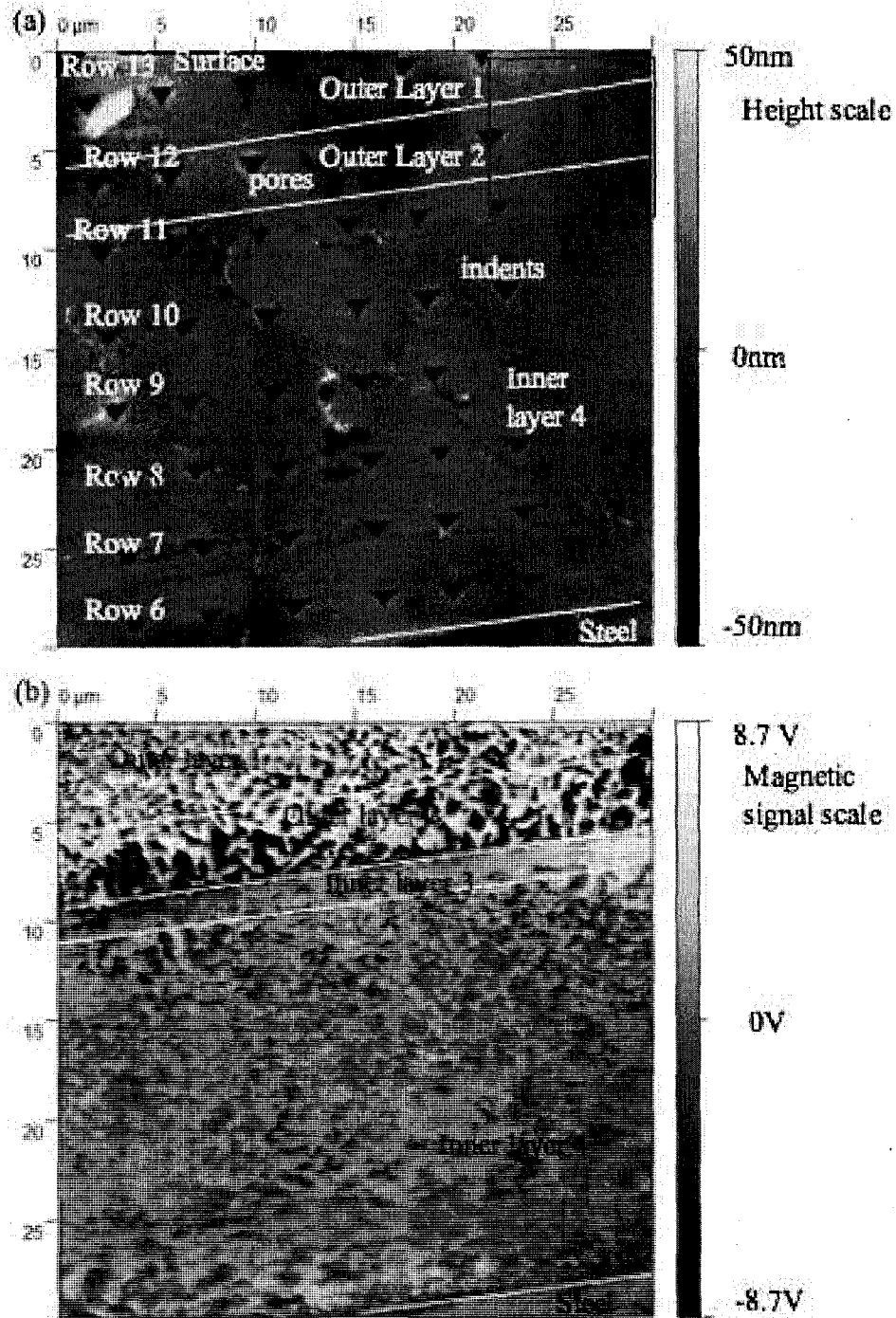


Figure 34 Four sublayers of the duplex oxide with the outermost layer at the top. (a) AFM image of oxide layers on exposed D9. Note the nanoindentation marks and grain boundaries. (b) MFM image of oxide layers on exposed D9.

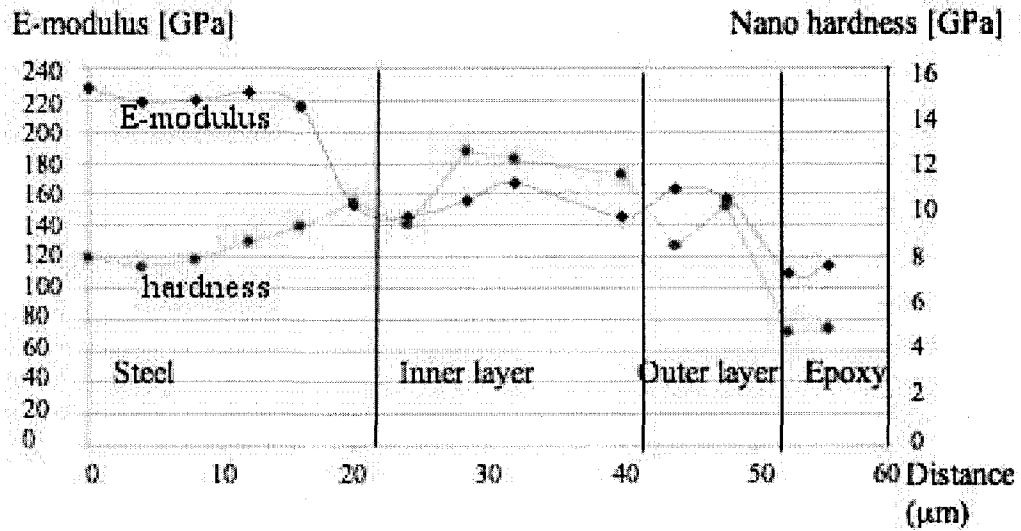


Figure 35 Hardness and E-modulus nanoindentation measurements on oxide layers of D9, exposed to LBE for 3000 hr at 550 C.

Hardness and elastic (Young's) modulus (or E-modulus) were determined from nano indentation measurements. Measuring from the steel outward (Figure 35) through the oxide layers, the Young's modulus was found to be highest in the bulk steel, where it is around 200-220 GPa. In the inner oxide it is at its lowest, varying 140-160 GPa, and in the outer oxide layer(s) it is slightly higher, around 160 GPa. As for hardness measurements, the inner oxide is the hardest ( $\approx 180$  GPa), followed by the outer oxide ( $\approx 120$ -140 GPa), and lastly the bulk steel ( $\approx 120$  GPa).



## CHAPTER 10

### CONCLUSION

From our surface SEM/EDX studies we know that exposed samples are covered with oxides, as indicated by strong oxygen peaks. Unexposed samples do not have significant oxygen peaks. Furthermore, among the exposed samples we know some areas are covered more densely with oxides. On such samples, uncovered or lightly covered areas show chromium signatures similar to that of an unexposed sample, whereas covered areas show little if any chromium. Iron and oxygen are strong in both the covered and uncovered areas, suggesting different oxide layer thicknesses (very thin oxide layering in the uncovered areas).

From the cross-sectional analysis we gain much insight to the processes at work. Together with the surface work, it can be concluded that oxidation corrosion begins locally at grain boundaries or surface defects that breach the initial passivating oxide (preoxidation is beneficial to the preservation of the steel.) Inward oxidation occurs first along grain boundaries and other fast-diffusion paths. Grains gradually become completely oxidized but maintain their original shape. Because of the grain structure preservation, oxygen diffuses inward and the inner oxide grows in vacancies left by outward diffusing elements, namely, iron. The outer oxide is amorphous magnetite, formed from outward diffusing iron as it comes into contact with free oxygen in the LBE. The outer oxide, which grows above the original steel interface, is easily eroded away. It is the outer iron-based oxide that gives the surfaces a patchy, blistered look.

From our XPS studies we see quite different data. Because of the surface sensitivity of XPS (first few atomic layers), we initially see very similar peaks on both exposed

and unexposed samples. In the spectra, carbon and oxygen both show up quite strongly. At first glance this seems very surprising since EDX does not show much for the existence of carbon, and oxygen only showed up on the exposed samples. While keeping in mind that XPS and EDX probe significantly different depth regions, this is what initially led us to suspect the existence of surface contaminants. After ion-beam milling, the XPS spectra changed drastically.

Iron shows up mostly in metallic form on the unexposed samples and mostly oxidized on the exposed samples, as expected. Also, oxidized iron remains constant throughout sputtering (up to 85 sec) on the exposed samples. Metallic iron appears with increasing depth on the exposed samples. Chromium is similar to iron, but is much weaker in oxidized form on the exposed annealed 316L. However, on the exposed cold-rolled 316L sample oxidized chromium is much stronger. We expect to see  $\text{Cr}_2\text{O}_3$  on stainless steels (especially on the unexposed samples), as it is the passivating component under atmospheric conditions. It appears in oxidized form on the surface of the unexposed samples and changes to metallic form with sputtering. We also expect, as mentioned in Chapter 6, to see weak signals from nickel on the exposed samples because nickel has the highest solubility in liquid metals. We do indeed see weak nickel peaks on the exposed samples, while on the unexposed samples nickel appears in metallic form. Finally, residual lead and bismuth appear on the exposed samples but not on the unexposed samples. On the exposed samples, lead and bismuth appear in both oxidized ( $\text{PbO}$  and  $\text{Bi}_2\text{O}_3$ ) and metallic form. They are both more oxidized on the surface and change to metallic form with sputtering.

An explanation of duplex oxide growth from oxidation/corrosion observed on the samples, in accordance with theoretical models, is the following: when fresh steel is first exposed to oxygen-controlled LBE at high temperature, a surface potential is created by oxygen ions which draws Fe ions out of the bulk. Although some

diffusion takes place within the steel grains, most of the diffusion takes place in grain boundaries, which serve as fast-diffusion paths. Iron is the primary diffusant because it has the second highest diffusion coefficient (*Lobnig et al.* report  $D_{Mn} > D_{Fe} > D_{Ni} > D_{Cr}$  [77]) and iron is the most abundant. Chromium is also somewhat mobile, but being the least noble of the alloying elements it quickly forms chromium-based oxides with oxygen anions, which diffuse in via grain boundaries. These oxides, which are enhanced in grain boundaries, are evident in Figure 21.

Oxidation within the grains also occurs because of voids left by vacated Fe locations and the grains retain their original structure. These oxides tend to be iron and possibly nickel chromite, a spinel structured oxide of the chemical form  $(Fe,Ni)Cr_2O_4$ . This is supported by preliminary x-ray diffraction data taken on D9 at Argonne National Lab (ANL) and Raman data taken at UNLV. [58] Nickel also moves and is enhanced in the inner oxide with respect to the bulk, though it is depleted in the inner oxide grain boundaries. It is believed that Ni undergoes similar diffusion that of chromium and iron, and ends up forming a nickel chromite, filling inner oxide voids in metallic form, or it dissolves into the LBE in metallic form, as it is by far the most soluble in LBE (Figure 13). In the bulk steel grain boundaries, close to the inner oxide, nickel appears to be slightly enhanced.

On annealed 316L, XPS data shows that molybdenum is oxidized to 20 um, but it was not mapped with EDX because of peak overlap with lead. Manganese cannot be mapped because of overlap with chromium, and there are no XPS data for manganese on annealed 316L. However, on the D9 sample, manganese was plotted in a WDS linescan and is measured to a weight percent of 3 - 3.5 (Figure 26), which is up from its bulk value of about 2 %. This is a compelling indication that manganese could play a role in the formation of the inner spinel oxide. [15][78][79] However, at 3.5 % it is not sufficiently abundant to be the only other participant other than chromium.

As a result of the mobilities of iron, chromium, and oxygen, a duplex oxide structure is formed. In the literature, oxygen has a very low diffusion tendency, but evidence shows that it clearly diffuses well into the steel ( $> 10 \mu\text{m}$ ). A plausible explanation of this is that oxygen diffuses through cracks and pores, and typical grain boundary pathways. [71] Oxygen diffusion is enhanced with increasing temperature. [80]

Above the original steel interface is an oxide of amorphous, small-grained  $\text{Fe}_3\text{O}_4$  and below the original interface is a spinel-type oxide, which propagates fastest along grain boundaries and gradually engulfs the grains. These oxide layers can grow to tens of microns in thickness. Gradually, however, their growths slow until they eventually stop.

It is observed from AFM data (Figure 34) that the outer oxide layer is not composed of homogenous grains of magnetite. Rather, it is larger-grained just outside the original interface (though the grains are still quite small compared that of the original steel) and the grains get smaller the farther from the interface they get. This trend of smaller grain size in proportion to distance from the original bulk steel interface is possibly due to a decline in iron diffusion (corrosion current,  $J$ , is proportional to the electric field across the oxide, which is inversely proportional to the oxide thickness,  $\delta$ , therefore  $J \propto 1/\delta$  [63]). As the oxide becomes thicker, the amount of iron arriving at the surface decreases and grain nucleation favors smaller, more-easily formed grains. This, in turn, leads to amorphous conglomerates. Moreover, the outermost region of the oxide layer is exposed to turbulent forces from flowing LBE, and is therefore susceptible to erosion corrosion. This, too, could possibly restrict grain growth at the oxide/LBE interface.

The growth of the inward growing, mixed spinel-phase oxide is also observed in samples exposed for 3000 hr. It is observed that the oxidation front in some regions

is rather straight (Figure 22), regardless of location (grain boundaries or grains), as opposed to those regions where the oxide is clearly deepest along grain boundaries. To account for this observation, a similar mechanism to the halting growth of the outer oxide is thought to be in effect, in which diffusion of oxygen inward has died off and only diffusion in the lateral direction occurs.

At the oxide/LBE front, the iron oxide is also slowly dissolved by the LBE (disregarding erosion corrosion). As long as this rate is slow enough, however, the oxide can be deemed protective and passivating. The ultimate fate of the steel is net material loss. Similar to oxidation in gaseous environments, stainless steels experience weight gain of parabolic growth in the initial phases of exposure, in accordance with Wagner's Theory. In LBE, however, the growth is constantly in competition with material loss due to dissolution, erosion, and spalling due to tangential stresses from phase mismatching at the interface [81] as the outer oxide thickens. However, AFM and nanoindentation data refute high stresses in the oxide layers. [76] Initially the oxide growth and weight gain dominates, enough so that a parabolic trend is observed. In the long term (time > thousands of hours) the oxide reaches a maximum thickness and material loss dominates. This trend is modeled well by Tedmon's modification to Wagner's Law.

This one-dimensional model does well to explain many of the observed phenomena. Unfortunately, it assumes that oxide growth is uniform across the surface of a sample and Figures 18 and 19 clearly show that the outer oxide is patchy, though total sample coverage seems to be the consequential trend. It is seen that some regions do not have the thick iron oxide coverage and presumably have a chromium rich thin oxide, likely the original protective ("stainless") oxide. Although some cross-sectional images show the inner chromite oxide lacking the outer magnetite oxide, those regions are rare. Presumably those regions have lost their outer layer from erosion or spallation. It

is more commonly observed that a thin iron/chromium oxide exists in regions not having an outer iron oxide layer. This is confirmed by EDX measurements (Figure 18a and 19a). It is not known if this kind of thin oxide is protective because evidence is ambiguous. *Zhang and Li et. al.* suggest that such an oxide is not “protective”. [64]

Regardless of the protective nature of the thin oxide, the mere existence of “uncovered” regions suggests some modifications to the one-dimensional model. A suggestive appendence to the model would be to say the thick, duplex oxide initially originates from a defect on the surface. This defect could be a break in the oxide due to any number of effects, but the simplest possibilities would be erosion or a mechanical breach in the original oxide (e.g., scratch). Another access point for material passage could be the intersection of multiple grain boundaries on the surface. It is known that stainless steels form a thin, dense, well-adhesive chromia ( $\text{Cr}_2\text{O}_3$ ) layer that is protective and generally self-healing in most environments. Discontinuities occurring at grain boundaries could be the weak points where breaches could occur in aggressive chemical environments. Once a break in the initial oxide is present, diffusion of the elements outlined above commences. As iron reaches the surface it is oxidized and forms small grains on the surface. Eventually these “volcanoes” grow laterally together, forming a continuous cover. Baer [82] describes a scenario of non-uniform oxide growth on a surface. Depending temperature and oxygen potential, the oxide can be chromium-rich at grain boundaries and iron-rich above the grains. Generally this occurs at higher oxygen potentials, and if the potential is low enough the only stable oxide that forms is chromia.

It is widely accepted that grain boundaries play a major role in the formation of a self-healing, protective oxide. [12][14][15][16][17][18] Previously we speculated that grain boundaries on the surface of steel could be the gateways to metallic cation and

oxygen anion passage, leading to the duplex oxide structure. It has been proposed that grain boundaries are the a very important parameter in the self-healing process on a stainless steel. *Peng* [83] proposes that cold-worked stainless steels are more efficient self-healers based on the fact that there are more grain boundaries and other fast diffusion pathways on the surface and in the near surface. Cold-working steels tends to deform grains, introducing stresses into them. As the grains relax, atoms move into domains of lower internal energy and new, smaller grains are formed. Since grain boundaries are fast paths for diffusion, having more of them allows a greater abundance of metal cations to diffuse to the surface. All metal atoms present in the steel can diffuse to the surface, but the least noble of them react to form oxides first. If the candidate steel is an alloy containing at least 11% chromium then the steel can continue to form a thin ( $\leq 1 \mu\text{m}$ ), stable  $\text{Cr}_2\text{O}_3$  layer. This phenomenon is well studied and verified in gaseous ( $\text{O}_2$  present) and aqueous environments. In a liquid metal, such as LBE, the dynamics are more complex and this process may only occur pending favorable thermodynamic and kinetic conditions. *Merz* [84] (as cited in [82]) describes a different nature of duplex oxide formation. In his experiments he found thin, chromium-rich oxides form on grain boundaries and thicker, iron-rich oxides form over grains for larger grained ( $\sim 40 \mu\text{m}$ ) 304 stainless steel. On smaller grained ( $\sim 4 \mu\text{m}$ ) 304 stainless steel he reports a uniform chromium-rich oxide. With the appropriate surface treatment, the larger grained steel could form a protective chromium oxide.

From the evidence presented in this study, thin chromium-rich oxide on the the cold-rolled 316L is more suited to prolonging the lifetime of LBE-containing steel. The appearance of localized duplex oxide growth (Figure 24) is indicative of a process that ultimately takes place when the denser, thin oxide is breached. The duplex oxide takes longer to develop in the presence of an initial chromium-rich oxide. Moreover,

since the duplex oxide is sustaining as well, the longevity of the steel is greater in the case where the rate of duplex oxide development is significantly reduced.



## APPENDIX I

### METALLURGICAL DEFINITIONS

**anneal** - Stress-relieving process in which a material is heated and held at a desired temperature to allow components to relax into lower energy phases. Reduces hardness, improves machinability.

**austenite** - Face-centered cubic (fcc) iron alloy ( $\gamma$ -phase iron).

**carbon steel** - Steels containing less than 2% total alloying elements. They are the most utilized (90% of all steels shipped in U.S.) Carbon content and microstructure are the principle factors affecting their properties. [85]

**carburize** - Introduction of carbon into a ferrous alloy at a high enough temperature to allow carbon diffusion into the metal. Oldest method of hardening (also called *cementation*).

**cementite** - Metastable iron carbide, approximately  $\text{Fe}_3\text{C}$

**cold-working** - Plastic deformation of a metal produced by an external force at a temperature below its recrystallization temperature. Induced strains (defects) to microstructure have hardening effects (also called *work-hardening*).

**ferrite** - Body-centered cubic (bcc) iron alloy ( $\alpha$ -phase iron)

**martensite** - Metastable transitional phase between the austenitic (fcc) and ferritic (bcc), having a body-centered-tetragonal (bct) crystal structure in steels. It is the strongest phase, with needle-like granular structure which occurs by quenching heated steels in an austenitic phase.

**pearlite** - Aggregate of ferrite and cementite.

**pickling** - The process of chemically removing surface oxides and scales from the

surface of metals by the action of chemical, from inorganic acids, or electrochemical reactions.

**quench** - Immersion of a metal in oil or water to achieve rapid cooling as part of the heat treatment process in order to produce a desired effect (typically hardening).

**sensitization** - intergranular corrosion due to chromium carbides forming in grain boundaries, diminishing chromium at grain edges and impairing corrosion resistance.

**temper** - To reheat a hardened metal to a temperature below the transformation range and then cool at any rate for the purpose of increasing ductility and resilience, at the expense of loss of hardness.

**transformation range** - Temperature range over which metallurgical or chemical transformations occur for a given metal.

## REFERENCES

- [1] Peter Atkins. *Physical Chemistry*. W.H. Freeman & Company 5<sup>th</sup> edition 1994.
- [2] H. Glasbrenner, F. Gröschel, H. Grimmer, J. Patorski and M. Rhode. *Expansion of solidified lead bismuth eutectic*. Journal of Nuclear Materials **343**, 341–348 (August 2005).
- [3] J. A. Taylor and D. L. Perry. *An x-ray photoelectron and electron energy loss study of the oxidation of lead*. Journal of Vacuum Science & Technology A: Vacuum, Surfaces, and Films **2** (2), 771–774 (1984).
- [4] X. He and N. Li. *Review of Russian's reports on 'Results of corrosion tests on 316, 316L, T-410, HT-9, and D-9 steels'*. Technical report 2000.
- [5] J. Moore, S. Greer, C. Davis and M. Coplan. *Building Scientific Apparatus*. Westview Press 2002.
- [6] J. Beddoes and J. Gordan Parr. *Introduction to Stainless Steels*. ASM International 1999.
- [7] Lauren Benny Susanto. *Kinetics of Carbide Dissolution in Chromium + Molybdenum Steels During Oxidation*. PhD thesis School of Material Science and Engineering, University of New South Wales, Australia Feb. 2004.
- [8] J. R. Davis, Editor. *ASM Specialty Handbook: Stainless Steels*. ASM International 1994.
- [9] T. Baumeister, E. Avallone and T. Baumeister III. *Mark's Standard Handbook for Mechanical Engineers*. McGraw-Hill Professional 1978.
- [10] H. S. Khatak. *Corrosion of Austenitic Stainless Steel: Mechanisms, Mitigations & Monitoring*. Alpha Science International Ltd. 2001.
- [11] C. Fazio, G. Benamati, Martini and G. Palombarini. *Compatibility tests on steels in molten lead and lead-bismuth*. Journal of Nuclear Materials **296**, 243–248 (2001).
- [12] Ning Li, Jinsuo Zhang, Bulent Sencer and Daniel Koury. *Surface treatment and history-dependent corrosion in lead alloys*. Nuclear Instruments & Methods in Physics Research A **562**, 695–697 (2006).
- [13] Mike Meier. *The Hall-Petch Relationship*. Technical report Department of Chemical Engineering and Materials Science, University of California, Davis 2004.

- [14] J. Beddoes and K. Bucci. *The influence of surface condition on the localized corrosion of 316L stainless steel orthopaedic implants*. Journal of Materials Science: Materials in Medicine **10**, 389–394 (1999).
- [15] J. W. Tyler. *Characterization of the Initial Oxide formed on Annealed and Unannealed 20Cr-25Ni-Nb-Stabilized Steel in 50 torr CO<sub>2</sub> at 973 K*. Oxidation of Metals **24** (3/4), 149–176 (1985).
- [16] M. Warzee, J. Hennaut, M. Maurice, C. Sonnen, J. Waty and Ph. Berge. *Effect of Surface Treatment on the Corrosion of Stainless Steels in High-Temperature Water and Steam*. Journal of The Electrochemical Society **112** (7), 670–674 (July 1965).
- [17] R. C. Lobb and H. E. Evans. *Formation of Protective Oxide Film on Chromium-Depleted Stainless Steel*. Metal Science **15** (6), 267–274 (June 1981).
- [18] S. N. Basu and G. J. Yurek. *Effect of Alloy Grain Size and Silicon Content on the Oxidation of Austenitic Fe-Cr-Ni-Mn-Si Alloys in Pure O<sub>2</sub>*. Oxidation of Metals **36** (3/4) (1991).
- [19] L. Leibowitz and R. A. Blomquist. *Thermal Conductivity and Thermal Expansion of Stainless Steels D9 and HT9*. International Journal of Thermophysics **9** (5), 873–883 (1988).
- [20] A. Banerjee, S. Raju, R. Divakar, E. Mohandas, G. Panneerselvam and M. P. Antony. *Thermal property characterization of a titanium modified austenitic stainless steel (alloy D9)*. Journal of Nuclear Materials **347**, 20–30 (2005).
- [21] Baldev Raj, S. L. Mannan, P. R. Vasudeva Rao and M. D. Mathew. *Development of fuels and structural materials for fast breeder reactors*. Sādhanā pages 527–558 (2002).
- [22] S. L. Mannan, S. C. Chetal, Baldev Raj and S. B. Bhoje. *Selection of Materials For Prototype Fast Breeder Reactor*. Transactions of the Indian Institute of Metals **56** (2), 155–178 (2003).
- [23] S. Latha, M. D. Mathew, K. Bhanu Sankara Rao and S. L. Mannan. *Creep Deformation Behaviour of Titanium Modified Austenitic Stainless Steel*. International Symposium of Research Students on Materials and Engineering (2004).
- [24] Sumantra Mandal, P. V. Sivaprasad, K. P. N. Murthy and Baldev Raj. *Modeling constitutive behavior of a 15Cr-15Ni-2.2Mo-Ti modified austenitic stainless steel under hot compression using artificial neural network*. Proceedings of the International conference on Statistical Mechanics of Plasticity and Related Instabilities (2006).
- [25] V. Shankar, T. P. S. Gill, A. L. E. Terrance, S. L. Mannan and S. Sundaresan. *Relation between Microstructure, Composition, and Hot Cracking in Ti-Stabilized*

- Austenitic Stainless Steel Weldments*. Metallurgical and materials transactions A, Physical metallurgy and materials science **31** (12), 3109–3122 (2000).
- [26] G. VanderVoort. *Metallography Principles And Practice*. ASM International 1999.
  - [27] J. Wilson and A. Buffa. *College Physics*. Prentice-Hall Engineering/Science/Mathematics 1997.
  - [28] G. Somorjai. *Introduction To Surface Chemistry and Catalysis*. John Wiley and Sons, Inc. 1994.
  - [29] E. M. Pell. *Ion Drift in an n-p Junction*. Journal of Applied Physics **31** (2), 291–302 (1960).
  - [30] J. Goldstein, D. Newbury, D. Joy, C. Lyman, P. Echlin, E. Lifshin, L. Sawyer and J. Michael. *Scanning Electron Microscopy and X-Ray Microanalysis*. Kluwer Academic/Plenum Publishers 3<sup>rd</sup> edition 2003.
  - [31] H. Rahab, A. Keffous, A. Akam and H. Menari. *The Preparation of Lithium Drifted Silicon Si(Li) Detector*. Advanced Performance Materials **6**, 53–56 (1999).
  - [32] K. Kanaya and S. Okayama. *Penetration and energy-loss theory of electrons in solid targets*. Journal of Physics D: Applied Physics **5**, 43–58 (1972).
  - [33] S. J. B. Reed. *Electron Microprobe Analysis and Scanning Electron Microscopy in Geology*. Cambridge University Press 1996.
  - [34] D. L. Perry. *Applications of Analytical Techniques to the Characterization of Materials*. Springer 1991.
  - [35] J. Moulder, W. Stickle, P. Sobol and K. Bomben. *Handbook of X-ray Photoelectron Spectroscopy*. Physical Electronics, Inc. 1995.
  - [36] B. Crasemann. *Atomic Inner Shell Processes*. Academic Press Inc., U.S. 1975.
  - [37] D. Briggs and M. P. Seah. *Practical Surface Analysis by Auger and X-ray Photoelectron Spectroscopy*. John Wiley and Sons, Inc. 1 edition 1983.
  - [38] M. H. Engelhard, D. R. Baer, T. Drouby, A. S. Lea and P. Nachimuthu. *Comparison of the Sputter Rates of Fe<sub>2</sub>O<sub>3</sub>, Cr<sub>2</sub>O<sub>3</sub>, CeO<sub>2</sub>, ZnO, TiO<sub>2</sub>, and Ta<sub>2</sub>O<sub>5</sub> Films to the Sputter Rate of SiO<sub>2</sub>*. American Vacuum Society Symposium Poster Session (To be published) Nov 2006.
  - [39] D. A. Shirley. *High-Resolution X-Ray Photoemission Spectrum of the Valence Bands of Gold*. Phys Rev B **5** (12), 4709–4714 (1972).
  - [40] R. Vanselow and S. Y. Tong. *Chemistry and Physics of Solid Surfaces*. CRC Press Inc 1977.

- [41] J. B. Wachtman. *Characterization of Materials*. Butterworth-Heinemann 1993.
- [42] D. J. O'Connor and B. A. Sexton. *Surface Analysis Methods in Materials Science*. Springer 1992.
- [43] L. L. Shreir, R. A. Jarman and G. T. Burstein. *Corrosion Vol1 Metal/Environment Reactions*. Butterworth-Heinemann 3 edition 1994.
- [44] Alan M. Bolind. *Control of the Oxygen Content of the Cover Gas in a Molten Lead-Bismuth Eutectic System*. Master's thesis University of Illinois at Urbana-Champaign 2006.
- [45] H. J. T. Ellingham. *Reducibility of Oxides and Sulfides in Metallurgical Process*. Journal of The Society of Chemical Industry **63**, 125 (1944).
- [46] David Talbot and James Talbot. *Corrosion Science and Technology*. CRC Press Inc 1<sup>st</sup> edition 1998.
- [47] N. Cabrera and N. F. Mott. *Theory of The Oxidation of Metals*. Reports on Progress in Physics **12**, 163–184 (1949).
- [48] Richard Ghez. *On the Mott-Cabrera oxidation rate equation and the inverse-logarithmic law*. Journal of Chemical Physics **58** (5), 1838–1843 (1973).
- [49] Alexander H. Tullo. *Foiling Corrosion Involves Outsmarting Metals' Nature*. Chemical & Engineering News: Business **85** (38), 20–21 (2007).
- [50] J. C. Scully. *The Fundamentals of Corrosion*. Pergamon 1975.
- [51] David W. Oxtoby and H. Pat Gillis. *Principles of Modern Chemistry*. Brooks Cole 1999.
- [52] Xiaoyi He, Ning Li and Mark Mineev. *A kinetic model for corrosion and precipitation in non-isothermal LBE flow loop*. Journal of Nuclear Materials **297**, 214–219 (2001).
- [53] Ning Li. *Active control of oxygen in molten lead-bismuth eutectic systems to prevent steel corrosion and coolant contamination*. Journal of Nuclear Materials **300**, 73–81 (2002).
- [54] J. Zhang and N. Li. *Review of studies on fundamental issues in LBE corrosion*. Technical report Los Alamos National Laboratory 2004.
- [55] J. Zhang and N. Li. *Oxidation Mechanism of Steels in Liquid-Lead Alloys*. Oxidation of Metals **63** (5/6), 353–381 (2005).
- [56] H. Glasbrenner, J. Konys, G. Müller and A. Rusanov. *Corrosion investigations of steels in flowing lead at 400 C and 550 C*. Journal of Nuclear Materials **296**, 237–242 (2001).

- [57] F. Barbier and A. Rusanov. *Corrosion behavior of steels in flowing lead-bismuth*. Journal of Nuclear Materials **296**, 231–236 (2001).
- [58] B. Hosterman. *Micro-Raman Spectroscopic Study of the Corrosion of Stainless Steel by Lead Bismuth Eutectic*. Master's thesis University of Nevada, Las Vegas 2006.
- [59] J. Zhang, N. Li and Y. Chen. *Dynamics of high-temperature oxidation accompanied by scale removal and implications for technological applications*. Journal of Nuclear Materials **342**, 1–7 (2005).
- [60] H. U. Borgstedt and C. Guminski. *A model for the prediction of the corrosion of steels in flowing liquid lead alloys*. Journal of Nuclear Materials **303**, 240–241 (2002).
- [61] X. He and N. Li. *Lattice Boltzmann simulation of electrochemical systems*. Computer Physics Communications **129**, 158–166 (2000).
- [62] Carl Wagner. *The distribution of cations in metal oxide and metal sulphide solid solutions formed during the oxidation of alloys*. Corrosion Science **9**, 91–109 (1969).
- [63] A. Atkinson. *Transport processes during the growth of oxide films at elevated temperature*. Reviews of Modern Physics **57** (2), 437–470 (1985).
- [64] Jinsuo Zhang, Ning Li, Yitung Chen and A. Rusanov. *Corrosion behaviors of US steels in flowing lead-bismuth eutectic (LBE)*. Journal of Nuclear Materials **336**, 1–10 (2005).
- [65] C. S. Tedmon. *The Effect of Oxide Volatilization on the Oxidation Kinetics of Cr and Fe-Cr Alloys*. Journal of The Electrochemical Society **113**, 766–768 (1966).
- [66] H. Taimatsu. *Kinetic Analysis of High-Temperature Oxidation of Metals Accompanied by Scale Volatilization*. Journal of The Electrochemical Society **146** (10), 3686–3689 (Oct-Dec 1999).
- [67] G. Müller, G. Schumacher, D. Strauß, V. Engelko, A. Andreev and V. Kavalijov. *Modification of material surfaces by the pulsed electron beam facility GESA*. In *Proceedings of the 11<sup>th</sup> International Conference on High-Power Particle Beams* Band 2 page 809. K. Jungwirth June 1996.
- [68] Laure Martinelli, F. Balbaud-Célérier, S. Bosonnet, A. Terlain, G. Santarini, S. Delpech and G. Picard. *High temperature oxidation of Fe-9Cr steel in stagnant liquid lead-bismuth*. In Press.
- [69] A. Brückman and J. Romanski. *On the Mechanism of Sulphide Scale Formation on Iron*. Corrosion Science **5**, 185–191 (1965).

- [70] Daniel Koury. *Investigation of Corrosion of Steel by Lead Bismuth Eutectic (LBE) Using Scanning Electron Microscopy and X-ray Photoelectron Microscopy*. Master's thesis University of Nevada, Las Vegas 2002.
- [71] Hubertus Nickel, Willem J. Quadackers and Lorenz Singheiser. *Determination of Corrosion Layers and Protective Coatings on Steels and Alloys Used in Simulated Service Environment of Modern Power Plants*. Transactions of the ASME **128**, 130–138 (2006).
- [72] M. Da Cunha Belo, M. Walls, N. E. Hakiki, J. Corset, E. Picquenard, G. Sagon and D. Noel. *Composition, Structure and Properties of the Oxide Films Formed on the Stainless Steel 316L in a Primary Type PWR Environment*. Corrosion Science **40** (2/3), 447–463 (1998).
- [73] Masahiko Kato and Ryutaro Souda. *Energy spectrum shape of low energy ion scattering from insulators and its similarity to asymmetric spectrum shape observed in core level XPS from metals*. Nuclear Instruments & Methods in Physics Research B **258**, 28–31 (2007).
- [74] C. M. K. Watts. *Dynamical screening effects in the Auger spectrum of metals*. J. Phys. F: Metal Phys. **2** (May 1972).
- [75] P. S. Cornaglia and A. Georges. *Theory of core-level photoemission and the x-ray edge singularity across the Mott transition*. Phys Rev B **75** (March 2007).
- [76] P. Hosemann, D. Koury, G. Swadener, M. Hawley, A. L. Johnson, J. Welch, G. Mori and N. Li. *Characterization of oxide layers on D9 grown in Lead Bismuth Eutectic (LBE)*. In Preparation, To Be Submitted in Journal of Nuclear Materials.
- [77] R. E. Lobnig, H. P. Schmidt, K. Hennesen and H. J. Grabke. *Diffusion of Cations in Chromia Layers Grown on Iron-Base Alloys*. Oxidation of Metals **37**, 1–2 (1992).
- [78] H. Glasbrenner, J. Konys, H. D. Röhrig, K. Stein-Fechner and Z. Voss. *Corrosion of ferritic-martensitic steels in the eutectic Pb-17Li*. Journal of Nuclear Materials **283-287** (1332-1335) (2000).
- [79] P. R. Wilson and Z. Chen. *The effect of manganese and chromium on surface oxidation products formed during batch annealing of low carbon steel strip*. Corrosion Science **49**, 1305–1320 (2007).
- [80] Y. F. Lu, W. D. Song, M. H. Hong, T. C. Chong and T. S. Low. *Mechanism of and method to avoid discoloration of stainless steel surfaces in laser cleaning*. Applied Physics A: Materials Science and Processing **64** (6) (1997).
- [81] A. Atkinson. *Conditions for the Formation of New Oxide within Oxide Films Growing on Metals*. Corrosion Science **22**, 347–357 (1982).



- [82] Don Baer. *Protective and Non-protective Oxide Formation on 304 Stainless Steel*. Applications of Surface Science **7**, 69–82 (1981).
- [83] X. Peng, J. Yan, Y. Zhou and F. Wang. *Effect of grain refinement on the resistance of 304 stainless steel to breakaway oxidation in wet air*. Acta Materialia **53**, 5079–5088 (2005).
- [84] M. D. Merz. *Oxidation Resistance of Fine-grained Sputter-deposited 304 Stainless Steel*. Metall. Trans. **10A**, 71–77 (1979).
- [85] J. R. Davis and Davis & Associates, Editoren. *ASM Specialty Handbook: Carbon and Alloy Steels*. ASM International 1996.

## VITA

Graduate College  
University of Nevada, Las Vegas

Daniel J. Koury

Local Address:

1271 Summer Dawn Ave.  
Henderson, NV 89014

Degree:

Bachelor of Science, Physics, 1998  
Bachelor of Science, Mathematics, 1998  
Florida Southern College of Lakeland, FL

Master of Science, Physics, 2002  
University of Nevada, Las Vegas of Las Vegas, NV

Dissertation Title: Characterization of The Mechanism of Bi-Layer Oxide Growth on Austenitic Stainless Steels 316L and D9 in Oxygen-controlled Lead-Bismuth Eutectic (LBE)

Thesis Committee:

Chairperson, Dr. John Farley, Ph.D.  
Chairperson, Dr. Allen Johnson, Ph.D.  
Committee Member, Dr. Malcolm Nicol, Ph.D.  
Committee Member, Dr. Jim Selser, Ph.D.  
Graduate Faculty Representative, Dr. Clemens Heske, Ph.D.